ALCOA

82 06 01 090

REPORT DOCUMENTATION PAGE		READ INSTRUCTIONS BEFORE COMPLETING FORM
1. REPORT NUMBER	2. GOVT ACCESSION NO. AD-A115 043	3. RECIPIENT'S CATALOG NUMBER
4. TITLE (and Subtitle) DEVELOPMENT OF STRUCTURE AND PROPERTIES OF 7050 AND 7475 ALLOYS DURING DIRECT EXTRUSION		5. TYPE OF REPORT & PERIOD COVERED FINAL
		6. PERFORMING ORG. REPORT NUMBER 56-80-AF10
7. AUTHOR(s) T. H. SANDERS, JR.		8. CONTRACT OR GRANT NUMBER(s) N00019-77-C-0499
9. PERFORMING ORGANIZATION NAME AND ADDRESS ALUMINUM COMPANY OF AMERICA ALCOA LABORATORIES ALCOA CENTER, PA 15063		10. PROGRAM ELEMENT, PROJECT, TASK AREA & WORK UNIT NUMBERS
11. CONTROLLING OFFICE NAME AND ADDRESS		12. REPORT DATE 1981 June 01
		13. NUMBER OF PAGES
14. MONITORING AGENCY NAME & ADDRESS(if different from Controlling Office)		15. SECURITY CLASS. (of this report) UNCLASSIFIED
		15a. DECLASSIFICATION/DOWNGRADING SCHEDULE

16. DISTRIBUTION STATEMENT (of this Report)

APPROVED FOR PUBLIC RELEASE; DISTRIBUTION UNLIMITED.

17. DISTRIBUTION STATEMENT (of the abstract entered in Block 20, If different from Report)

18. SUPPLEMENTARY NOTES

19. KEY WORDS (Continue on reverse side if necessary and identify by block number)

7475, 7050, High strength aluminum alloys, Microstructure, Tensile properties, Toughness, Constant amplitude fatigue crack growh, Direct extrusion

$(Z = \epsilon \cdot \exp(\frac{\Delta H}{}))$

20. ABSTRACT (Continue on reverse side if necessary and identify by block number)

The primary aim of the investigation was to explore the production and control of microstructures of 7050 and 7475 through variations in the temperature compensated strain rate, Z ($Z = \epsilon \exp(\frac{\Delta H}{RT})$). The experimental design was constructed such that the results could be expressed in terms of the more traditional -- billet temperature, extrusion ratio, and section aspect ratio. Extremes in ram speed, extrusion ratio, and billet temperature were chosen such that the widest variation in Z and, therefore, the

DD FORM 1473   EDITION OF 1 NOV 65 IS OBSOLETE   UNCLASSIFIED
1 JAN 73

20.

widest variation in microstructure could be achieved. Accordingly, 7050 and 7475 were direct extruded into round rod and rectangular bars on a 22.24 MN press. The microstructures were characterized in the solution heat treated and aged conditions as a function of temperature compensated strain rate, Z. The following observations were made: (1) Extrusions run under conditions of highest Z had the greatest tendency to recrystallize upon solution heat treatment. (2) Extrusion ratio appeared to have an effect on the development of structure even though geometry and ratio were taken into account in the definition of strain rate. The lower extrusion ratio consistently gave a greater tendency to recrystallize during heat treatment. (3) Under similar conditions, alloy 7050 had a greater tendency to recrystallize than alloy 7475. (4) The grain structure in the extrusions varied from surface to center. In extrusions with limited recrystallization, the amount of deformation could be qualitatively assessed by comparing the aspect ratio (length/width) of the original grains. Higher aspect ratios occurred near the surface of the extrusions. (5) The extrusion ratio and location within the extrusion affected the distribution of Al_7Cu_2Fe and Mg_2Si, the insoluble intermetallics. The effect of these microstructural features on the tensile, fracture toughness and fatigue crack growth are discussed.

SUMMARY

Direct extrusion of aluminum alloy 7050 and 7475 results in a product which has a nonuniform microstructure. The structure varies from surface to center and from front to rear of the product. The nonuniform structure develops within the billet during the extrusion process. Cylinder wall shear produces a region of intense deformation adjacent to the surface. During the stroke this layer widens and toward the end of the extrusion cycle, the heavily sheared layer constitutes a significant volume of the billet. The material at the surface of the product comes from the heavily sheared layer and the depth of this well defined layer increases from front to rear of the product. During solution heat treatment, if the structure has a tendency to recrystallize the greatest probability of recrystallization is at the surface. Extruding at high Z (low temperature and high strain rate where Z is the temperature compensated strain rate) facilitates recrystallization throughout the product with complete recrystallization at the surface. Furthermore, the results of this investigation indicate that under similar fabricating conditions 7050 has a greater tendency to recrystallize than 7475.

In addition to the effect of nununiform flow on the development of a nununiform grain structure, the distribution of insoluble particles are also affected by the metal flow. At high extrusion ratio, or near the surface where the amount of deformation is high, the interparticle spacing of the insolubles appears to be modified by deformation. Increasing the deformation

increases the interparticle spacing in a plane parallel to the deformation.

Yield strength was affected by cross-section geometry and composition, but was unaffected by changes in Z or R (extrusion ratio). The major effect of cross-section geometry appears to be on its influence on crystallographic texture. Axi-symmetric extrusion (round billet cross-section to a round product) leads to duplex fiber texture. The <111> and <100> directions are parallel to the axis of extrusion, changing the cross-section to a rectangle results in a texture similar to that which is produced by hot-rolling ((110) <$\bar{1}$12>)).

Ductility and toughness could be correlated to extrusion ratio and location with respect to surface or center of the extruded product. Increasing R or testing near the surface results in an increase in L and LT ductility and an increase in UPE in the L and LT orientations.

Analysis of the fatigue crack growth data revealed only one consistent trend in the data. The combination of high Z and high R resulted in the shortest lives for both 7050 and 7475.

The use of Z in relating microstructure to processing in heat treatable alloys must be approached with caution, since changes in temperature affect the amount of soluble phase in solution and therefore the recrystallization behavior.

FORWARD

TABLE OF CONTENTS

LIST OF FIGURES

LIST OF TABLES

INTRODUCTION

Extrusion is an important process in commercial forming of metals. It is, however, a complex process insofar as understanding how structure develops during deformation and how structure, in turn, determines final mechanical properties. There have been a number of investigations which have led to a fundamental understanding of the relationship between microstructure and processing variables such as billet temperature, ram speed, and extrusion ratio.[1-7] Although most of these studies have been conducted using high purity alloys, small laboratory presses, and axisymmetric deformation, the results of these investigations can be applied to the design and execution of a program to address some of the complexities of commercial extrusion. This program attempts to examine in detail the influence of changes in the basic extrusion variables on the development, distribution and morphology of a variety of microstructural features and the relationship of the microstructure to strength, toughness, and fatigue crack growth of heat treatable aluminum alloys.

In past investigations, partially extruded billets and products were examined by optical, X-ray degree of recrystallization, and transmission electron microscopy techniques. These examinations revealed systematic variations in deformation throughout the billet and product. The structural observations were correlated to the mechanical properties by applying concepts originally developed to explain

structural changes occurring in creep, where flow stress, σ_ϵ, strain rate, $\dot\epsilon$, and deformation temperature, T, are related by:[8-11]

$$\sigma_\epsilon = f(Z), \text{ where } Z = \dot\epsilon\{\exp(\frac{\Delta H}{RT})\}.$$

In the above equation, ΔH is an activation energy and Z is the Zener-Holloman parameter or temperature compensated strain rate.

Qualitatively, when Z is high, i.e., either the temperature is low or the strain rate is high, fewer thermally activated events can occur per unit strain, and, therefore, the flow stress will be high. When Z is low, the converse is true.

Structurally, for a particular combination of $\dot\epsilon$ and T, i.e., Z, a limiting or equilibrium subgrain size is reached and, correspondingly, a limiting flow stress results. Usually, both equilibrium subgrain size and flow stress can be functionally related to Z. The equilibrium structure is a consequence of the mutual rates of creation and annihilation of dislocations and the rearrangement of the remaining dislocations into regular low angle boundaries or subgrains. This mechanism is referred to as dynamic recovery.

Because flow stress at room temperature also increases with decreasing subgrain size, equilibrium structures produced under a variety of hot working conditions should reflect an

interrelationship between Z, subgrain size, and room temperature properties of nonheat treatable alloys.

The application of the above principles can then be applied to extrusions in the following way. The variables temperature, ram speed, and extrusion ratio can be used to calculate Z by applying certain simplifying assumptions. For instance, the starting billet temperature may be used as an estimate of temperature and the strain rate may be calculated by use of a relationship such as Feltham's:[12]

$$\dot{\bar{\epsilon}} = \frac{6D_C^2 V_{ram}(\ln R)\tan\alpha}{D_C^3 - D_E^3},$$

where:

$\dot{\bar{\epsilon}}$ = mean strain rate,

D_C = cylinder diameter,

D_E = diameter of extruded section,

V_{ram} = ram speed,

R = extrusion ratio, and

α = angle between cylinder center line and the dead metal zone boundary.

Thus, for given conditions, an estimate of the temperature compensated strain rate, Z, is:

$$Z = \left[\frac{6D_C^2 V_{ram}(\ln R)\tan\alpha}{D_C^3 - D_E^3}\right] \exp\left[\frac{\Delta H}{RT_{Billet}}\right].$$

Using these ideas, the present investigation aims to test the applicability and limitations of the above concepts when applied to commercial, heat treatable, high-strength 7XXX aluminum alloys and to make available the information gathered to aid in the production of consistent, predictable structures and properties.

EXPERIMENTAL PROCEDURE

Material

Four 22.86 cm (9.0") x 254 cm (100.0") ingots were cast by the HDC method. The melt analyses are listed in Table 1. The compositions are nominally equivalent to 7050 and 7475. Two solidification rates were used in an attempt to alter the ingot grain size to correspond to large and small ingot cross-sections. The cast ingots were scalped to approximately 15.5 cm (6.12") diameter and cut into 30.5 cm (12.0") length for extrusions billets.

Fabrication

The billets were extruded into round rod and rectangular bars from a 16.2 cm (6.38") diameter cylinder on a 22.24 MN (2500 ton) production size press. A detailed description of the experimental design is given in Appendix A. The extrusion data are summarized in Table 2 and represent two phases of work. In the first phase, aimed at better understanding of the development of structure and properties in an extruded product, four 7050 billets were preheated, reheated to the desired extrusion temperature and partially extruded to approximately 50% of complete extrusion. Once the desired amount of extrusion was achieved, the unextruded portion of the billet was pushed from

the container, sheared from the extruded product, and quenched
in room-temperature water. The elapsed time from load removal
to quench was approximately one minute. The unextruded billet
portions were split in half longitudinally. One half of the
billet was solution heat treated at 477°C (890°F) for 1.5 hours
and cold water quenched. Both halves were then machined on a
diametral plane and macroetched to reveal the flow patterns and
the developing structures in the as-fabricated temper (F) and
in the solution heat treated and quenched temper (W). The
macroetching was done using hot, 66°C(150°F) caustic solution
(5% by weight NaOH), washed in room temperature water, washed
in 20% (by volume) nitric acid to remove corrosion product, and
rinsed in water.

In the second phase, 26 billets were extruded at
various extrusion ratios, temperatures, strain rates, and
section geometries to manipulate microstructure, in accordance
with previous discussion.

Microstructure

Structure in the Billet. Figure 1 is a photograph
showing the grain flow in the high Z, low R extrusion (F temper)
and illustrating the regions of interest for the metallographic
and TEM investigations in the F and W tempers of the partially
extruded 7050 billets. As indicated in the photograph, there
are four regions to be examined. One is region A, a region of
intense deformation as suggested by the grain flow. This region
lies adjacent to the cylinder wall at the rear of the billet and

curves toward the die opening at the front of the billet. A
second region, B, lies along the centerline which extends from
the rear of the billet toward the die opening. A third region,
C, appears as a "cone" of deformation and is located in the
approach to the die opening. The fourth region, D, lies just
beyond the die exit in the product.

TEM and X-ray transmission specimens were prepared
from the partially extruded billets by machining a longitudinal
slab approximately 0.51 mm (0.020") thick. For reference, the
thinned sections contained the macroetched surface. The
machined slabs were chemically thinned in a solution containing
400 ml HCl, 400 ml H_2O, 20 grams NaCl and 4 grams $NiSO_4$. The
sections were then washed in a caustic solution (5% by weight
NaOH) and cleaned in a solution of concentrated HNO_3. Trans-
mission Laue photographs were taken at selected locations
adjacent to, and within, the heavily sheared layer in the F
and W tempers. Discs 3.0 mm (0.12") in diameter were punched
from the thinned sections of the high Z, low R and low Z, low
R extrusions. Only F temper material was examined in the TEM.
The discs were electropolished in a twin jet Fischione polishing
cell operated at approximately 12 volts d.c. A solution of 25%
(by volume) nitric acid and 75% methanol cooled to approximately
-30°C (-22°F) was used for the polishing.

The W temper metallographic specimens were mechanically
polished, electropolished using a solution of 46 ml HBF_4 (48%),
977 ml H_2O, and 7 grams of boric acid at 20 volts, and examined
using polarized light.

<u>Structure in the Product.</u> Selected specimens from near the midlength of the extruded products were examined in the F temper by TEM and the phases present along with their relative amounts determined by X-ray diffraction. Estimates of mean subgrain size were made using the linear intercept method. Measurements were made on foils prepared at the surface, T/4, and T/2 locations in the high Z, low R and low Z, low R 7050 extrusions. The X-ray intensity data were collected on film using a Guinier-deWolff quadruple focusing camera. All extrusions were examined by optical microscopy and transmission X-ray Laue techniques. The metallographic specimens were mechanically polished and examined in the as-polished and electropolished conditions.

The as-polished 7050 and 7475 specimens generally had a low volume fraction of secondary intermetallic precipitates, which is typical for these alloys. However, those extruded from the 7050 ingot cast at a slow solidification rate had a large amount of porosity along the centerline. Examples of this porosity are shown in Figure 2. Because the porous specimens came from midlength, the lot of extrusions in question was considered to be of unacceptable quality and was not examined further.

Estimates of mean subgrain size were made on the four 7050 extrusions at surface, T/4, and T/2 locations provided these regions did not fully recrystallize.

Reflection pole figure data were collected on the rectangular cross-section extrusions of 7050 and on the 7475 round rod. The specimens were machined from blanks along the centerline at mid-thickness on the rectangular section extrusions and from along the centerline on the round rod extrusions. The specimens were 2.54 cm (1.0") long by 2.54 cm (1.0") wide by 0.64 cm (0.25") thick and in the W temper. The data were collected using an automated Siemens texture diffractometer with an oscillating stage. To fully describe the texture the (111), (200), and (220) Bragg reflections were examined. Intensity histograms were collected at 8 second intervals while the ϕ axis (axis of roatation perpendicular to the plane of the specimen) and the χ axis (axis of rotation perpendicular to the ϕ axis) were continuously rotating at a 5:1 ratio. The simultaneous two-axis rotation resulted in a spiral covering the sphere of reflection, as illustrated by Figure 3. The same intensity data were corrected for the angular dependence of absorption and plotted using computer programs written at Georgia Tech.

Mechanical Testing

The front half of each extrusion was solution heat treated,* cold-water quenched, stretched 1.5%, naturally aged for one week, and artificially aged for 24 hours at 121°C followed by 15 hours at 163°C (T76-type tempers). The various specimens for mechanical testing were prepared from these front end

---

*Solution heat treatments: 7050 - 1.5 hours at 477°C (890°F) and for 7475 - 1.5 hours at 516°C (960°F).

sections taken at midplane along the centerline of the extrusions. A complete description of specimen location and the type of specimen is given in Appendix B.

Constant Amplitude Fatigue Crack Growth (CAFCG). The 7050 and 7475 extrusions in a T7651-type temper were investigated for changes in CAFCG performance as a function of the processing conditions. The FCG specimens were compact tension type with an L-T fracture plane orientation (See Appendix B).

All tests were conducted on closed loop, electro-hydraulic servo-controlled MTS test equipment. Crack growth was monitored electronically by crack propagation gauges as shown in Figure 4. Uniform increments of crack extension 1.27 mm (0.05") apart were measured as strands of the wire gauge broke due to the propagating crack. Numbers of cycles were monitored on a 20 counter electronic box so that as each gauge strand broke, the counter for that strand stopped and the next counter started. The data were obtained as crack length vs cycles and converted to rate of crack growth vs ΔK. Pilot tests were run to check the accuracy and reliability of this system. Figure 5 shows the crack growth vs number of cycles obtained by visual reading of photogrids on the surface of the specimen. It can be seen that they are in good agreement. The visual measurement can be made within ± 0.05 mm (± 0.002") or within $\pm 1\%$ of a/w. The maximum expected error in crack detection with gauges is estimated to be about ± 0.1 mm (± 0.004") or within $\pm 2\%$ of a/w.*

*Final Report NAVAIR Contract N00019-76-C-0482, 'Effect of Microstructure on Fatigue Crack Growth of 7XXX Aluminum Alloys Under Constant Amplitude and Spectrum Loading."

Humid air (relative humidity >90%) was used as the reference environment for all tests. The high humidity assures a mositure-saturated environment, thereby reducing sensitivity of crack growth rate to both test frequency and small changes in mositure content.*

All tests in this phase of the investigation were conducted at constant amplitude conditions with sinusoidal loading a maximum stress, σ_{max}, of 17.4 MPa (2524 psi) and a stress ratio of R=0.33. A frequency of 20 Hz was maintained through the entire test. Maximum load, P_{max}, and load range, ΔP, were maintained within $\pm 2\%$.

The propagation gauges were located to obtain data as the crack length, a, extended from 20.3 mm (0.8") to 45.7 mm (1.8") in all tests. The factors considered in deciding the location of the gauges are as follows:

Stress Intensity Range: The stress intensity range traversed during the constant load cycles corresponds to inter-mediate ΔK levels of 4.4 to 15.0 MPa$\sqrt{m}$ (4.0 to 13.6 ksi$\sqrt{in.}$). For screening purposes, these K levels were chosen to be high enough so as not to make the test too time consuming and low enough so that crack growth is not predominantly influenced by fracture toughness of the material.

Specimen Size Requirement: Calculations indicated

---

*Wei, R. P., "Some Aspects of Environment-Enhanced Fatigue Crack Growth," Engineering Fracture Mechanics, Vol 1, No. 4, April 1970.

that the uncracked ligament size exceeded the ASTM requirement,
w/a, equal to or greater than $4/\pi \frac{(K_{max})^2}{Y.S.}$.*

Precrack Interval: A sufficient precracked interval
of 17.1 mm (0.675") was provided to initiate the crack. The
final 3.2 mm (0.125") of precracking to 20.3 mm (0.8") of crack
length was done at the test loads and humidity to avoid any
transient effects.

Fractography

Sections of the fracture surface from the tensile, tear
and fatigue crack growth specimens were examined in the scanning
electron microscope to determine fracture mode and discern dif-
ferences in the fracture surface of the various samples.

Specimen Location Effects

To determine if the tensile and tear properties are influenced
by microstructure within a given extrusion, specimens were prepared
from a surface section of the low Z, low R 74750 extrusion in the
T7651 temper.

---

*ASTM E647-78T, "Tentative Test Methods for Constant-Load
Amplitude Fatigue Crack Growth Rates above 10^{-8} m/cycle,"
1978 Annual Book of ASTM Standards, Vol 10.

RESULTS

Structure in the Billet

In an attempt to better understand the development of structure in the product, partially extruded billets were examined in the F and W tempers. This section will summarize the microstructural observations.

The same general characteristics were observed in the macroetched section from each of the four billets partially extruded approximately 50% (15 cm butt). Consequently, the billet extruded at high Z into a low R product will be considered representative of the general metal flow. Figure 6 is a photograph of the macroetched F temper billet in the high Z, low R extrusion. A region of intense deformation, suggested by the grain flow, lies adjacent to the cylinder wall at the rear of the billet and curves toward the die opening at the front of the billet. This area is termed the heavily sheared layer.

A second region lies along the central portion of the billet and extends from the rear toward the front of the billet near the die opening. The amount of deformation as suggested by grain flow is limited at the rear but increases considerably near the die opening.

Surrounding the die opening there is an area which appears as a cone of deformation which is a result of grain distortion due to the shape change occurring as the metal moves from the billet to the smaller rectangular section.

The last region of interest is in the vicinity of the die exit and contains structure common to the billet and product.

The microstructures of the partially extruded 7050 billets were examined in the F-temper by the techniques of X-ray transmission Laue and TEM. Figures 7 and 8 contain pinhole photographs taken at several locations in the partially extruded 7050-F billets. The degree of recrystallization (as estimated by the pinhole films[*]) varied from none on either side of the heavily sheared layer to just started + at the center of the layer. Furthermore, the recrystallized grains at the center of the heavily sheared layer were fine. These observations are in contrast to those made at similar locations in the high Z, low R extrusion, Figure 8, where the structure was unrecrystallized throughout the billet.

TEM's from specific locations in the as-extruded billets are shown in Figures 9 and 10. The microstructure in the heavily sheared layer is characterized by a nonuniform distribution of equiaxed subgrains with mechanical fibering of the precipitates in the principle direction of metal flow. Away from the heavily sheared layer, slightly larger equiaxed subgrains were present. The microstructure of the high Z, low R extrusion was slightly different from that of the low Z extrusions, Figure 10. The subgrains in the high Z extrusion tended to be smaller and more uniform in size than those at similar locations in the low Z extrusion. In the heavily sheared layer, the subgrains were elongated in the direction of metal flow. As observed in the low Z extrusion, the precipitates were aligned in the direction

[*]Degree of recrystallization gradations: None, Just Barely Started, Just Started, Started, Partial, Complete.

of metal flow. Numerous, small equilibrium precipitates of
η ($MgZn_2$-type) and S (Al_2CuMg) were observed in the high Z and
not in the low Z extrusion.

Solution heat treating half of each of the partially extruded billets resulted in similar macro flow patterns. However, there were systematic variations in the recrystallization behavior which could be correlated to location within the billet, Z, and R.

Figure 11 is a polarized light micrograph taken across the heavily sheared layer in the high Z, low R extrusion. A continuous variation in grain structure is apparent in this low magnification photograph. Correspondingly higher magnification polarized light micrographs are included in Figure 12. These photographs were taken at the locations indicated on Figure 11.

Loacation A contains evidence of the original cast structure; these cast grains, however, are distorted and are elongated in the direction of metal flow. At position B, microstructure consists of coarse elongated and fine equiaxed recrystallized grains with areas of unrecrystallized grains. At position C, most of the field contains coarse, recrystallized grains with a few fine equiaxed recrystallized grains. At the last position, D, most of the structure is unrecrystallized with a few recrystallized grains.

Figures 13&14 contain polarized light micrographs taken approximately at the center of the heavily sheared layer of the four different partial extrusions. Figure 13 contains representative micrographs taken of the low Z and high Z variants both extruded at low R. The microstructure in the low Z was characterized by a mixed grain structure containing both unrecrystallized

and fine recrystallized grains. This structure is in contrast to the coarse, elongated recrystallized grains observed in the high Z extrusion. Figure 14 contains representative micrographs taken of the low Z and high Z variants both extruded at high R. The low Z microstructure was characterized by a mixed grain structure containing areas of unrecrystallized grains, and both coarse and fine recrystallized grains. The recrystallized grains that formed under these extrusion conditions were slightly larger than those extruded at the same calculated Z, but at the lower extrusion ratio. The grain structure from the high Z billet extruded at high R contained unrecrystallized areas and both fine and coarse recrystallized grains. This microstructure was different from the structure extruded at the same calculated Z, but at the lower extrusion ratio. The low R resulted in much coarser recrystallized grains, and a high fraction of recrystallized grains throughout the shear layer.

Thus, the microstructures of the solution heat treated partial extrusions in the heavily sheared layer were observed to vary across the layer with the greatest tendency to recrystallize near the center. Furthermore, Z and R both seemed to control the type of microstructure produced. These structural variations can be summarized as follows:

> The high Z extrusions generally resulted in a greater
> tendency to recrystallize than those extruded at
> the low Z. Low R tended to result in larger, elongated
> recrystallized grains when the calculated Z's were the
> same.

Thus, the high Z, low R condition resulted in the greatest tendency to recrystallize, producing coarse, elongated grains.

Figures 15-18 contain micrographs of orthogonal sections illustrating the effect of varying Z and using the same extrusion ratio (high R condition). The micrographs were taken at areas located along the centerline and near the rear of the billet, and near the die opening at the front of the billet within the cone of deformation. At the rear, the original cast grains are easily recognizable and have undergone little shape change. However, near the front in the cone of deformation, the micrographs illustrate the shape change as a consequence of extrusion from the round billet to the thin, rectangular section.

The transition area, or the area including material in the billet and product, is quite interesting, especially in the vicinity of the die corner showing the structure forming the product surface.

Figure 19 is a low magnification polarized light micrograph showing the variation of grain structure from surface into the center of the product. The section was from material extruded at high Z high R. At the surface there is a layer containing coarse recrystallized grains. Below this layer the microstructure is unrecrystallized and the width of these unrecrystallized grains increases from surface to center.

Figures 20-21 include four variants of the partially extruded 7050 at the die opening. Figure 20 shows the effect of varying Z and extruding at low R. Extruding at low Z results in

a thin layer of coarse, elongated recrystallized grains. Extruding at high Z, on the other hand, results in a recrystallized layer composed of coarse, elongated recrystallized grains extending across the field of view.

Figure 21 shows the effect of varying Z on the development of the recrystallized layer in the high R extrusions. Increasing Z increases the depth of the coarse recrystallized layer.

A comparision of the micrographs in Figures 20 and 21 illustrates the effect of R on structure while maintaining the same calculated Z. The greatest absolute depth occurs in the high Z, low R, but a comparison of the depth of this recrystallized layer with the layer formed by extruding at high Z, high R shows that the low R thickness was approximately two times that of the high R. The difference in reduction in the direction in which the micrograph was taken was approximately 2.7 times greater in the high R.

The recrystallized layer present on the surface appears to develop from material moving from the heavily sheared layer. The depth of the recrystallized layer is qualitatively related to both Z and R. High Z tends to result in greater depth and the greatest absolute depth occurs when extruded at high Z and low R.

The above observations were made at approximately 50% of completion of extrusion. This next section will summarize the observations made on the butt ends of the high and low Z variants of the low R extrusions of 7050.

Metallographic examinations of W-temper sections of the
butt ends of 7050 extruded at low and high Z at low R were made
to complete the understanding of microstructure development during
extrusion. As illustrated in the metallography from the partially
extruded billets, variations in grain flow, recrystallization,
and grain size were observed. There were, however, some specific
differences between the structure observed at 50% and near the
end of the stroke.

The continuation of the extrusion process has widened
the heavily sheared layer, for example, compare Figure 22 with
Figure 6. The heavily sheared layer now constitutes a significant
fraction of the billet. Furthermore, material from the heavily
sheared layer is not confined to a thin layer at the surface of
the product, but now penetrates well into subsurface layers of
the product. Figure 22 compares the effect of Z on the structure
after solution heat treatment. (It is important to note the
fine grain structure in the zone which separates the billet and
the product is a result of the effect of the deformation from
shearing the product from the billet rather than the extrusion
process itself.)

Figures 23 and 24 contain micrographs taken at com-
paratively higher magnification than in Figure 22 from the
heavily sheared layer of the low Z extrusion. In this region
very fine recrystallized grains are present. Near the top of the
heavily sheared layer, however, there are some coarse, elongated,
recrystallized grains. Figure 24 is a photomicrograph of this
area. The large grains appear to be associated with tears in
the metal.

Figure 25 shows the grain structure in, and adjacent to, the heavily sheared layer in the high Z extrusion. In contrast to the grain structure in the heavily sheared layer of the low Z extrusion, Figure 23, the recrystallized grains are not uniform in size and numerous large elongated grains can be seen.

Figures 26 and 27 show the grain structure in, and adjacent, to the heavily sheared layer in the low Z, Figure 26, and high Z, Figure 27, extrusions. In the low Z extrusions, the structure is mixed with fine recrystallized grains along with the elongated cast grains. In contrast, the high Z extrusion contains coarse, elongated, fully recrystallized grains.

In summary, toward the end of the stroke, the heavily sheared layer has widened and constitutes a significant portion of the billet area. In areas that have recrystallized, the low Z extrusion results in a more uniform, fine grain structure than the high Z extrusion.

Structure in the Product

The detailed optical metallographic and transmission X-ray Laue investigations on each of the 7050 and 7475 extrusions showed a number of microstructural variations. The observations could be correlated qualitatively to temperature compensated strain rate, Z, extrusion ratio, R, alloy, and specimen location as to surface or center.

Extrusions run under conditions of highest temperature compensated strain rate, Z, had the greatest tendency to recrystallize upon solution heat treatment. This can be shown by comparing Figures 28 through 33 with Figures 34 through 39. However, extrusion ratio also appeared to have an effect on the development of structure even though geometry and ratio were taken into account in the definition of strain rate. The lower extrusion ratio gave a greater tendency to recrystallize during solution heat treatment at the high Z (e.g., compare Figure 28 with Figure 31). However, when extrusion was carried out at low Z, the combination low Z, low R resulted in the lowest degree of recrystallization. Variation in alloy chemistry also seemed to affect the degree of recrystallization of the W temper products. Under similar extrusion conditions, alloy 7050 had a greater tendency to recrystallize than alloy 7475. For example, compare Figure 28 with Figure 29. Thus, alloy 7050 extruded using high Z, low R conditions had the greatest tendency to recrystallize while 7475 extruded at low Z and low R did not appear to recrystallize. Furthermore, the 7475 low R, either as round rod

or rectangular section was unrecrystallized in the W temper.

As noted earlier, minor differences in the effect of cooling rate during solidification were observed in the ingot structure. However, there was no detectable effect of cooling rate in the development of structure in the extruded products of 7475.

The degree of recrystallization estimated from X-ray pinholes taken near the center agreed qualitatively with optical results (Table 3).

The grain structure in the extrusions varied from center to surface. In extrusions with limited recrystallization, the amount of deformation could be qualitatively assessed by comparing the aspect ratio (length/width) of the original grains. Higher aspect ratios (greater deformation) occurred near the surface of the extrusions (Figure 40). In extrusions which re-crystallized, the greatest tendency to recrystallize occurred at the surface of the extrusions.

As-polished sections of 7050 and 7475 rectangular cross-section extrusions showed an effect of extrusion ratio on the size and distribution of the insoluble phases. The variation was independent of alloy (7050 versus 7475) and Z. Random metallurgical sections for the low Z 7050 taken at the surface, T/4 and T/2 locations are included in Figure 41 to illustrate the effect of R on the particle distribution. The size and distribution in the low R extrusion changed from surface to center. At the surface, the particles were slightly smaller

and discrete compared to the larger and more clustered particles at T/2. On the other hand, the high R extrusion did not show this through thickness variation. A comparison of the high R with the low R showed that the greater reduction tended to result in a finer distribution of particles when comparing the T/2 and T/4 locations. However, the surface sections of the low and high R extrusions were similar. For comparison, Figure 42 includes a random metallographic sections comparing high and low R insoluble particle distribution at the T/2 locations.

High magnification often revealed the presence of substructure in unrecrystallized grains. When recrystallization occurred, this substructure was absent. Micrographs with three different orientations of polarization are shown in Figure 43. Substructure is not present in the recrystallized grain regardless of orientation, but can be seen in the surrounding unrecrystallized grains. In certain instances, an alignment of the substructure was observed. Three orientations, Figure 44, show the distribution of substructure in a unrecrystallized section of extrusion, when in contrast the substructure appears to be aligned at approximately 45° to the extrusion direction (parallel to the planes of maximum shear). Higher magnification in another sample, Figure 45, further illustrates this effect.

There appeared to be an effect of Z on the ability to show subgrain contrast in the unrecrystallized areas of the products. Figures 46 and 47 contain polarized light micrographs of W-temper, longitudinal sections of 7050, the four combinations of high and low Z and R. At both low and high R, high Z tends to produce a microstructure which has enhanced substructure

contrast, whereas low Z does not. However, subgrains were present
in the unrecrystallized grains extruded at both low and high Z.

The low Z, low R and high Z, low R microstructures were
examined in the F- and W-tempers at the surface, T/4 and T/2
locations. Foils were prepared from planar sections parallel
to the surface of the extrusions. The average subgrain sizes are
summarized in Table 4. The subgrain sizes varied slightly from
surface to center, the larger subgrains were generally observed
in the center of the extrusions, and the low Z extrusions usually
had larger subgrain sizes than those extruded at high Z.

In F-temper material, occasionally areas were observed
which contained subgrains adjacent to areas which were fully re-
crystallized, Figure 48.

Pole figures for the W-temper 7050 extruded at low Z,
low R, and low Z, high R; and 7475 extruded axisymmetrically into
a round rod are plotted and discussed in Appendix C.

Mechanical Testing

The average tensile, yield, elongation and reduction in area for duplicate longitudinal (L) and long-transverse (LT) tensile tests are summarized in Tables 5 and 6. The averages of triplicate tear tests for L-T* and T-L** orientations are summarized in Tables 7 and 8.

Alloy type, 7050 versus 7475, was the only parameter in this program which affected either yield or tensile strength. However, tensile ductility, Tables 5 and 6, and toughness, as measured by a tear test, Tables 7 and 8, could be consistantly correlated to extrusion ratio. The high R extrusions gave the highest tensile ductility (as measured either by total elongation or reduction in area). Further, high R gave higher unit propagation energies (UPE's) than did the corresponding low R extrusion S, regardless of specimen orientation.

Also, another interesting trend in UPE can be taken from the data in Tables 7 and 8. Within an extrusion condition, 7475 solidified at the slower rate (S# 498813, -811, -821, -825) had lower UPE's than 7475 solidified more radily (S# 498814, -812, -822, -826). The casting rate effect was present in both orientations.

CAFCC

A total of 14 tests (a single test for each variable) were made to evaluate the effects of the different extrusion para-

---

*L-T: Stress in longitudinal direction, crack growing in transverse direction.
**T-L: Stress in transverse direction, crack growing in longitudinal direction.

meters on the 7050 and 7475. The results are plotted in Figures 49-53. The data are presented according to crack length, a, versus the number of cycles, N, Figures 49-51, and as the incremental crack growth per cycle, da/dn, versus the cyclic stress intensity factor range, ΔK, Figures 52 and 53. Each figure contains annotated data points to indicate the alloy and process variables. Also, the amount, in degrees, the crack deviated from an ideal crack plane, Figure 54 is given. Cracks deviating by more than $5°$ violate the requirements imposed by ASTM E647-78T. For comparison, results of other investigations in similar tempers are plotted on Figures 52 and 53.

Examination of Figures 49 and 50 indicates that only one consistent trend emerges from the data. The combination of high Z, high R results in the shortest life. This observation was true for 7050 and both 7475 alloys.

Fractography

The tensile, Kahn tear, and FCG fracture surfaces were examined in the SEM to determine the nature of the failure process and the influence of the microstructure on the propagation of a crack.

Tensile fractures. Regardless of the alloy or processing variables, the predominant mode of failure was ductile dimple rupture. Representative SEM's of the tensile failures of 7050 and 7475 are included in Figures 55 and 56.

Tear fractures. Figures 57 and 58 contain SEM's of TL and LT tear fractures of 7050 extruded at low Z, low R

(Figure 57), and low Z, high R (Figure 58). These micrographs were taken beyond the pop-in area where the crack was propagating stably. From these micrographs it appears that the crack path is influenced by the presence of the secondary intermetallics. The distribution of the dimples on the high R extrusion appears to be more uniform than the dimple distribution on the low k extrusion. Figures 59 and 60 further illustrate the effect of particles and their distribution on the propagation of the crack. Again, these micrographs were taken from regions on the fracture surface where the crack was propagating stably. A low magnification micrograph is included to establish an overall view of the fracture surface.

FCG fractures. Fracture surfaces at different ΔK's are shown in Figures 61-68 for 7050 extruded under the four test conditions. Only extrusion ratio appeared to have an effect on fracture morphology. The effects were particularly pronounced at low ΔK's, where the fracture path, though propagating transgranularly, was strongly influenced by the grain morphology. Figures 61-64.

Extrusion ratio also appeared to have a minor effect on the fracture surface in the overload region (high ΔK). Figures 65-68 contain SEM's taken near the transition region from crack growth to overload. The dimples formed in high R extrusions, Figures 65 and 67, appear to be slightly smaller and more uniformly distributed than the dimples which formed in the low R extrusion shown in Figures 66 and 68.

In summary, only extrusion ratio, R, appeared to have an effect on the fracture appearance. The origin of this effect may be in the influence of the extrusion ratio on modifying the distribution of the insoluble, second phase particles, and modification of the size and shape of the unrecrystallized grains.

Specimen Location Effects

Triplicate Kahn tear tests were conducted on a 7475 low Z, low R extrusion machined from just below the surface. These results are presented in Table 9. There was an increase in UPE going from the center to near surface. (Compare Table 8 with 9).

SUMMARY OF RESULTS

Direct extrusion of aluminum alloy 7050 and 7475 results in a product which has a nonuniform microstructure. The structure varies from surface to center and from front to rear of the product. The nonuniform structure develops within the billet during the extrusion process. Cylinder wall shear produces a region of intense deformation adjacent to the surface. During the stroke this layer widens and toward the end of the extrusion cycle, the heavily sheared layer constitutes a significant volume of the billet. The material at the surface of the product comes from the heavily sheared layer and the depth of this well defined layer increases from front to rear of the product. During solution heat treatment, if the structure has a tendency to recrystallize the greatest probability of recrystallization is at the surface. Extruding at high Z (low temperature and high strain rate) facilitates recrystallization throughout the produc with complete recrystallization at the surface. Furthermore, the results of this investigation indicate that under similar fabricating conditions 7050 has a greater tendency to recrystallize than 7475.

In addition to the effect of nonuniform flow on the development of a nonuniform grain structure, the distribution of insoluble particles are also affected by the metal flow. At high extrusion ratio, or near the surface where the amount of deformation is high, the interparticle spacing of the insolubles appears to be modified by deformation. Increasing the deformation increases the interparticle spacing.

Yield strength was affected by cross-section geometry and composition, but was unaffected by changes in Z or R. On the other hand, ductility and toughness could be correlated to extrusion ratio and location with respect to surface or center of the extruded product.

Analysis of the fatigue crack growth data revealed only one consistent trend in the data. The combination of high Z and high R resulted in the shortest lives for both 7050 and 7475.

DISCUSSION

In this program, composition and shape had an effect on yield strength; whereas, extrusion ratio, R, and Z did not have an effect on the yield strength. A comparison of the 7475 tensile data in Table 5 shows the result of changing the shape from a round cross-section to a rectangular cross-section on the longitudinal yield strength of 7475 identically aged. The round rod gives higher strength than the rectangular sections. This effect has been reported by others[13] and is more dramatic in the T651 temper. The primary difference in the structure of the round rod and the rectangular section is the crystallographic texture, Appendix C. The round rod has a duplex fiber texture with a strong <111> component and a weak <100> component. On the other hand, the rectangular sections have a rolling texture, (110) <1$\bar{1}$2>.

Since changes in recrystallographic texture may affect
strength, a systematic investigation attempting to relate shape
and yield strength to crystallographic texture was conducted[13].
The results of this investigation are summarized in Figures 69
and 70.   The yield strength showed the usual inverse correlation
with tensile elongation, Figure 70.   However, increasing the
aspect ratio decreased the yield strength. These authors
correlated the decrease in the density of <111> parallel to the
tensile axis. For a (110) <1$\bar{1}$2> texture, the principle crystallo-
graphic axis parallel to the tensile axis is the <1$\bar{1}$2>. With
the high density of <111> parallel to the tensile axis, therefore,
in the round rod there is a high density of (111) planes nearly
perpendicular to the tensile axis thus unfavorably oriented for
slip. Alternatively, one might relate the density of <111>
parallel to the tensile axis and the corresponding higher Taylor
factor than would occur with a <112> parallel to the tensile
axis.[14] Regardless of the precise mechanism of strengthening,
it is clear that for the same alloy processed under nearly
identical conditions of temperature and strain rate, changes in
die geometry which change texture can have a larger affect on
yield strength in 7XXX alloys than changes in temperature
compensated strain rate, Z.

Figures 9 and 10 compare the F-temper microstructures at
equivalent positions in the interior of two partially extruded
7050 ingots. (Low Z is shown in Figure 9 and high Z is shown in
Figure 10.)   In addition to the presence of a deformation sub-
structure, soluble phases such as Al_2CuMg and $Mg (Zn, Cu, Al)_2$

are also present. The volume fraction of these phases is dependent upon the reheat time and temperature prior to hot working.

Figure 71 is a schematic illustrating the effect of composition on the solvus temperature. For a given composition, increasing the hot working temperature decreases the volume fraction of soluble phase, or at a constant temperature, increasing the solute content decreases the volume fraction of soluble phases. Over the hot working range, 290-425°C, the fraction of soluble phase present varies significantly for 7475 and 7050. Thus the choice of hot working temperature plays two important roles in heat treatable aluminum alloys. The hot working temperature affects the dynamic recovery processes by increasing the number and mobility of the dislocations. The result is that at low hot working temperatures a smaller subgrain size is observed compared to the subgrain size when hot working at a higher temperature. This correlation has been observed in single phase alloys or alloy systems in which the fraction of second phase particles is small and temperature independent. In heat treatable alloys, the soluble elements, Zn, Mg, and copper, precipitate at the hot working temperature, thus decreasing the temperature or increasing the fraction of second phase particles.

The second phase particles act as sources and sinks for dislocations during the deformation process. The interparticle spacing may have a more important influence on the subgrain size and distribution than does the state of stress as determined by temperature. Therefore, when deciding how to apply the concepts

of hot working, one must know if the structure is temperature dependent over the range of hot working conditions. For the two alloys investigated in this program, the effect of temperature on structure must be considered.

In a detailed investigation on 7050 extrusions, the effects of fabricating variables and section geometry on properties were determined. Since the main thrust of that program was to generate data for MIL-HDBK-5,[15] a detailed microstructural study was not conducted, however, the mechanical properties reported were similar to the findings of this investigation, with respect to ratio effects. For a given aspect ratio the yield strength, increasing the extrusion ratio increases the NTS/YS ratio, or, for a given extrusion ratio and yield strength, increasing the aspect ratio increases the LT-NTS/YS ratio. For an alloy which fails by micro-void coalescence, it is the interparticle spacing which controls • fracture. Processing which modifies that distribution will alter the toughness. In this investigation and the report in Reference 15, increasing the extrusion ratio, proximity to the surface, or aspect ratio, resulted in an increase in fracture toughness.

CONCLUSIONS

For the two alloys investigated a clear, qualitative description relating the process variables, microstructure, and properties emerged. However, if we are to consider a different alloy system and a different method of hot working, the findings of this program would serve as a guide.

The microstructure of a commercial alloy is a composite of a variety of components. Some of these components such as grain morphology are affected by the conventional hot working variables T and $\dot{\varepsilon}$. However, other components such as deformation texture and insoluble particle distribution are affected by die geometry, extrusion ratio, and location. One needs to know which microstructural feature controls the property of interest and how that microstructural feature is altered by the deformation. Consequently, a number of investigations of the type reported in this document will be necessary before a generalized relationship between process, structure, and properties in aluminum alloys can be presented.

REFERENCES

1. B. J. Meadows, M. J. Cutler: Journal of the Institute of Metals, 97 (1969) 321.

2. T. Sheppard and D. Raybould: ibid., 101 (1973) 33.

3. D. Raybould and T. Sheppard: ibid., 101 (1973) 45.

4. D. Raybould and T. Sheppard: ibid., 101 (1973) 65.

5. T. Sheppard and D. Raybould: ibid., 101 (1973) 73.

6. M. M. Faray and M. H. Ahmed: Materials Science and Engineering 17 (1965) 131.

7. M. M. Faray and C. M. Sellars: Metals Technology, 172 (1975). 220.

8. H. J. McQueen: Journal of Metals, 20 (1968) 31.

9. J. G. Byrne: Recovery, Recrystallization, and Grain Growth, MacMillian, New York, pp 47-901.

10. C. M. Sellars and W. J. McG. Tegart: Mem. Scient. Revue Me'tall., 63, (1966) 731.

11. P. A. Beck, B. G. Ricketts, and A. Kelly: Trans. Met. Soc. AIME, 215 (1959) 949.

12. B. Avitzer: Metal Forming Processes and Analysis, McGraw Hill, New York, NY, 1968.

13. I. G. Palmer, R. E. Lewis, and D. D. Crooks: In Aluminum-Lithium Alloys, Ed. by T. H. Sanders, Jr. and E. A. Starke, Jr., pp. 241-262, TMS-AIME (1981).

14. W. A. Backofen: Deformation Processing, Addison-Wesley, Reading, Mass., 1972.

15. J. T. Staley, J. E. Jacoby, R. E. Davies, G. E. Nosdmark, J. D. Walsh, and F. R. Rudolf: "Aluminum Alloy 7050 Extrusions," Air Force Materials Laboratory Report: AFML-TR-76-129, March 1977.

Table 1. Chemical Analyses of the 7050 and 7475

Alloy	Si	Fe	Cu	Mg	Cr	Zn	Ti	Zr
7050-A	0.04	0.06	2.23	2.13	--	6.06	0.02	0.12
7050-B	0.04	0.06	2.28	2.11		6.15	0.02	0.12
7475-A	0.04	0.05	1.55	2.22	0.25	5.61	0.02	--
7475-B	0.04	0.06	1.64	2.49	0.25	5.78	0.02	--

Table 2. Extrusion Parameters Used to Control Grain Structure

S. Number	Alloy	Billet Temp, °C	Ram Speed, mm/sec	Section, LxW (mm)
498816	7050	288	1.8	96.3X8.13
498813	7475	288	1.8	96.3x8.13
498814	7475	288	1.8	96.3x8.13
498810	7050	288	5.8	101.6x25.4
498811	7475	288	5.8	101.6x25.4
498812	7475	288	5.8	101.6x25.4
498820	7050	428	.23	96.3x8.13
498821	7475	428	.23	96.3x8.13
498822	7475	428	.23	96.3x8.13
498824	7050	428	.75	101.6x25.4
498825	7475	428	.75	101.6x25.4
498826	7475	428	.75	101.6x25.4

Table 3. Estimated Degree of Recrystallization Determined
by the X-ray Pinhole Technique Taken Near the
Center of the SHT Product

S. Number	Alloy	Degree of Recrystallization*	Z	R
498816	7050	Just Started+	High	High
498813	7475	Just Barely Started-	High	High
498814	7475	Just Barely Started-	High	High
498810	7050	Partial+	High	Low
498811	7475	Partial-	High	Low
498812	7475	Started-	High	Low
498820	7050	Just Started-	Low	High
498821	7475	Just Started	Low	High
498822	7475	Just Started-	Low	High
498824	7050	Just Started	Low	Low
498825	7475	None	Low	Low
498826	7475	None	Low	Low

Degree of Recrystallization Gradation: None, Just Barely Started, Just Started, Started,
Partial, Commplete.

Table 4. Average Subgrain Size in the F- and W-Tempers of 7050
as a Function of Process Variables and Location

| Location | Extrusion Condition | | Subgrain Size (μm) | |
	Z	R	F-Temper	W-Temper
Surface	low	low	1.6	2.1
T/4	low	low	2.4	2.5
T/2	low	low	3.0	3.0
Surface	high	low	1.0	recrystallized
T/4	high	low	1.0	1.5
T/2	high	low	1.4	2.0

Table 5. Longitudinal (L) Tensile Properties

S. Number	Alloy	Tensile MPa (ksi)	Yield (.2%) MPa (ksi)	Elong. in 2" (%)	Reduction in Area (%)
498816	7050	582 (84.4)	528 (76.6)	15.0	43
498813	7475	568 (82.4)	505 (73.2)	16.0	42
498814	7475	568 (82.4)	510 (74.0)	15.5	44
498810	7050	570 (82.6)	520 (75.4)	14.0	37
498811	7475	561 (81.4)	503 (73.0)	13.8	36
498812	7475	552 (80.1)	494 (71.6)	13.8	37
498820	7050	586 (85.0)	535 (77.6)	16.0	46
498821	7475	568 (82.4)	507 (73.6)	16.0	46
498822	7475	563 (81.7)	502 (72.8)	16.5	46
498824	7050	583 (84.6)	537 (77.9)	13.8	38
498825	7475	562 (81.5)	507 (73.6)	14.2	40
498826	7475	558 (81.0)	503 (73.0)	15.2	44
Round Rod 5.72 cm (2.25"), Diameter					
498817	7475	574 (83.2)	527 (76.4)	13.8	44
498818	7475	571 (82.8)	523 (75.8)	13.0	40

Table 6. Long-Transverse (LT) Tensile Properties

S. Number	Alloy	Tensile MPa (ksi)		Yield (.2%) MPa (ksi)		Elong. in 2" (%)	Reduction in Area (%)
498816	7050	558	(81.0)	502	(72.8)	15.0	40
498813	7475	541	(78.5)	481	(69.8)	16.0	41
498814	7475	549	(79.6)	487	(70.5)	15.0	42
498810	7050	554	(80.4)	501	(72.6)	12.1	28
498811	7475	539	(78.2)	481	(69.8)	14.0	32
498812	7475	518	(75.2)	459	(66.6)	11.4	32
498820	7050	572	(83.0)	516	(74.8)	16.0	40
498821	7475	553	(80.2)	491	(71.2)	16.0	42
498822	7475	552	(80.1)	491	(71.2)	15.5	42
498824	7050	570	(82.6)	518	(75.1)	12.1	30
498825	7475	545	(79.1)	487	(70.6)	13.6	35
498826	7475	531	(77.0)	472	(68.4)	13.6	42

Round Rod 5.72 cm (2.25") Diameter (Transverse)

S. Number	Alloy	Tensile MPa (ksi)		Yield (.2%) MPa (ksi)		Elong. in 0.5" (%)	
498817	7475	514	(74.6)	472	(68.5)	10.0	
498818	7475	509	(73.8)	451	(65.4)	10.0	

Table 7. Longitudinal (L) Tear Properties

S. Number	Alloy	Tear Strength MPa (ksi)		Tear Strength/Yield Strength	Unit Propagation Energy, KJ/m² (In.-lb/in.²)	
498816	7050	709	(103.0)	1.34	129.1	(735)
498813	7475	694	(100.7)	1.38	134.1	(765)
498814	7475	699	(101.5)	1.37	116.1	(663)
498810	7050	682	(99.0)	1.31	114.8	(655)
498811	7475	669	(97.2)	1.33	73.7	(420)
498812	7475	669	(97.2)	1.36	82.9	(475)
498820	7050	735	(106.7)	1.37	171.1	(975)
498821	7475	690	(100.2)	1.36	98.6	(565)
498822	7475	711	(103.3)	1.45	113.2	(646)
498824	7050	699	(101.4)	1.31	100.6	(575)
498825	7475	675	(98.0)	1.33	84.1	(480)
498826	7475	685	(99.4)	1.36	103.6	(590)
Round Rod 5.72 cm (2.25") Diameter						
498817	7475	719	(104.3)	1.37	95.6	(546)
498818	7475	715	(103.7)	1.37	87.4	(499)

Table 8. Long-Transverse (LT) Tear Properties

S. Number	Alloy	Tear Strength MPa (ksi)		Tear Strength/Yield Strength	Unit Propagation Energy KJ/m² (In.-lb/in.²)	
498816	7050	685	(99.4)	1.37	66.7	(380)
498813	7475	679	(98.5)	1.41	73.3	(420)
498814	7475	690	(100.2)	1.42	82.5	(470)
498810	7050	586	(85.0)	1.17	44.6	(255)
498811	7475	627	(91.0)	1.30	50.5	(290)
498812	7475	611	(88.7)	1.33	60.1	(345)
498520	7050	679	(98.5)	1.32	66.3	(380)
498821	7475	678	(98.3)	1.38	69.9	(400)
498822	7475	696	(101.0)	1.39	113.2	(645)
498824	7050	539	(78.3)	1.04	36.0	(205)
498825	7475	610	(88.5)	1.25	46.6	(265)
498826	7475	657	(95.3)	1.39	65.1	(370)
Round Rod 5.72 cm (2.25") Diameter (Transverse)						
498817	7475	470	(68.3)	1.00	27.0	(155)
498818	7475	465	(67.5)	1.03	39.6	(255)

Table 9. Long-Transverse (LT) Tear Properties

S. Number	Alloy	Tear Strength MPa (ksi)	Tear Strength/Yield Strength	Unit Propagation Energy KJ/m² (In.-lb/in.²)
498825	7475	657 (95.3)	1.35	96.7 (550)
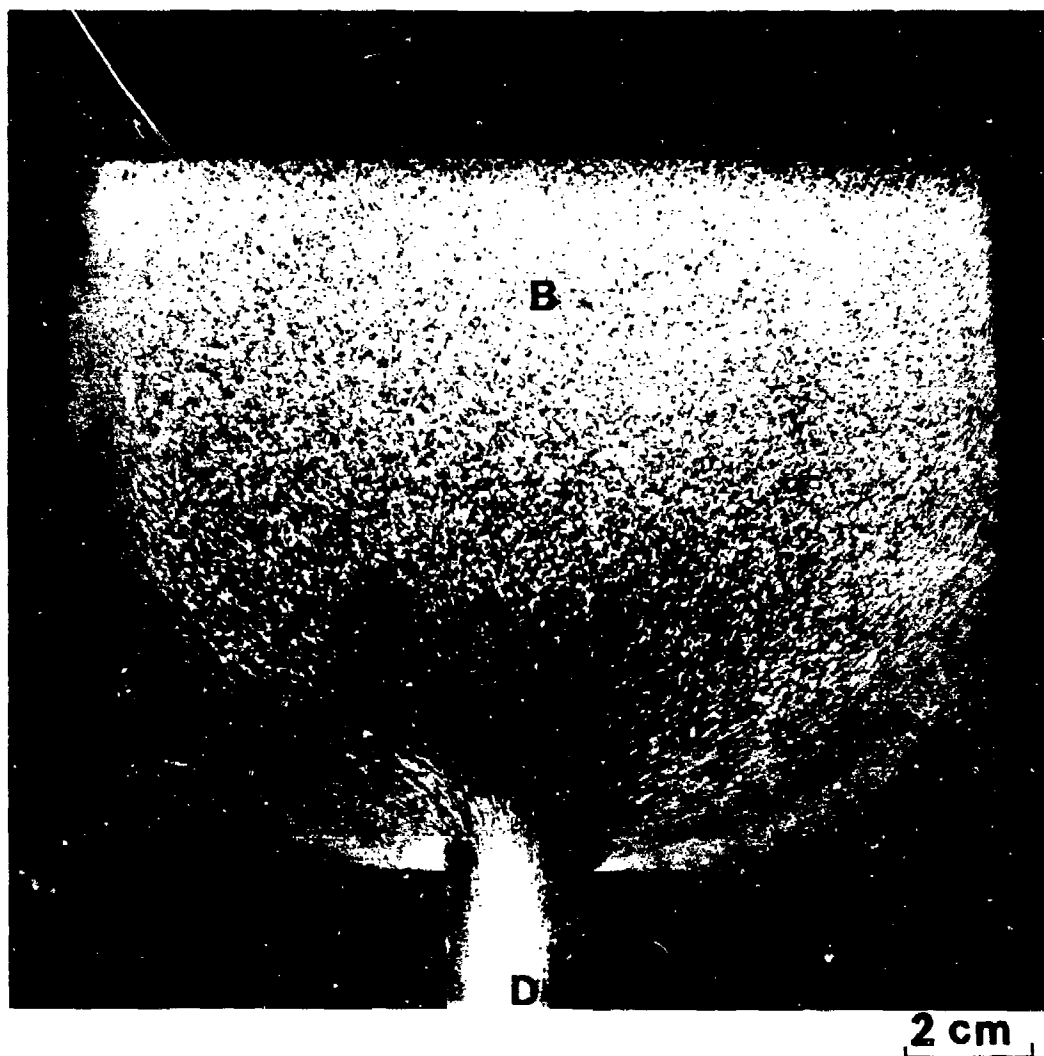
Figure 1. Photograph of macroetched F-temper billet extruded at high Z, low R showing the various regions of interest.
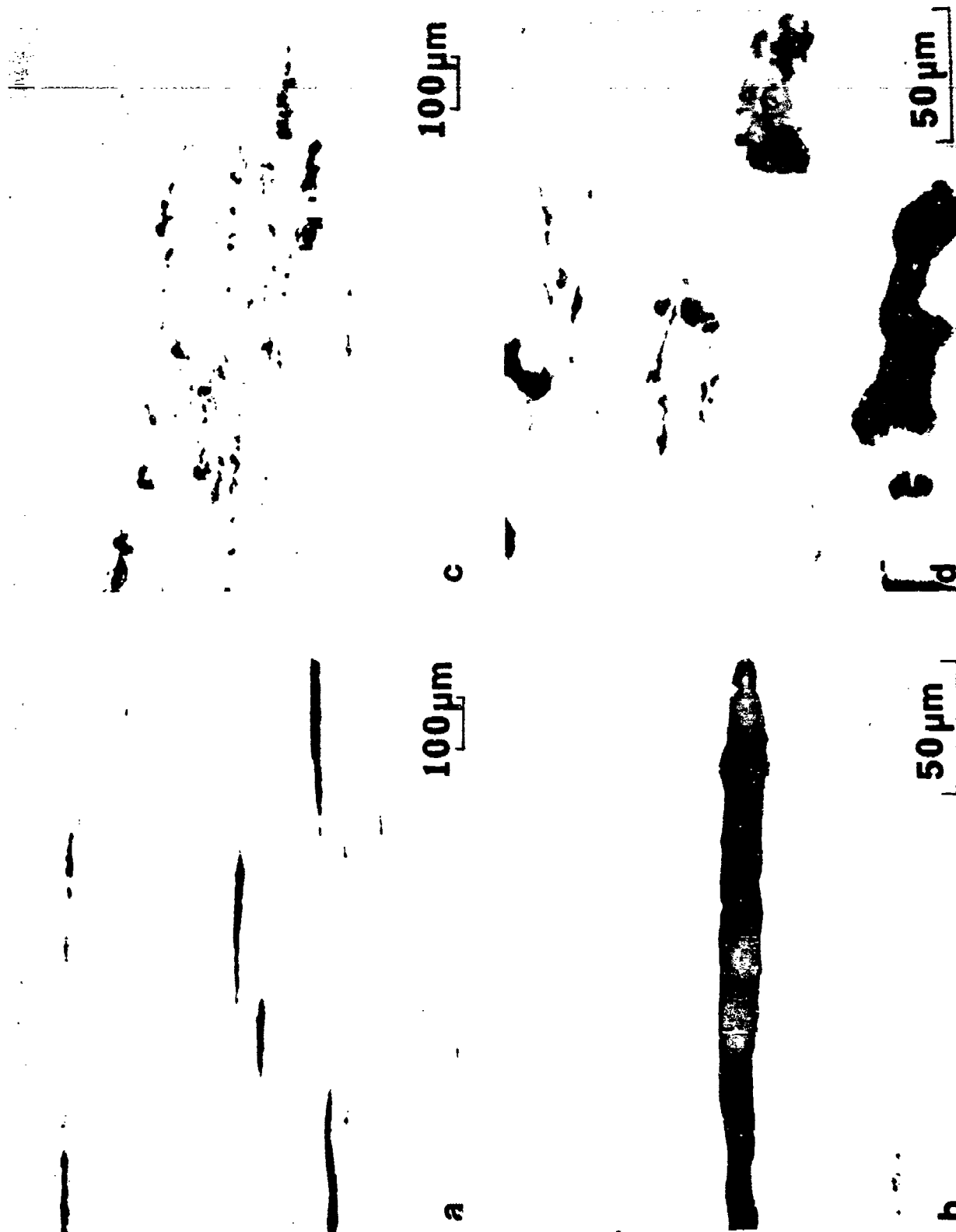
Figure 2. As-polished sections of 7050 extrusions from alloy cast
at a slow rate of solidification; (a) S-number 498823
at 100X, (b) same area as (a) at 500X, (c) S-number
498815 at 100X, and (d) same area as (c) at 500X.
Extrusion conditions for 498823 were high Z and low
ratio, and for 498815 high Z and high ratio.
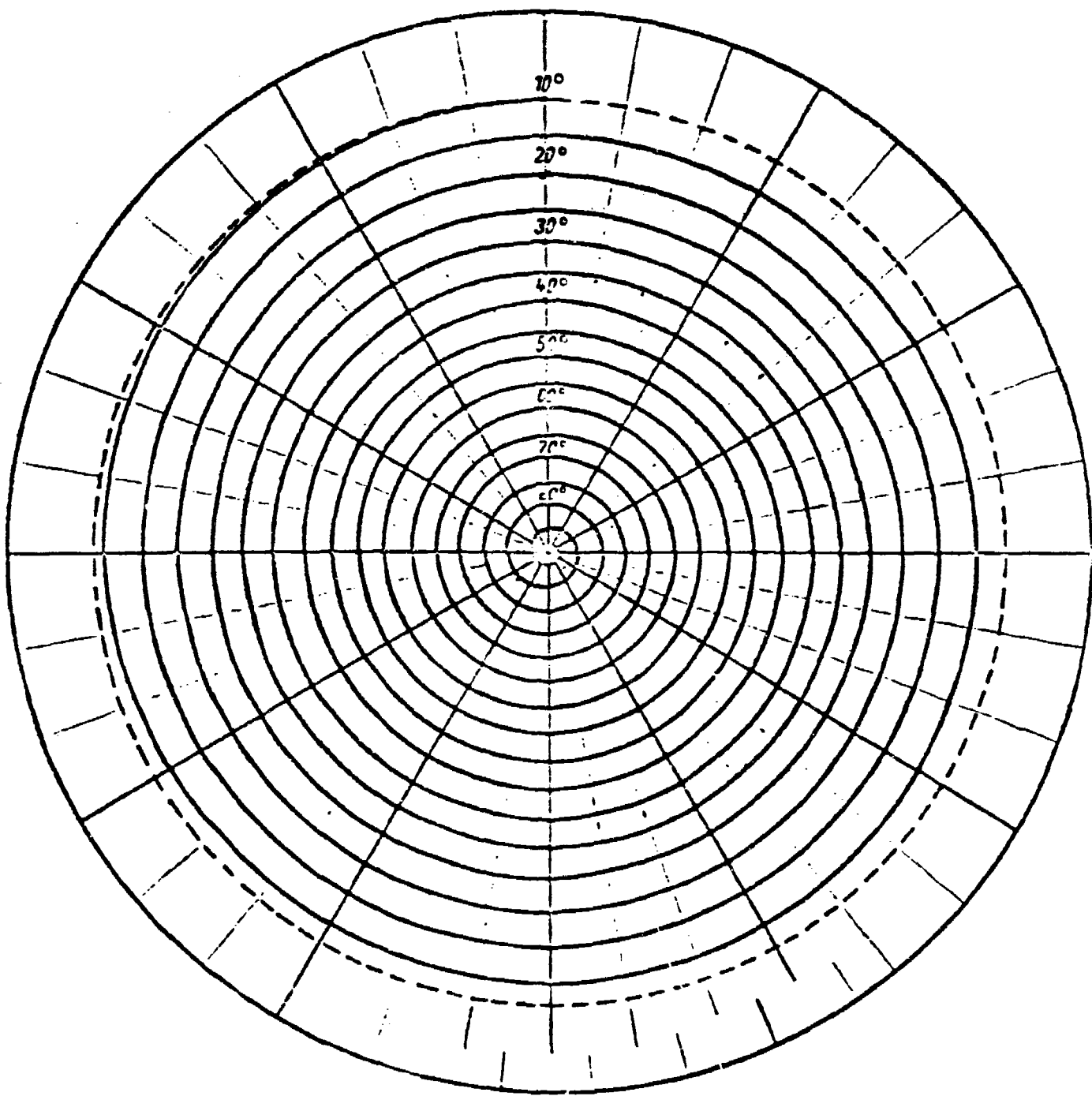
Figure 3. Schematic illustrating the surface area covered on the sphere of reflection.
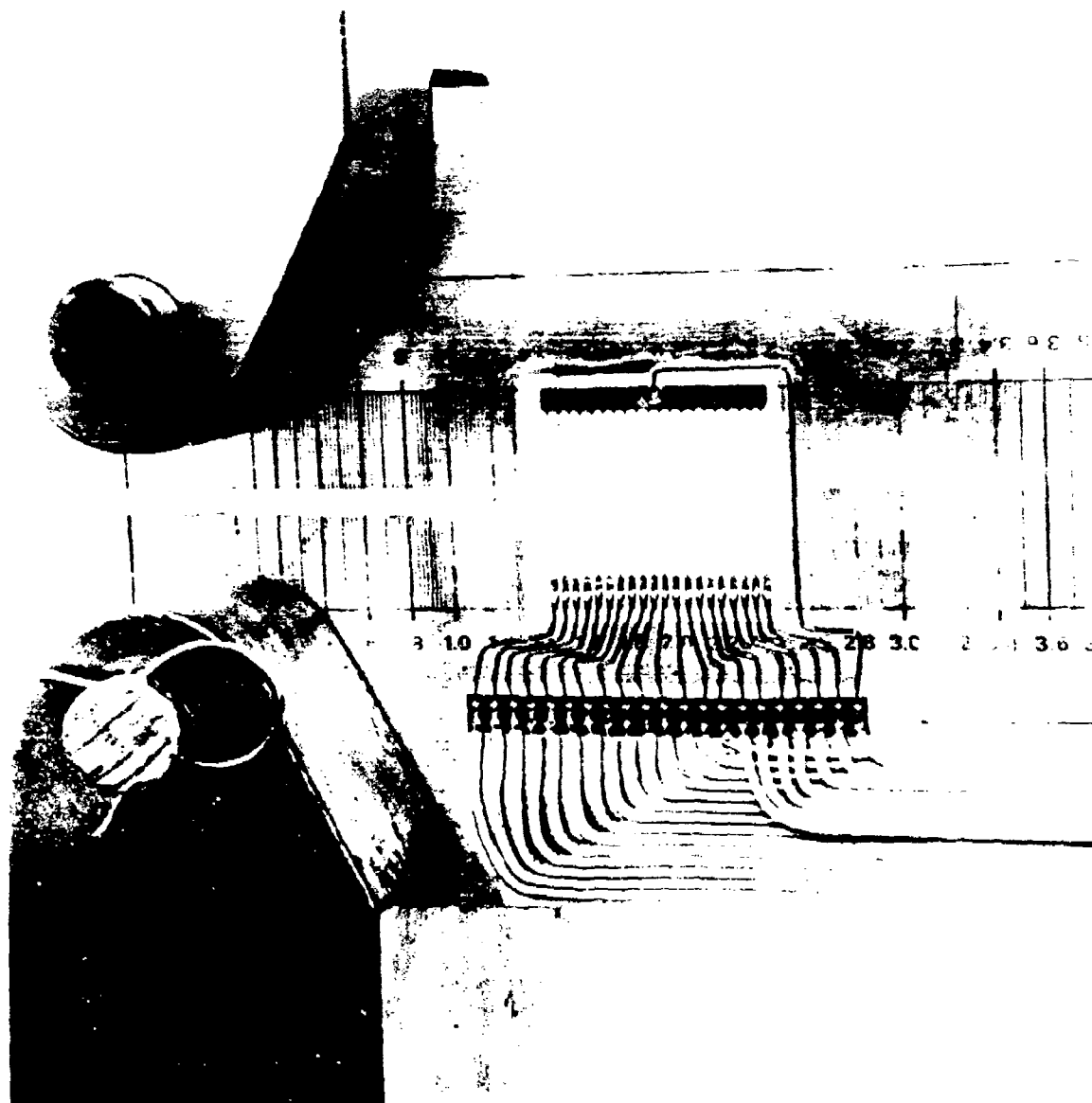
Figure 4. Fatigue crack propagation specimen with propagation gauge.
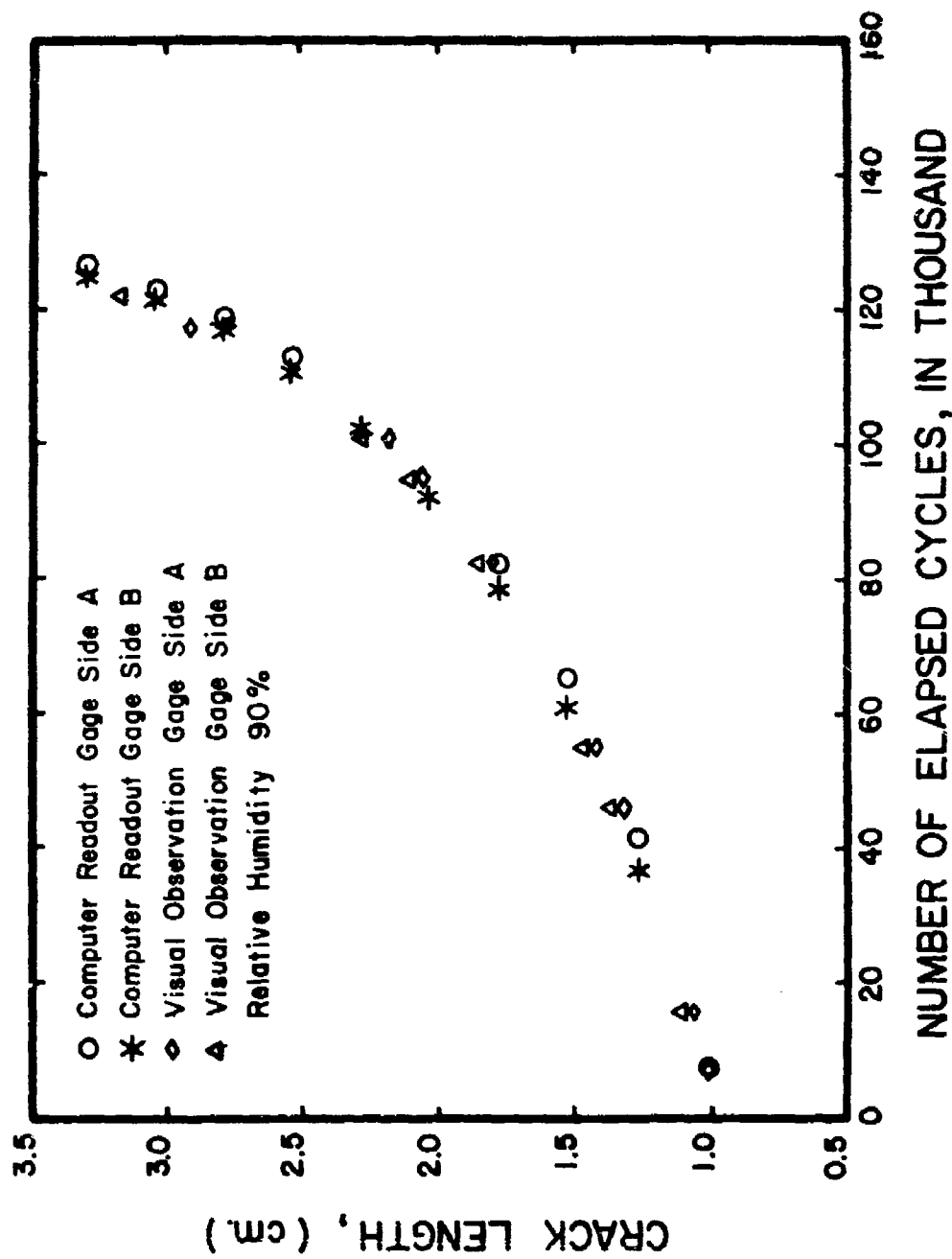
Figure 5. A comparison of crack length versus number of elapsed cycles for a constant amplitude test of alloy 7050-T751 using photogrids and visual observations of the crack growth.
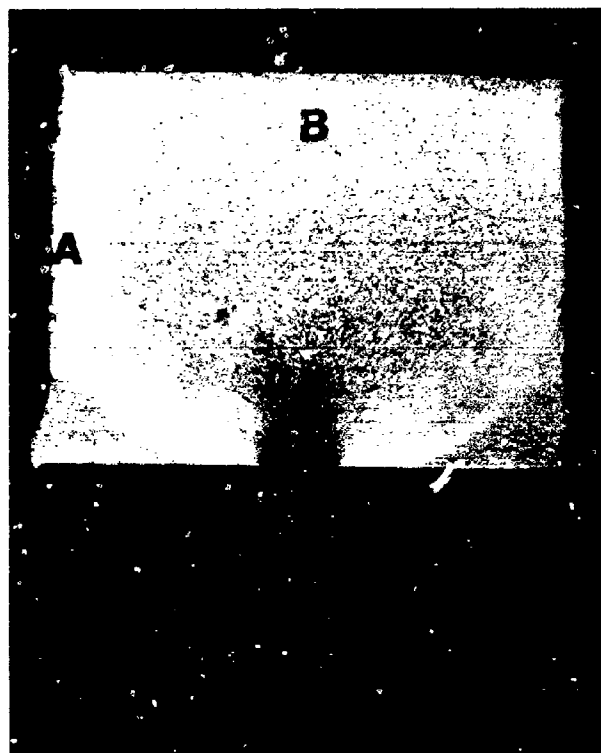
Figure 6.   Photograph of macroetched F-temper billet extruded at high Z, low R.
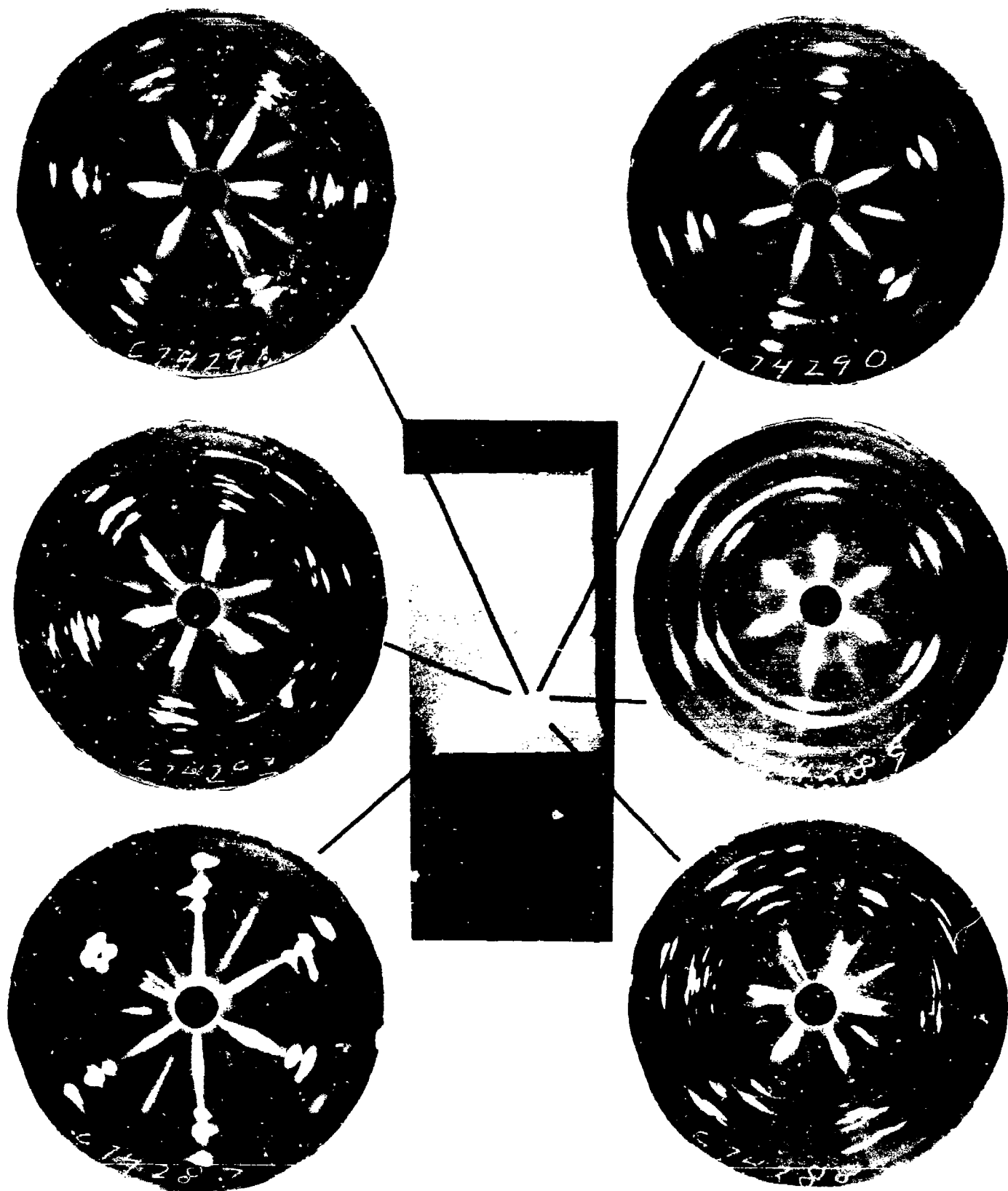
Figure 7. X-ray pinhole photographs taken at several locations in the partially extruded, low Z, low R 7050-F billet
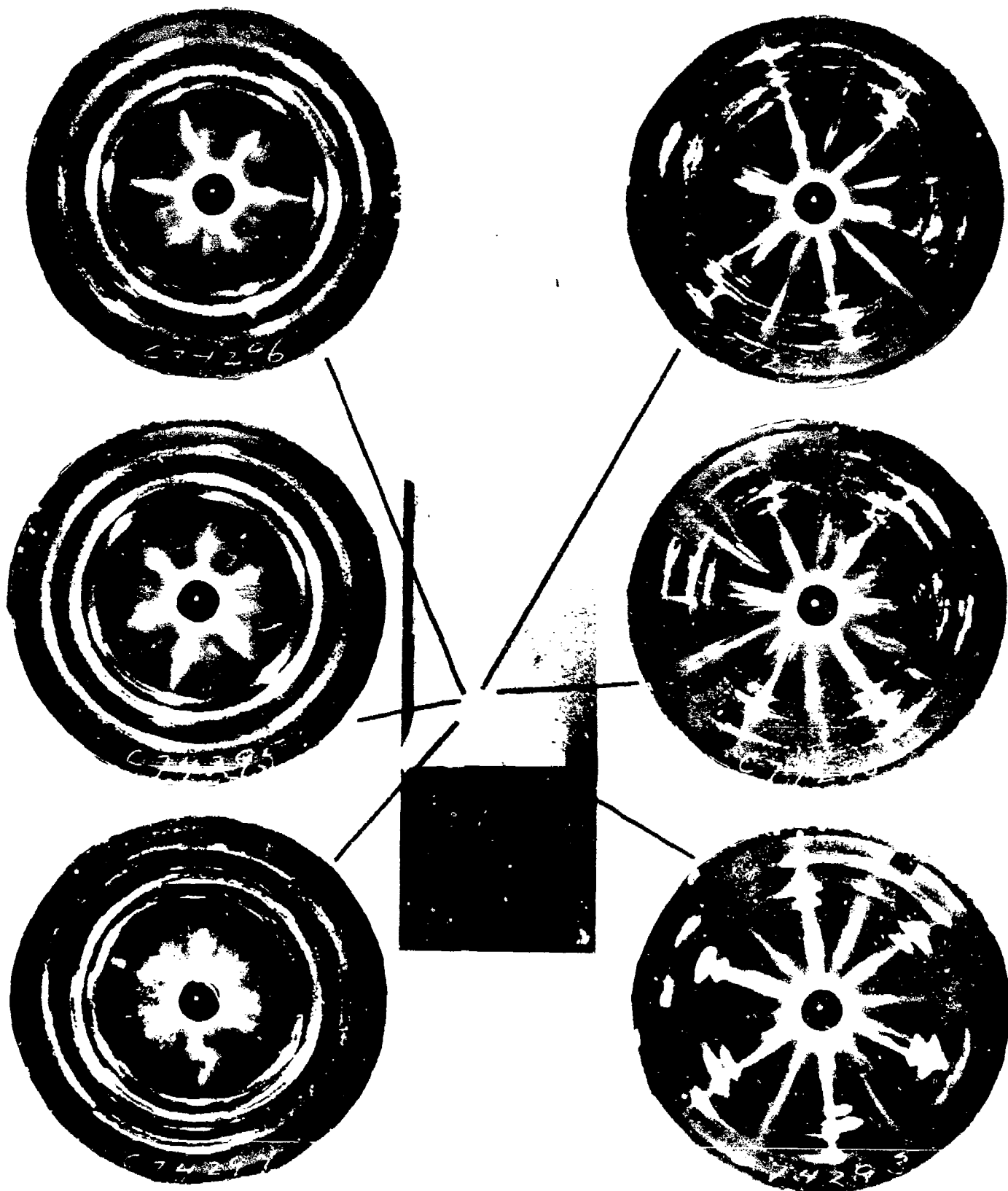
Figure 8. X-ray pinhole photographs taken at several locations in partially extruded, high Z, low R 7050-F billet.
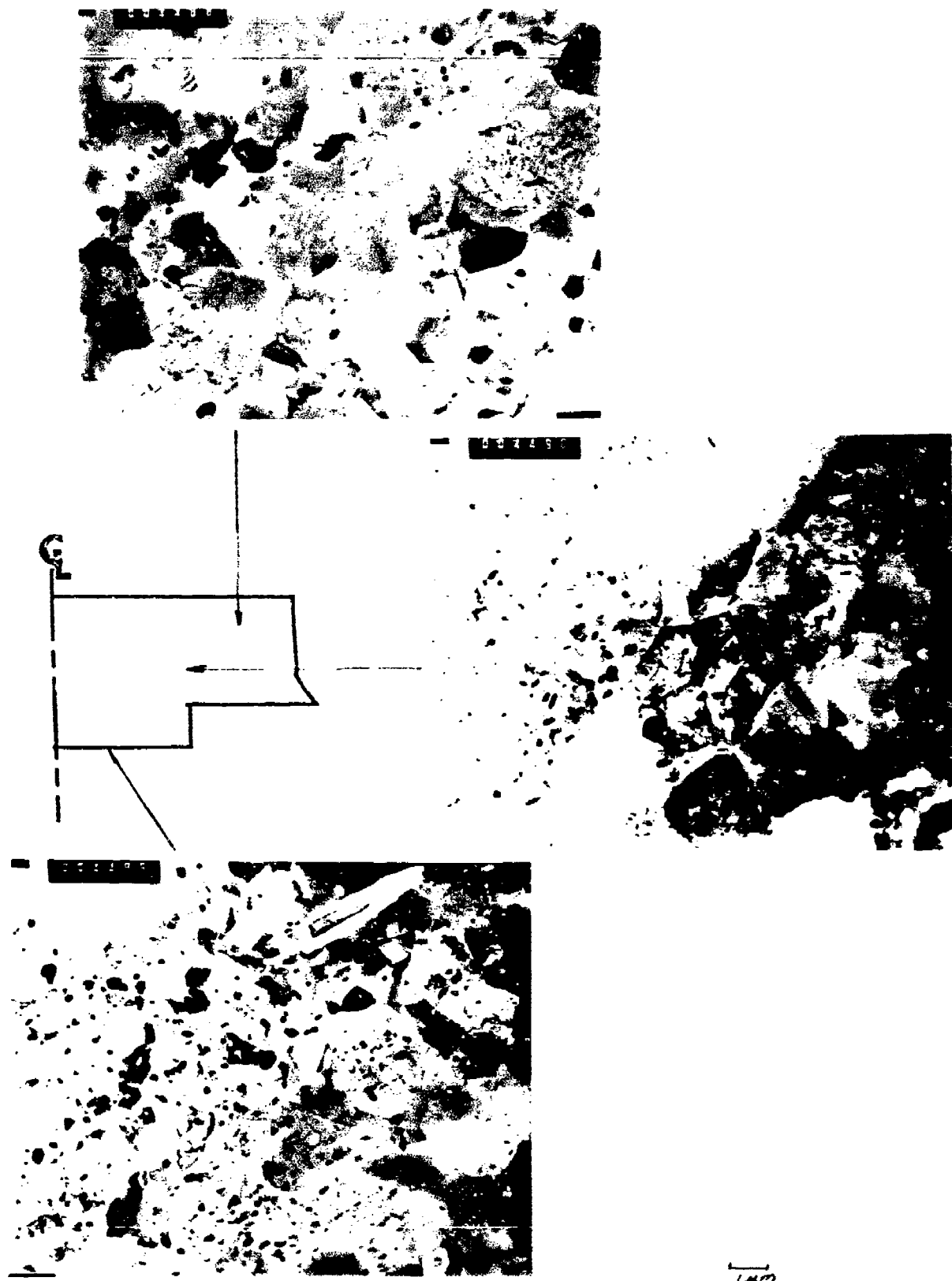
Figure 9.   TEM's taken at several locations in the partially
             extruded low Z, low R 7050-F billet.
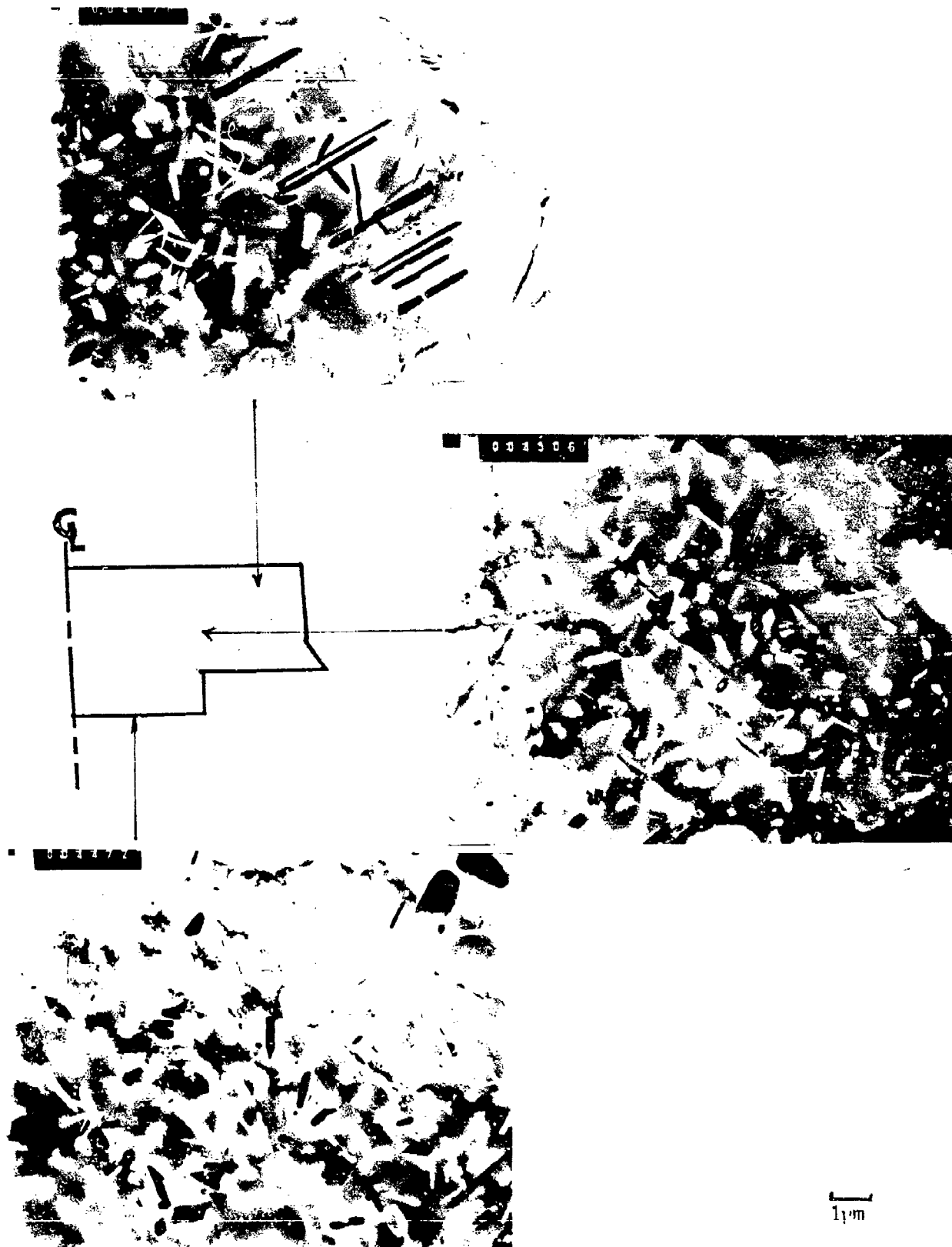
Figure 10.   TEM's taken at several locations in the partially
             extruded high Z, low R 7050-F billet.
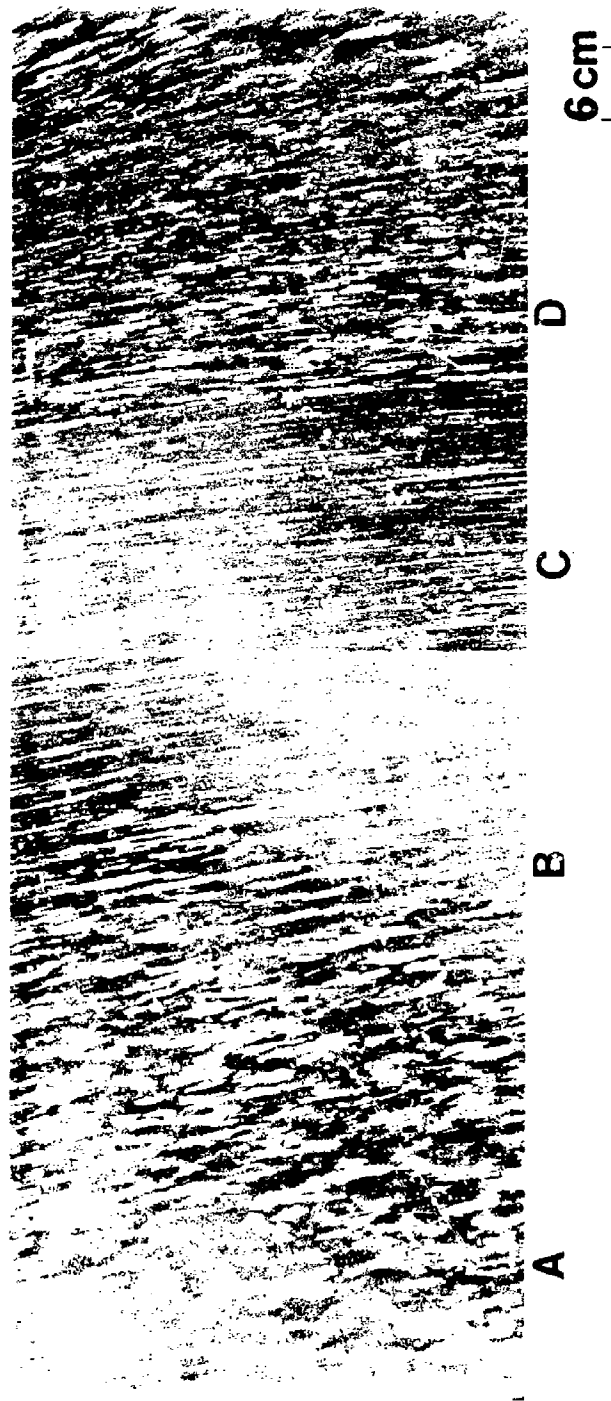
Figure 11. Polarized light micrograph taken across the heavily sheared layer in the high Z, low R extrusion.
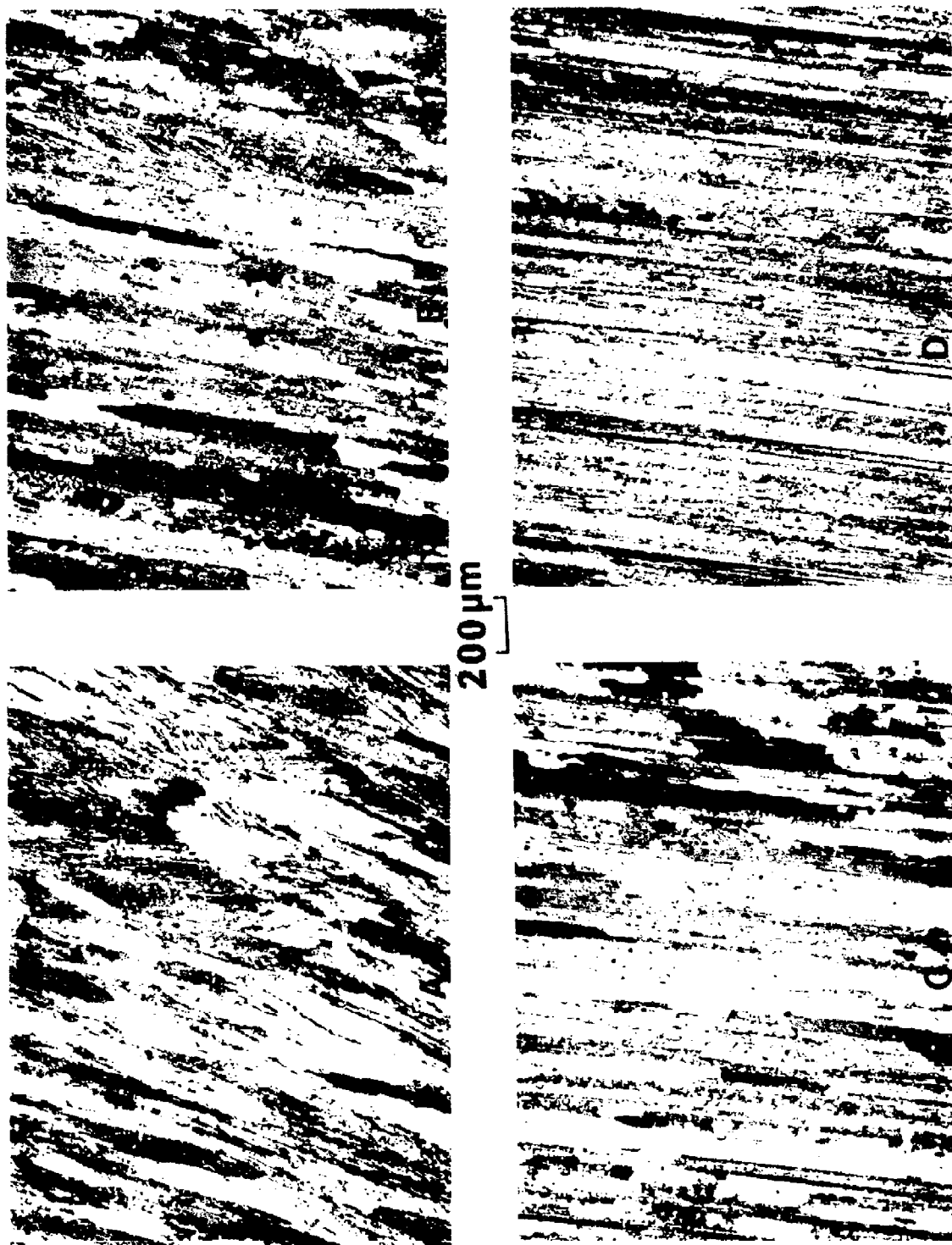
Figure 12. Higher magnification polarized light micrographs of the regions A, B, C, and D defined in Figure 11.
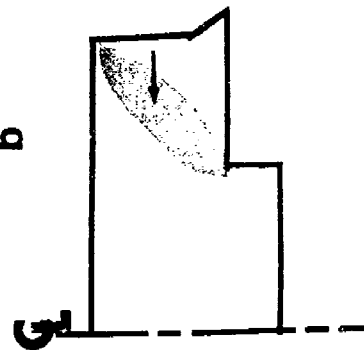
Figure 13. Polarized light micrographs of W-temper 7050 structures near the center of the heavily sheared layer of the (a) low Z, low R and (b) high Z, low R partial extrusions.

100μm
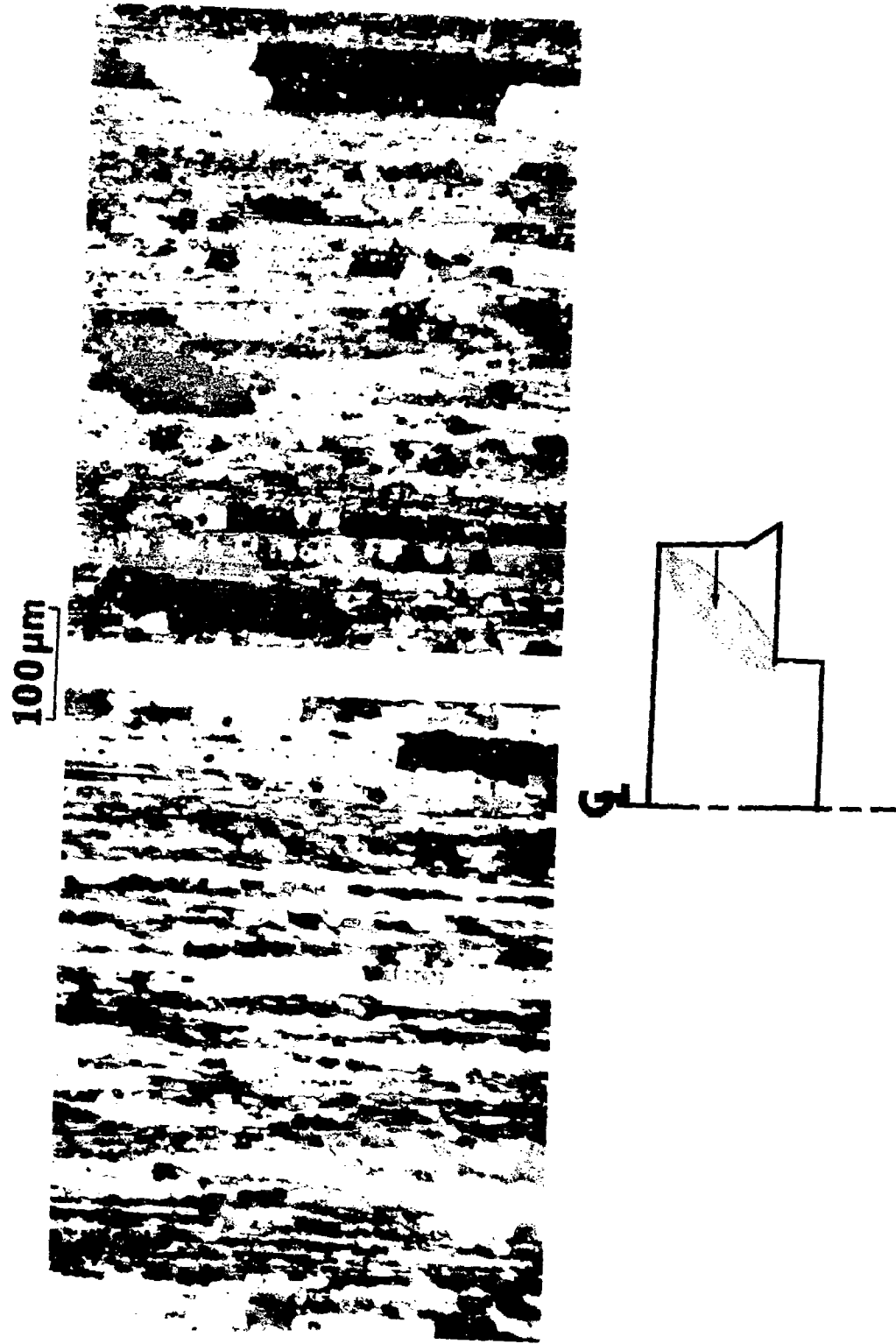
Figure 14. Polarized light micrographs of W-temper grain structures near the center of the heavily sheared layer of the (a) low Z and high R and (b) high Z, high R partial extrusions.

low Z
high R

200μm

C_L
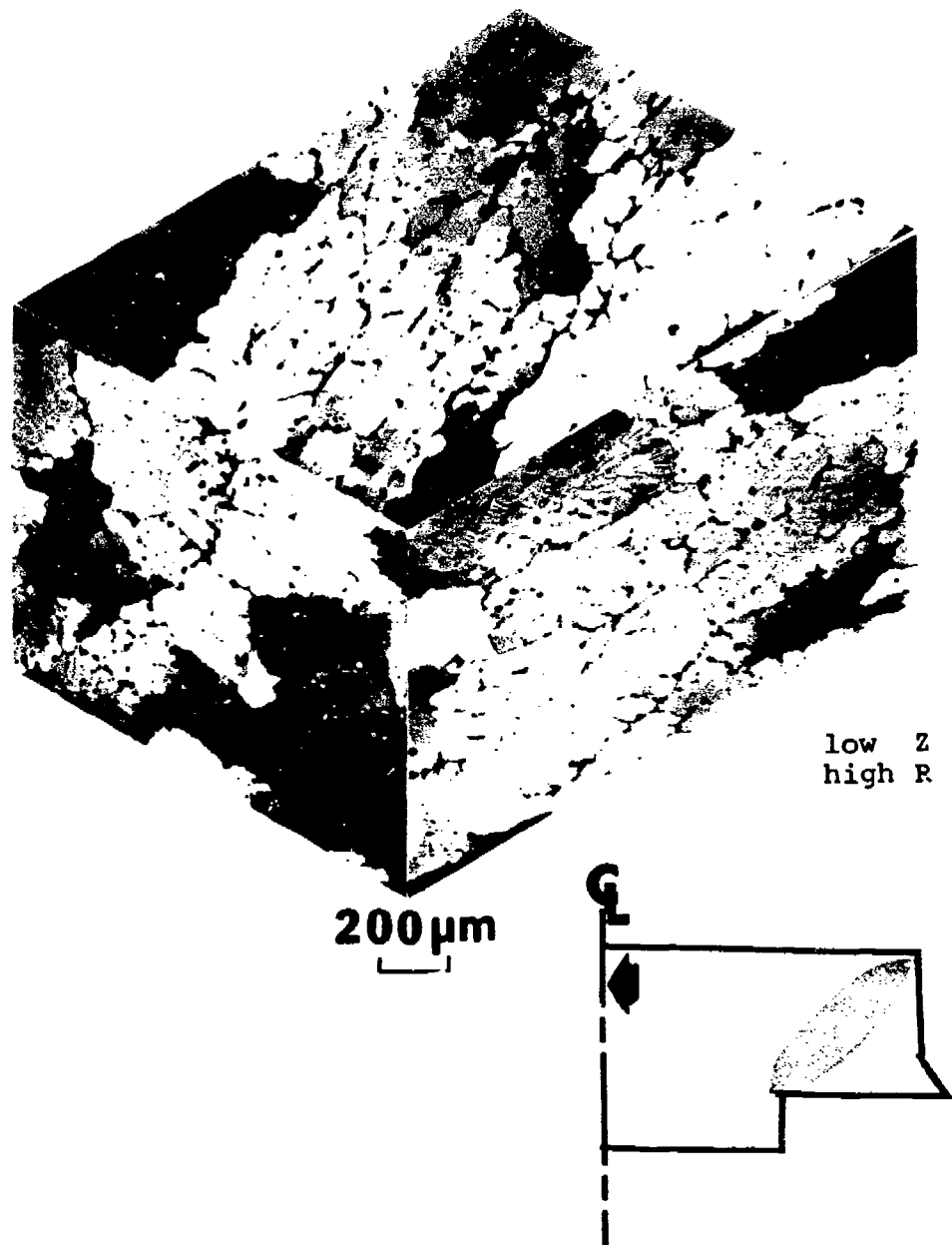
Figure 15.   Three dimensional grain structure from near the rear
of the partially extruded W-temper 7050.

high Z
high R

200 μm
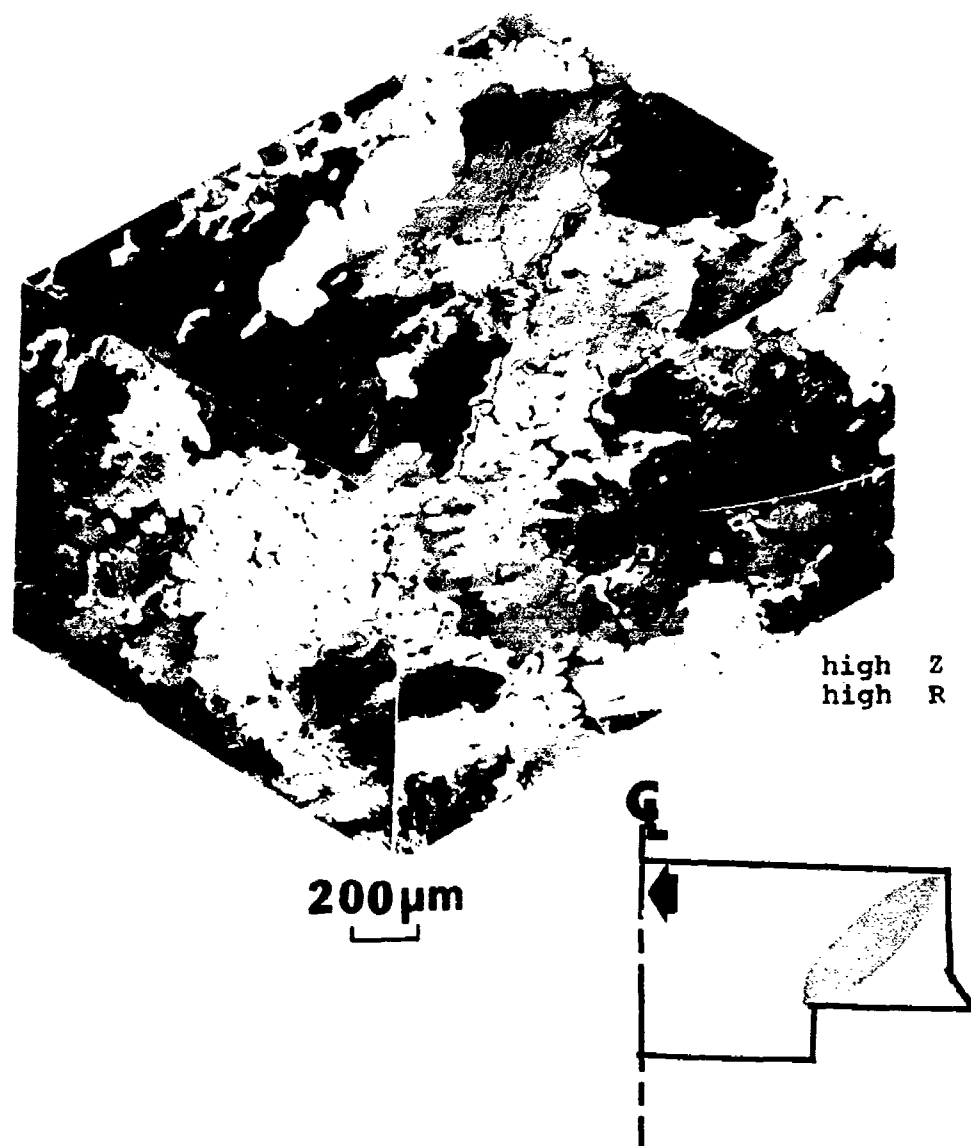
Figure 16.   Three dimensional grain structure from near the rear
              of the partially extruded W-temper 7050.
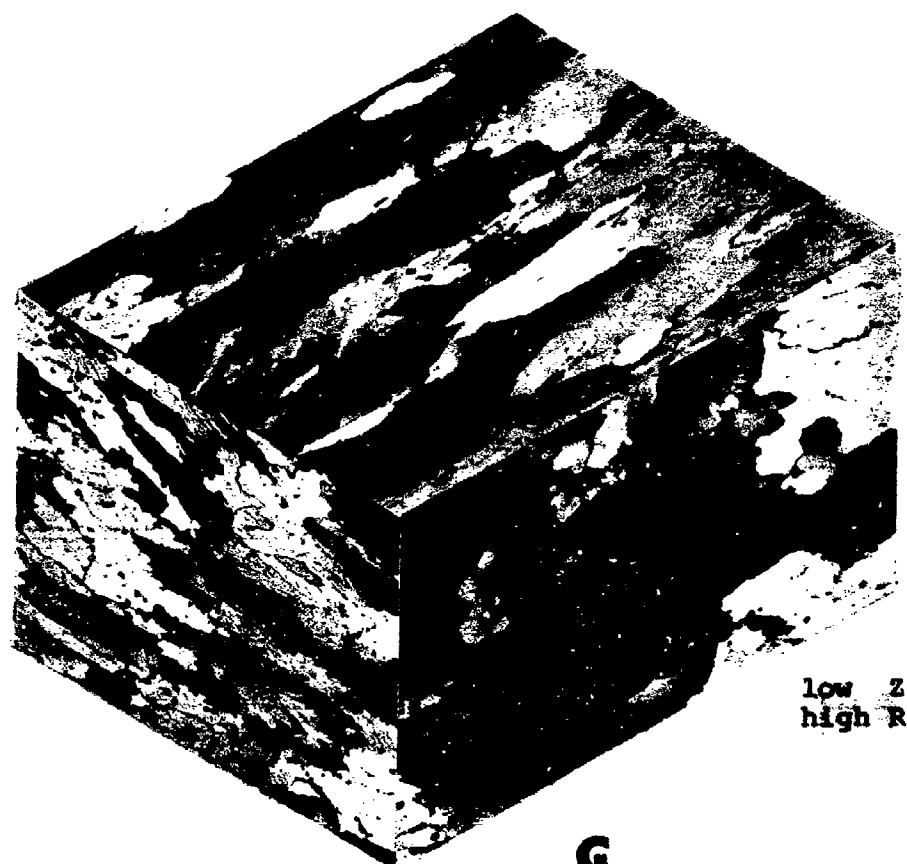
200μm

low Z
high R
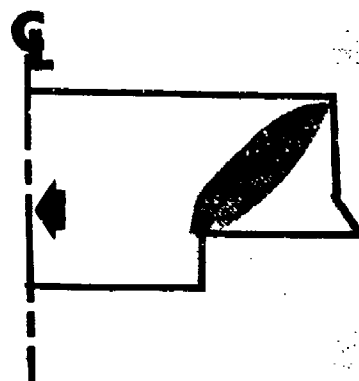
Figure 17. Three dimensional grain structure from near the die
exit of the partially extruded W-temper 7050.

high Z
high R
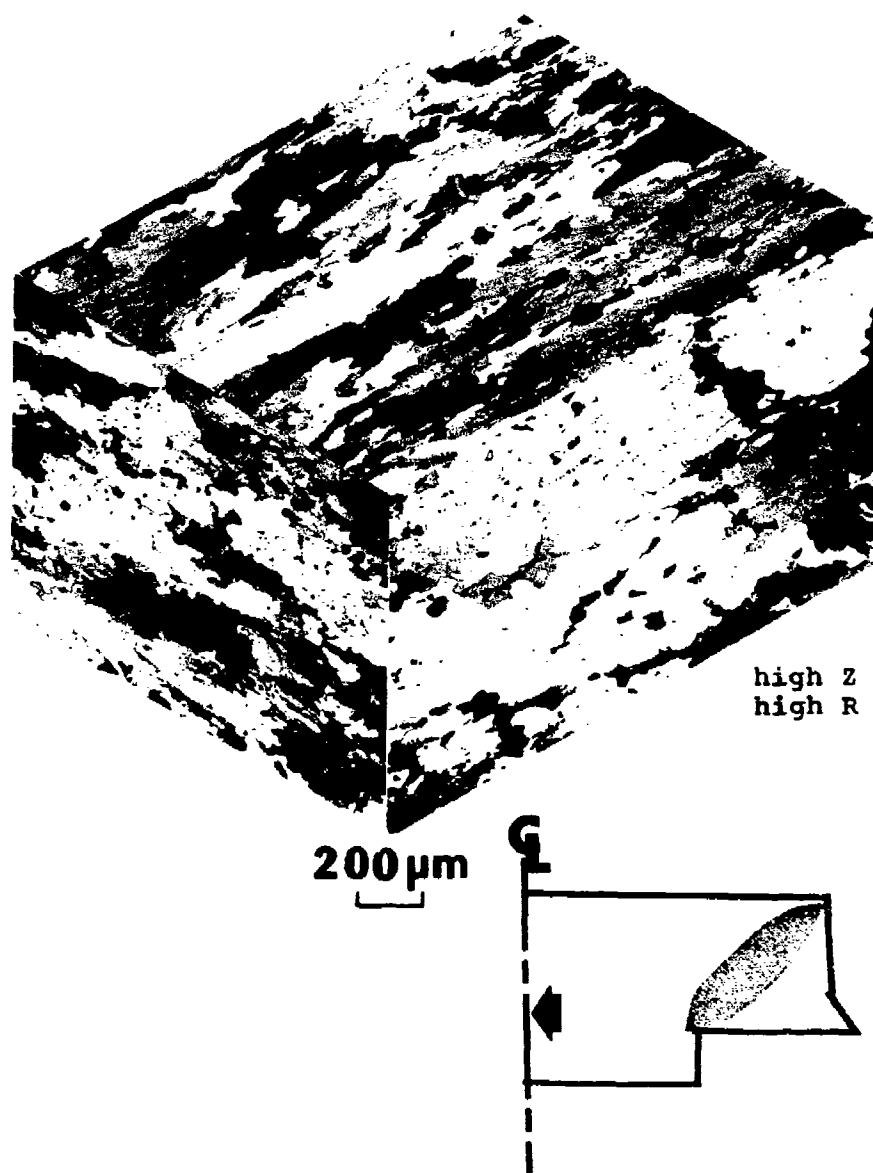
200 μm

Figure 18.   Three dimensional grain structure from near the die
exit of the partially extruded W-temper 7050.
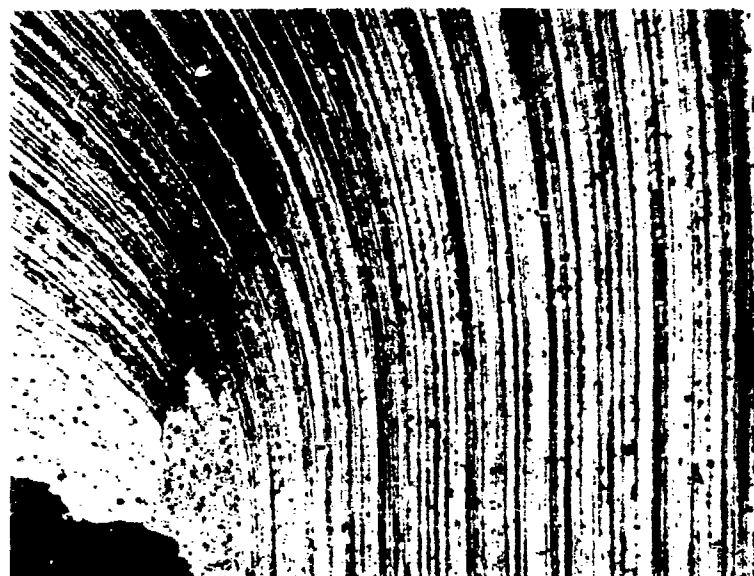
200 µm
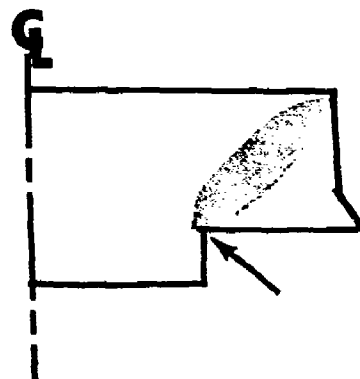
Figure 19. Polarized light micrograph of W-temper 7050 showing the variation of grain structure from surface toward the center of the product in the partially extruded high Z, high R extrusion.
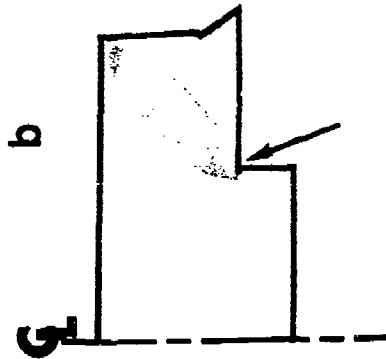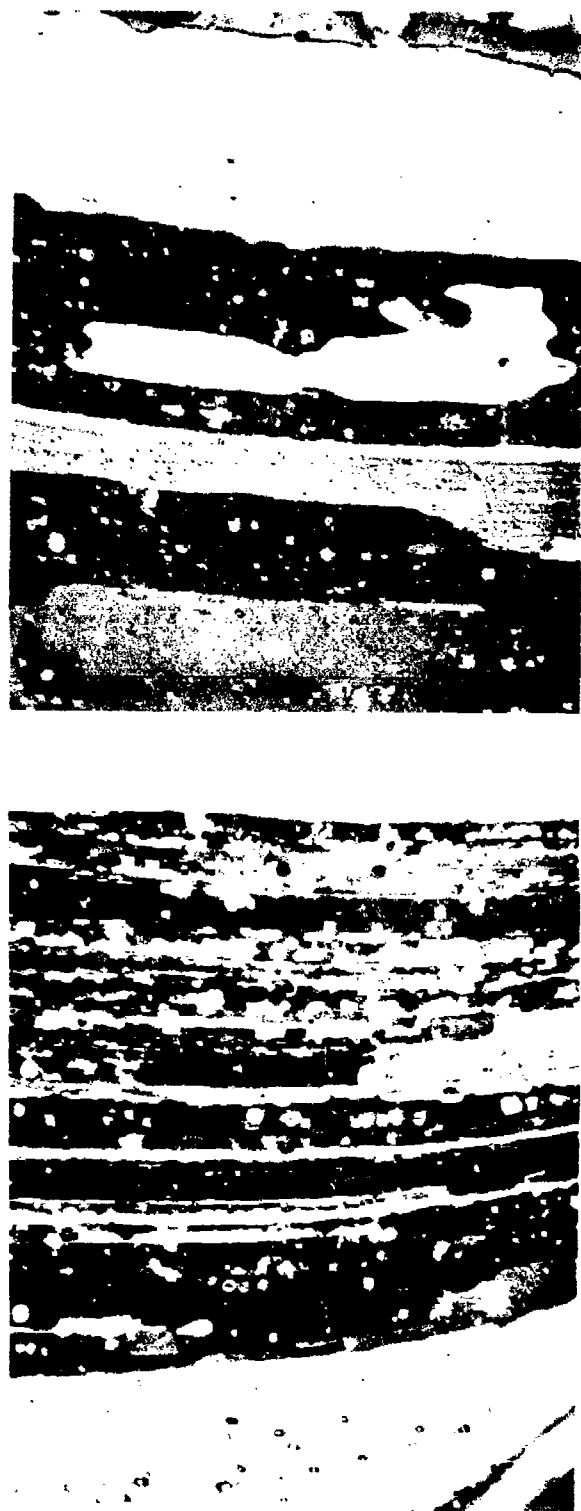
Figure 20. Polarized light micrographs of W-temper 7050 partially extruded billets showing the effect of (a) low Z and low R and (b) high Z and low R extrusion conditions on the grain structure at the die corner.
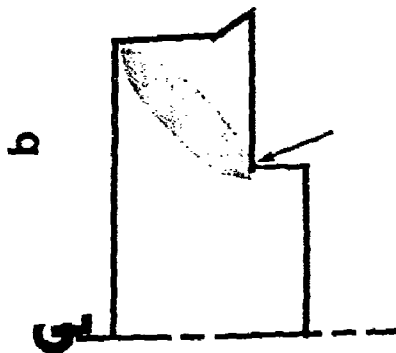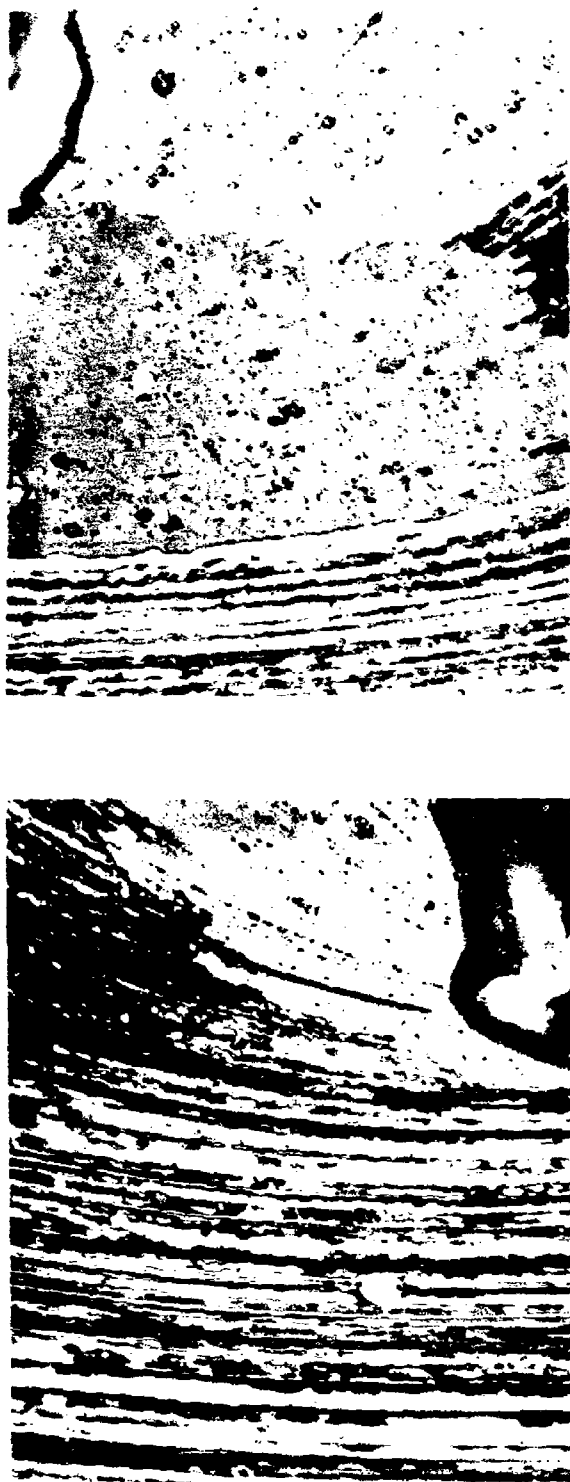
Figure 21. Polarized light micrographs of W-temper 7050 partially extruded billets showing the effect of (a) low Z and high R and (b) high Z and high R extrusion conditions on the grain structure at the die corner.

a   -Z

b   +Z
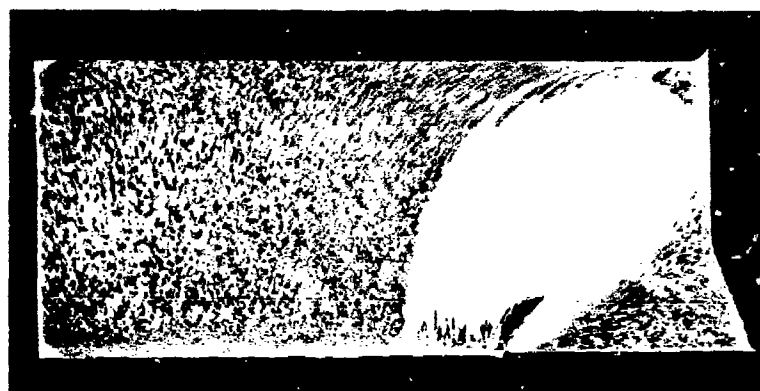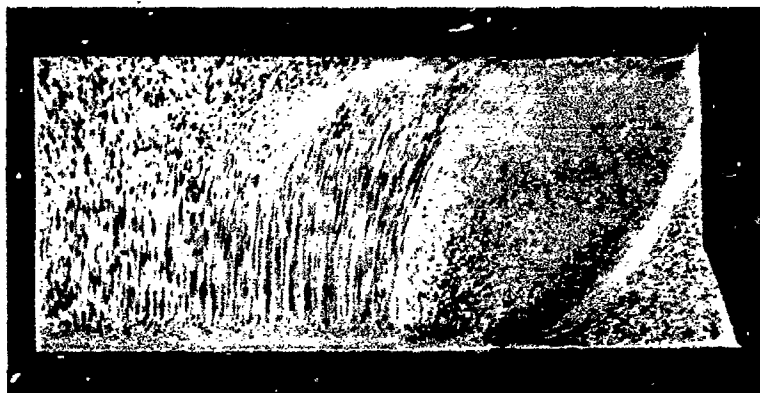
2.5 cm

Figure 22.   Photograph of macroetched W-temper 7050 extrusion;
(a) low Z and low R, and (b) high Z and low R
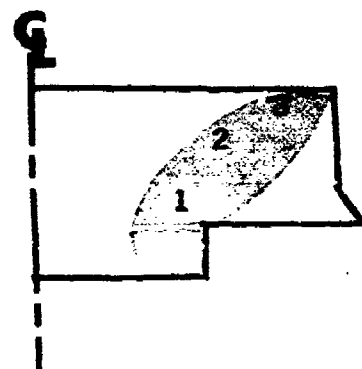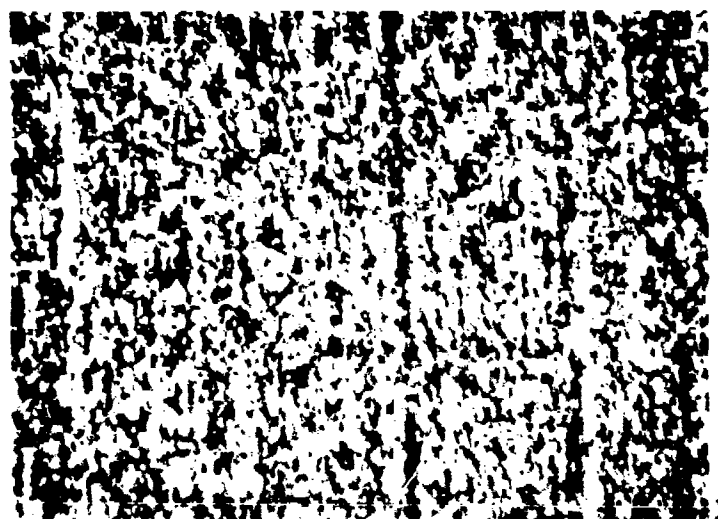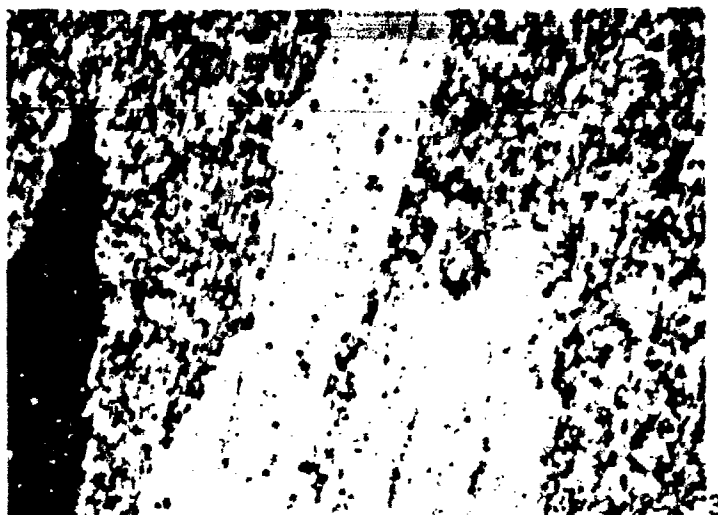
Figure 23. Polarized light micrographs of W-temper 7050 structure in the heavily sheared layer of the butt in the low Z and low R extrusion.
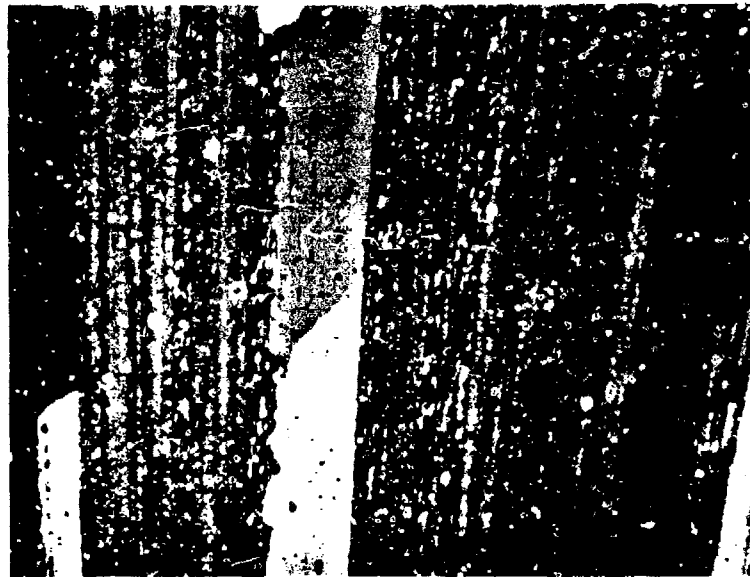
100 μm
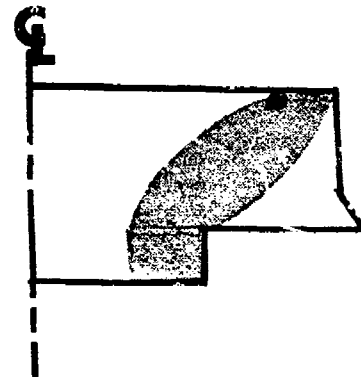
Figure 24. Polarized light micrograph showing the coarse re-crystallized grains associated with the tears in the low Z and low R 7050 extrusion.
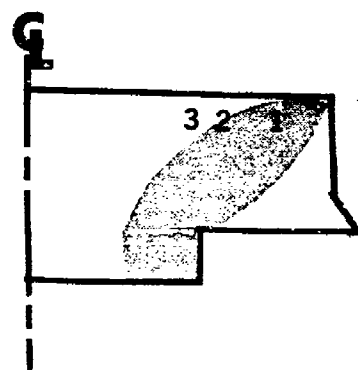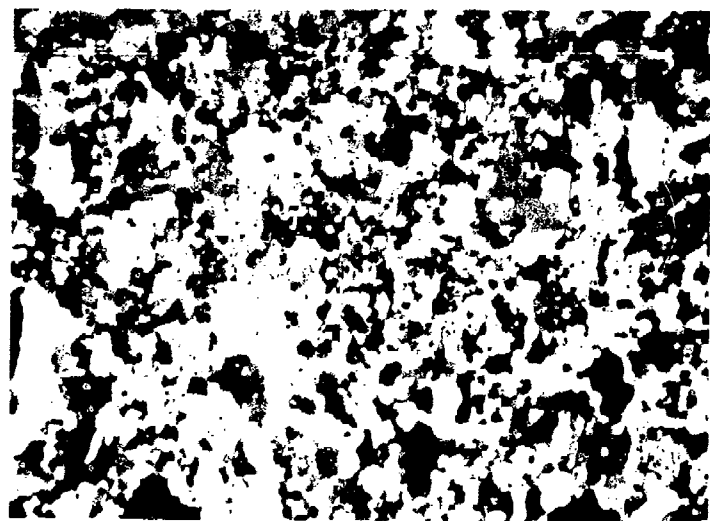
Figure 25. Polarized light micrograph of W-temper 7050 structure in the vicinity of the heavily sheared layer in the high Z low R extrusion.
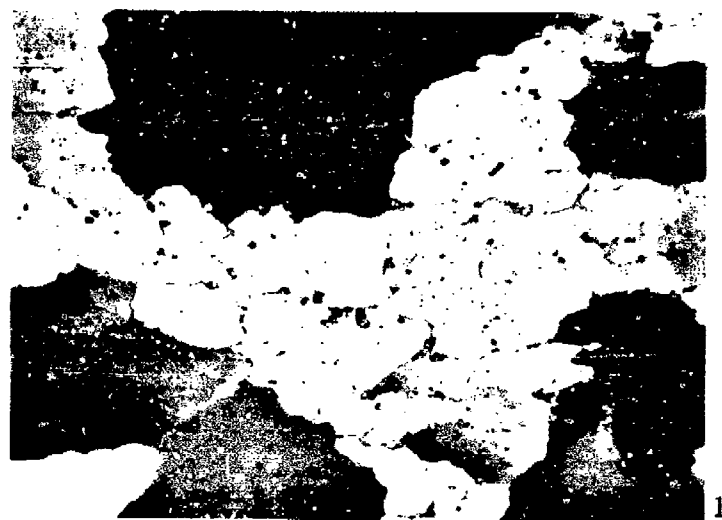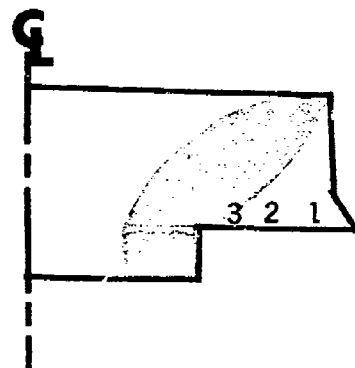
Figure 26. Polarized light micrographs of the W-temper 7050 in the vicinity of the heavily sheared layer in the low Z low R extrusion.
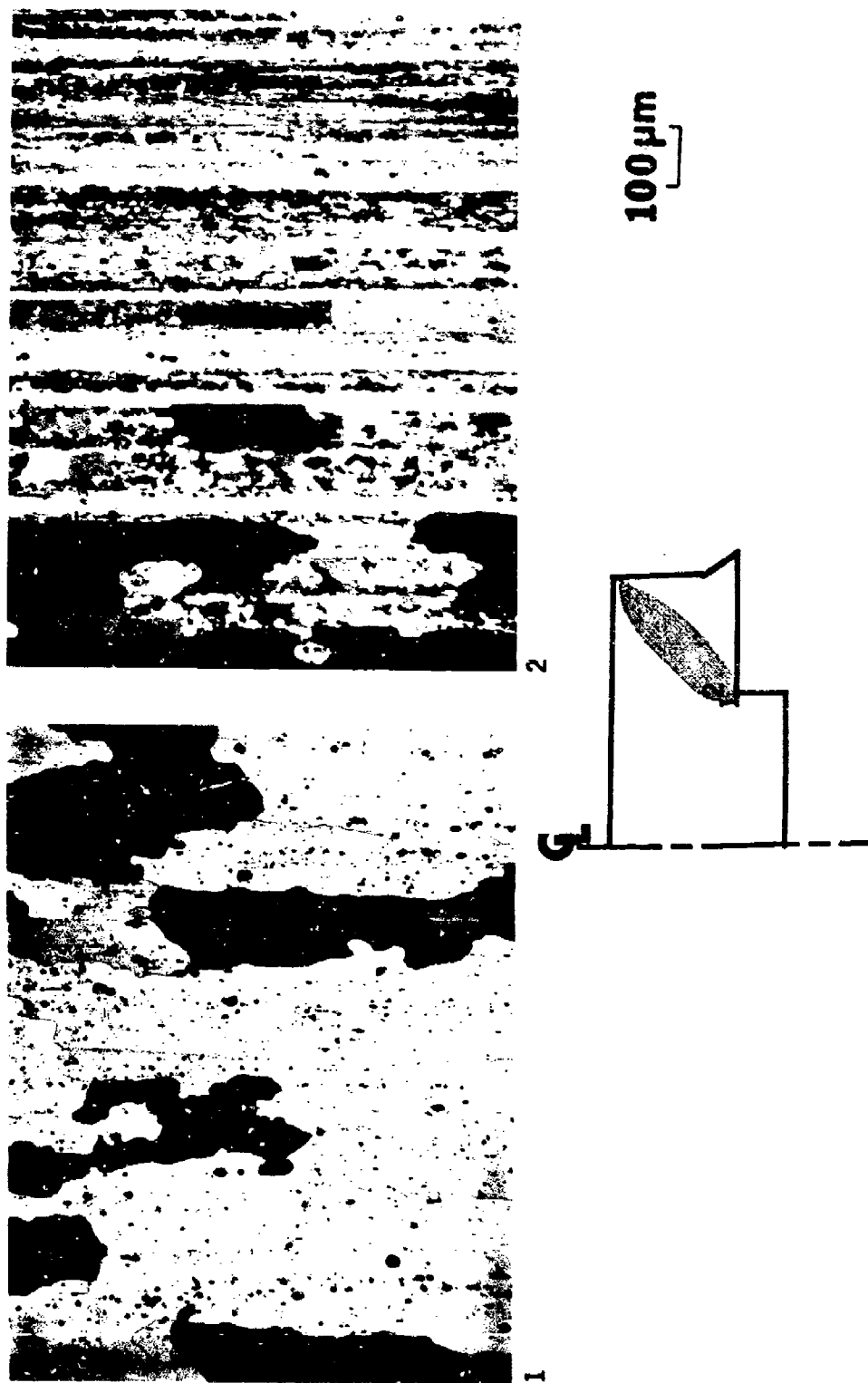
Figure 27. Polarized light micrograph of the W-temper 7050 in the vicinity of the heavily sheared layer in the high Z low R extrusion.
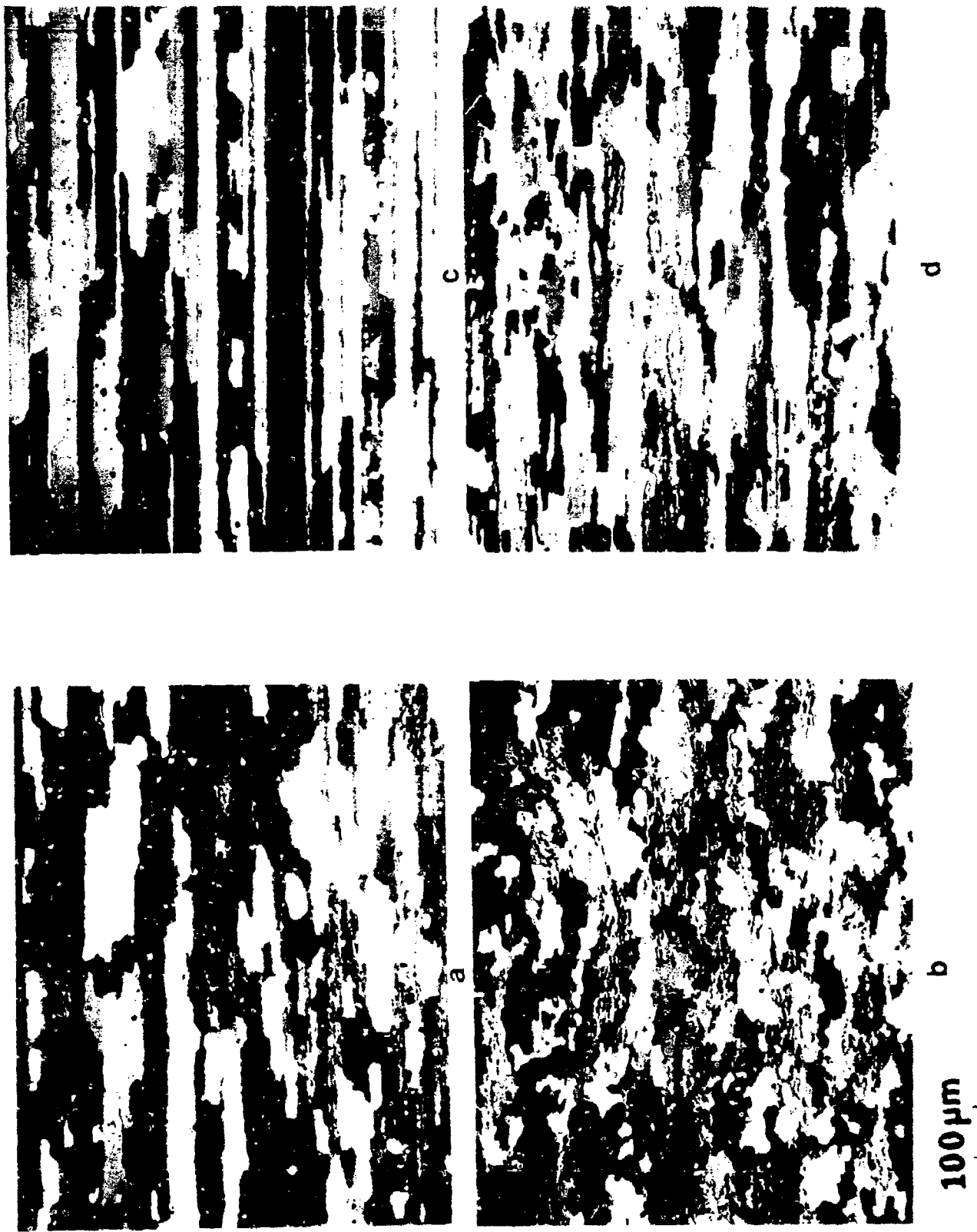
100μm
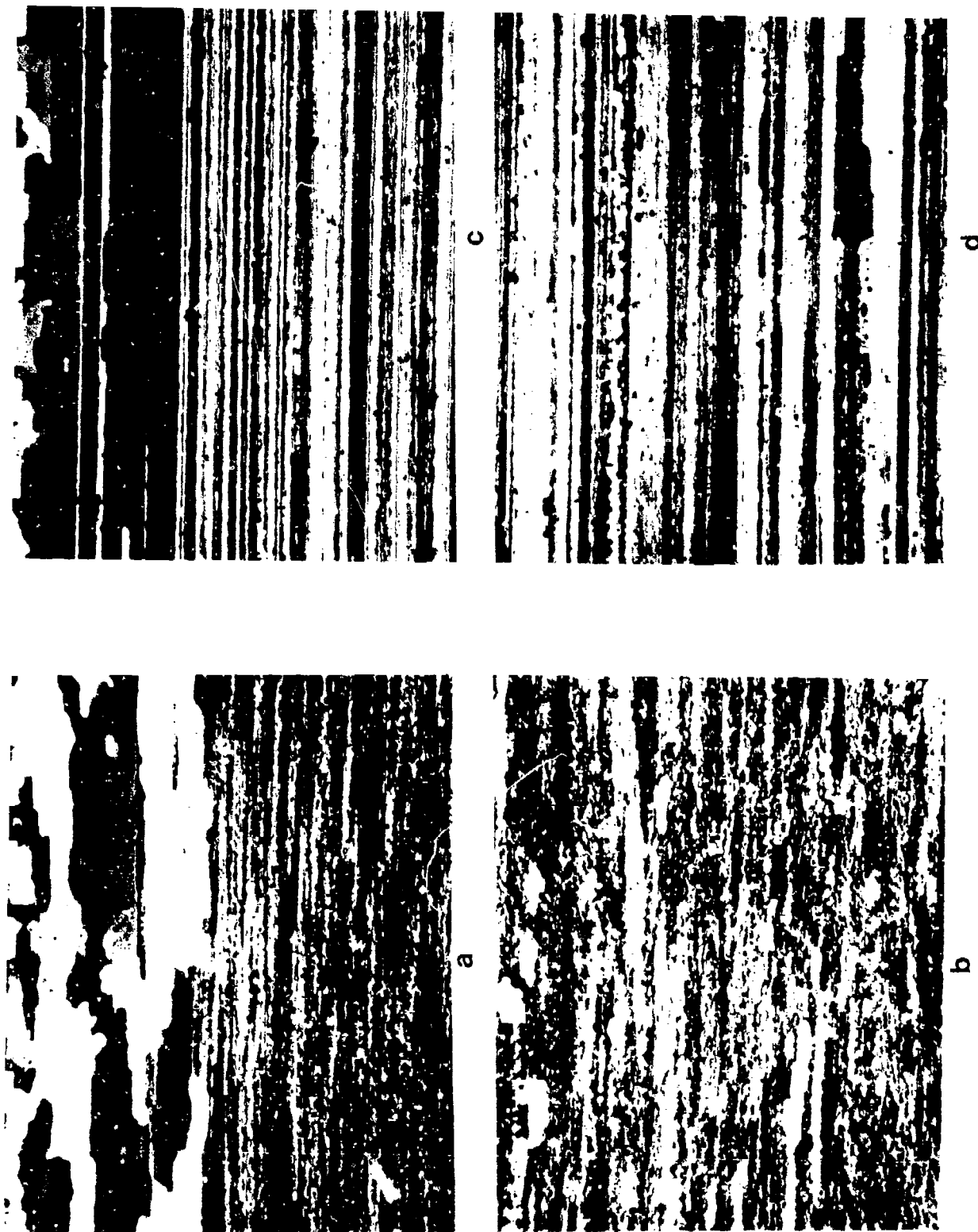
Figure 28.   The microstructure of 7050 extruded under conditions of high Z and high R;
(a) transverse section at surface, (b) transverse section at center, (c)
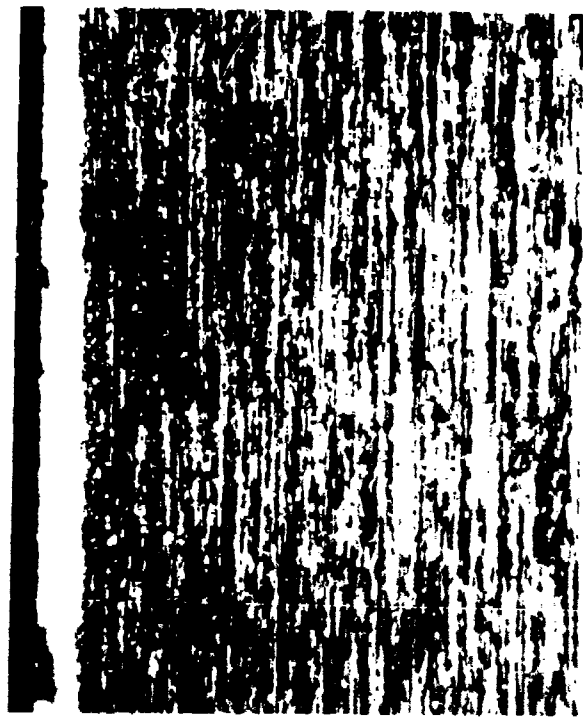longitudinal section at surface, and (d) longitudinal section at center.
(S#498816)
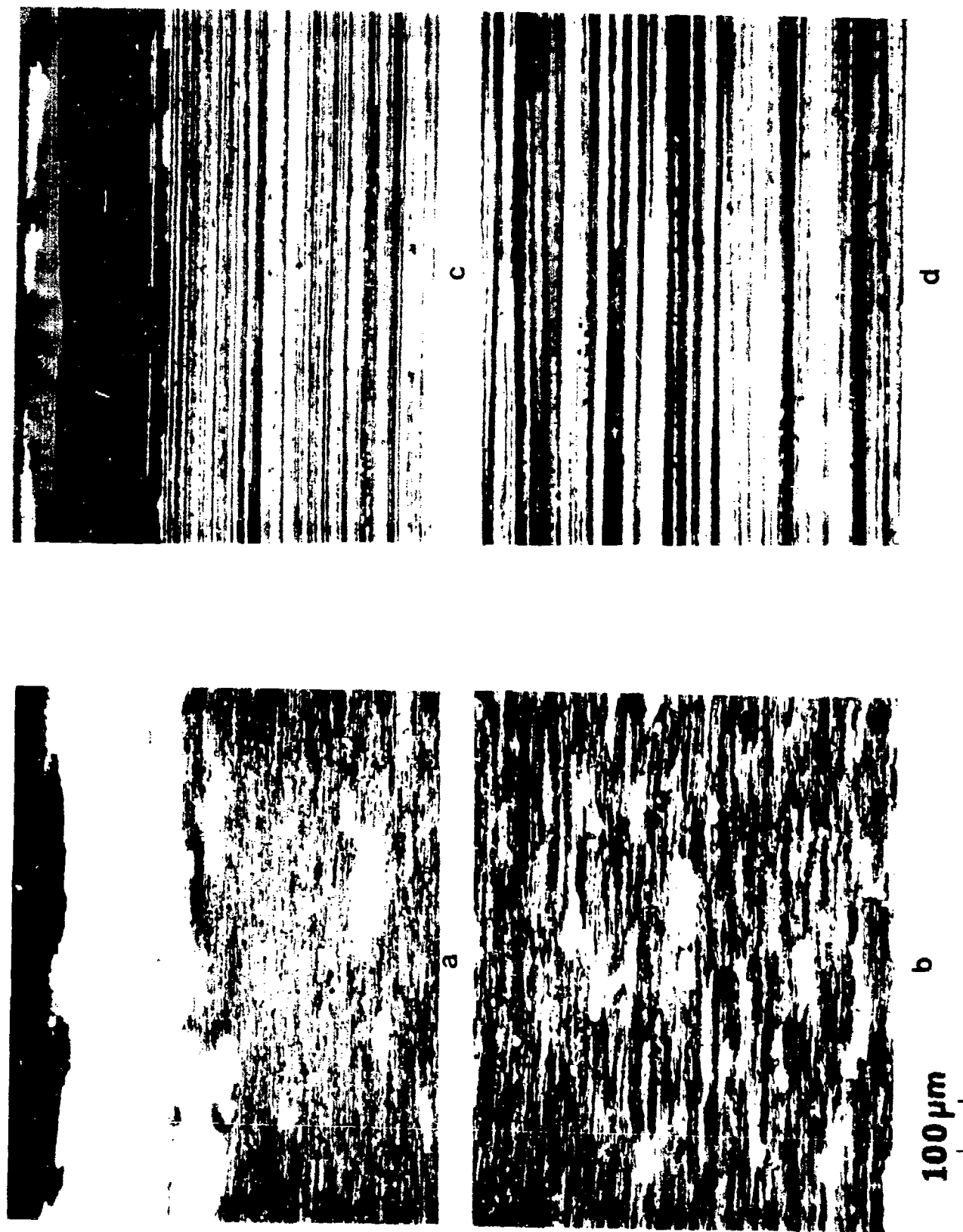
100μm

Figure 29. The microstructure of 7475 extruded under conditions of high Z and high R; (a) transverse section at surface, (b) transverse section at center, (c) longitudinal section at surface, and (d) longitudinal section at center.
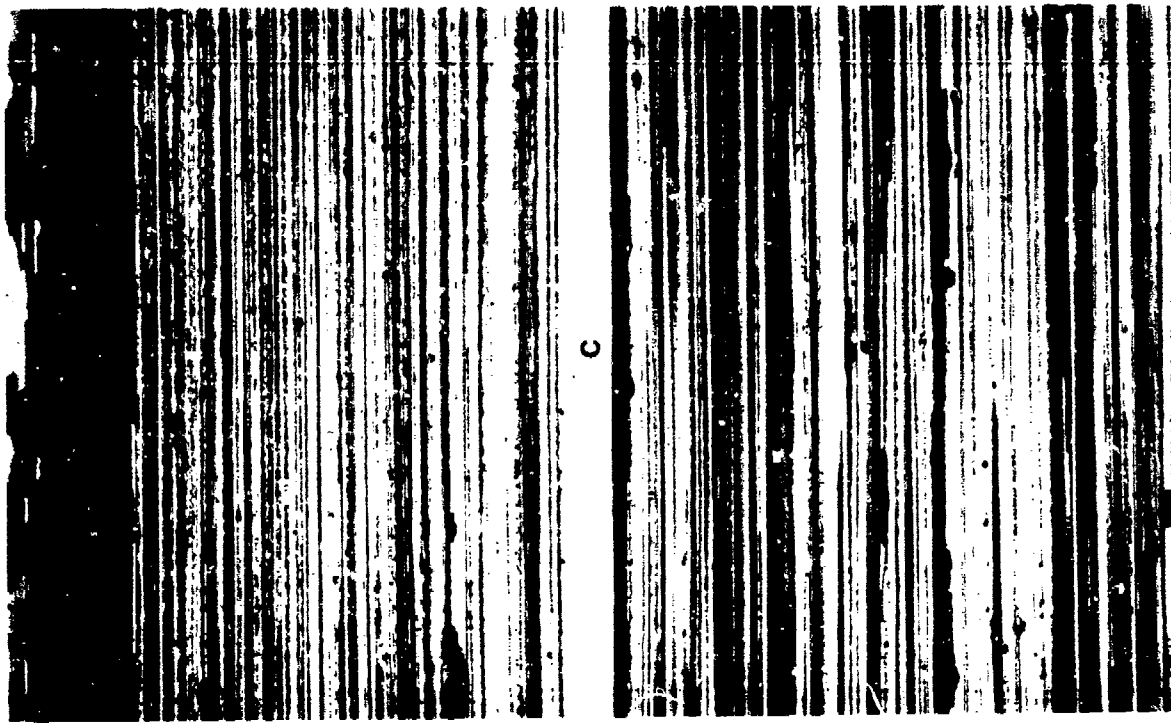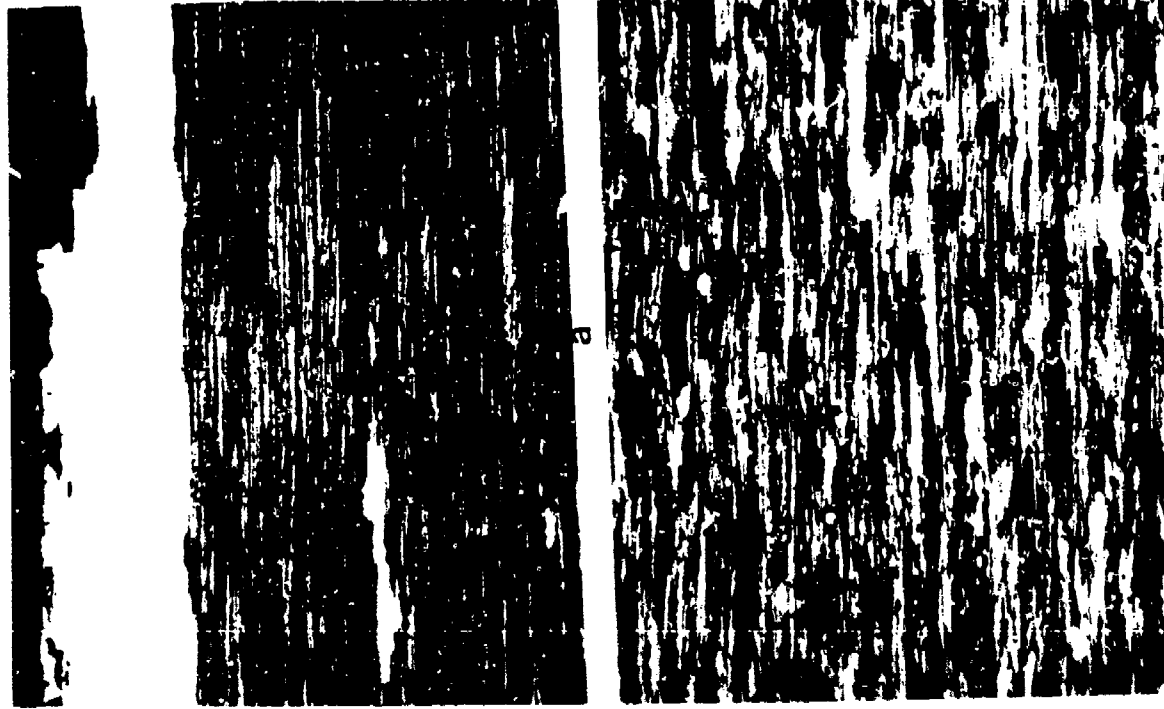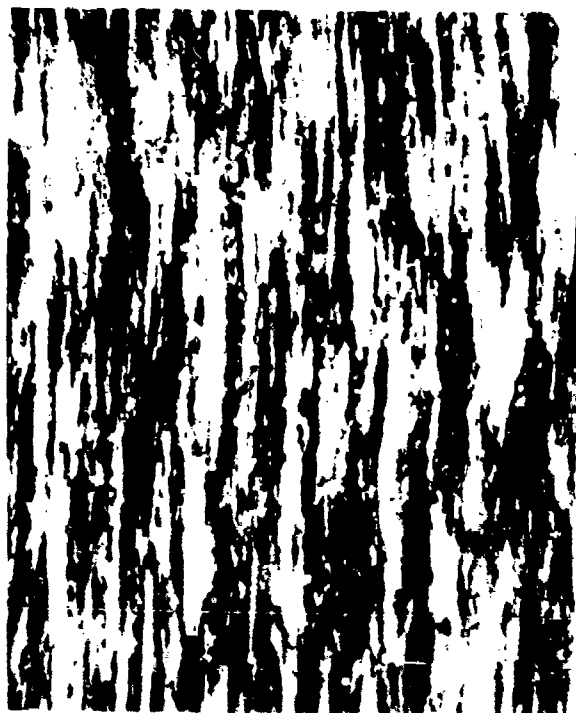
Figure 30. The microstructure of 7475 extruded under conditions of high Z and high R; (a) transverse section at surface, (b) transverse section at center, (c) longitudinal section at surface, and (d) longitudinal section at center.

Figure 31. The microstructure of 7050 extruded under conditions of high Z and low R;
(a) transverse section at surface, (b) transverse section at center, (c)
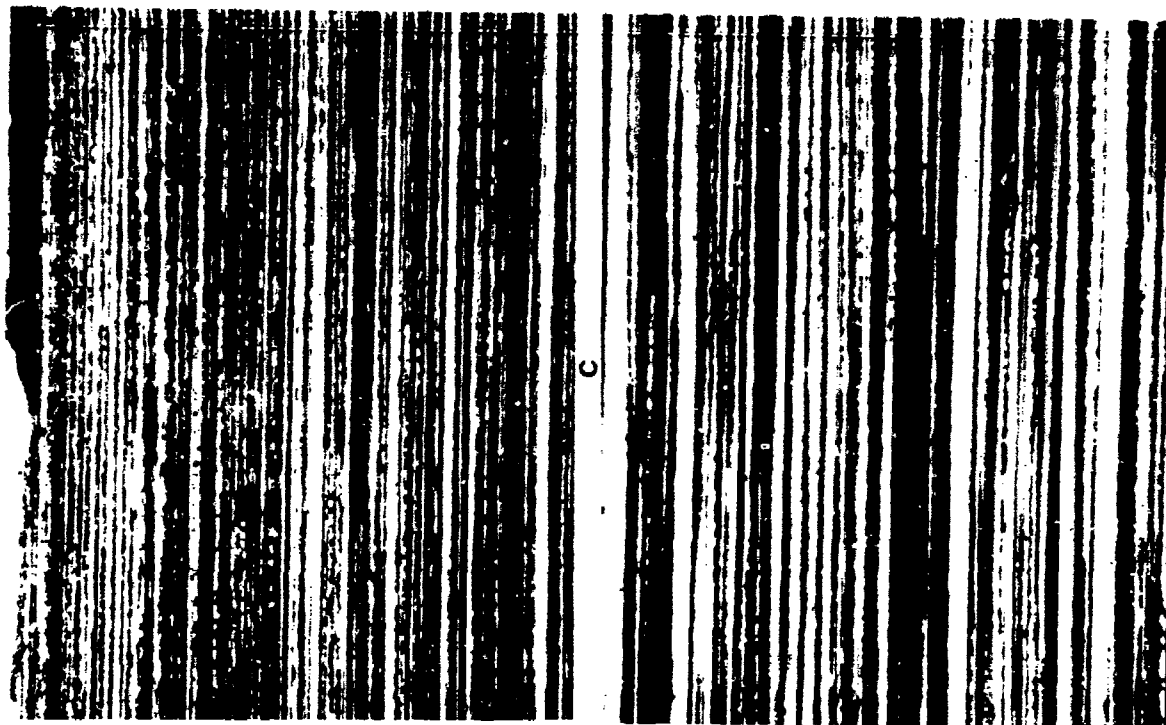longitudinal section at surface, and (d) longitudinal section at center.
(SM 40910)

100μm

Figure 32. The microstructure of 7475 extruded under conditions of high Z and low R; (a) transverse section at surface, (b) transverse section at center, (c) longitudinal section at surface, and (d) longitudinal section at center. (S# 498811)

100μm

Figure 33. The microstructure of 7475 extruded under conditions of high Z and low R:
(a) transverse section at surface, (b) transverse section at center, (c)
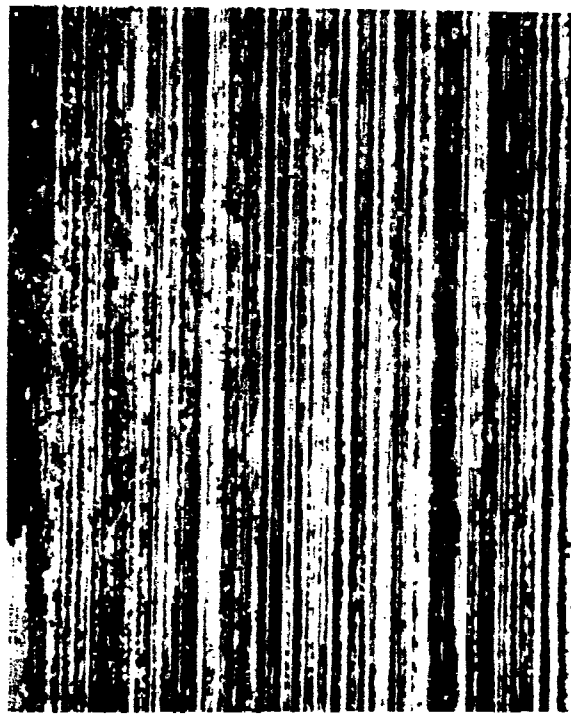longitudinal section at surface, and longitudinal section at center.
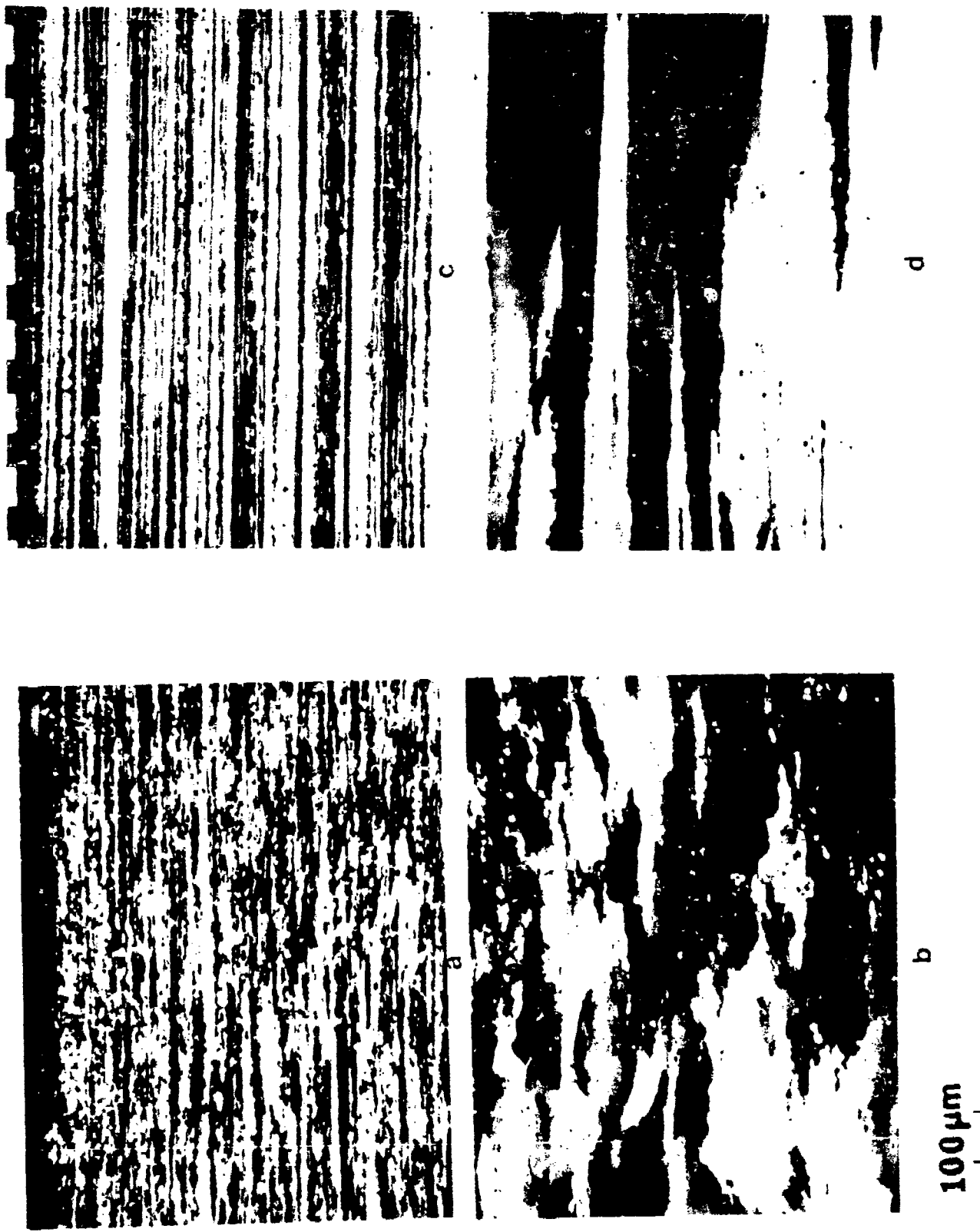(S# 498812)

100μm

Figure 34. The microstructure of 7050 extruded under conditions of low Z and high R;
(a) transverse section at surface, (b) transverse section at center, (c)
longitudinal section at surface, and (d) longitudinal section at center.
(S# 498820)

Figure 35. The microstructure of 7475 extruded under conditions of low Z and high R; (a) transverse section at surface, (b) transverse section at center, (c) longitudinal section at surface, and (d) longitudinal section at center.

100 μm

Figure 36. The microstructure of 7475 extruded under conditions of low Z and high R: (a) transverse section at surface, (b) transverse section at center, (c) longitudinal section at surface, and (d) longitudinal section at center. (SX 69862)
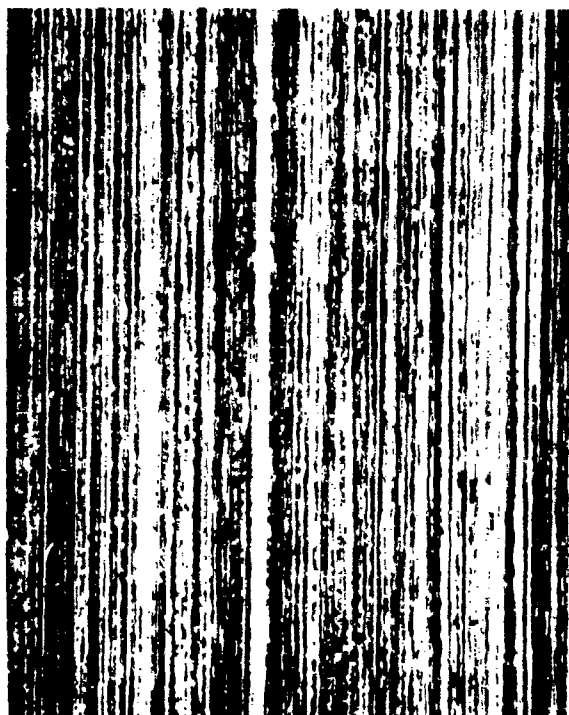
100μm

Figure 37. The microstructure of 7050 extruded under conditions of low Z and low R; (a) transverse section at surface, (b) transverse section at center, (c) longitudinal section at surface, and (d) longitudinal section at center. (S# 498824)

100 μm

100μm

Figure 38. The microstructure of 7475 extruded under conditions of low Z and low R; (a) transverse section at surface, (b) transverse section at center, (c) longitudinal section at surface, and (d) longitudinal section at center.

Figure 39. The microstructure of 7475 extruded under conditions of low Z and low R; (a) transverse section at surface, (b) transverse section at center, (c) longitudinal section at surface, and (d) longitudinal section at center. (S# 498826)

100μm

SURFACE

2mm
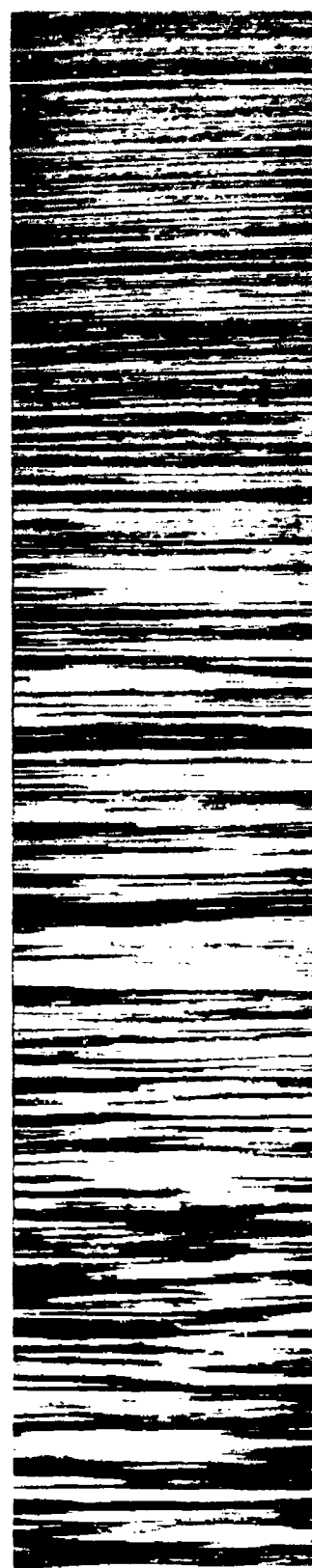
a   b

Figure 40. Longitudinal sections of (a) 7050 and (b) 7475 showing variation in grain morphology from surface to center in the low Z, low R extrusions.

S

$\frac{T}{4}$

$\frac{T}{2}$

50 μm

LOW R   **HIGH R**

Figure 41.   As-polished sections taken at surface, T/4 and T/2
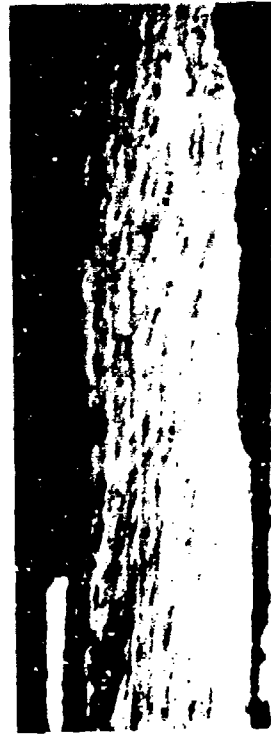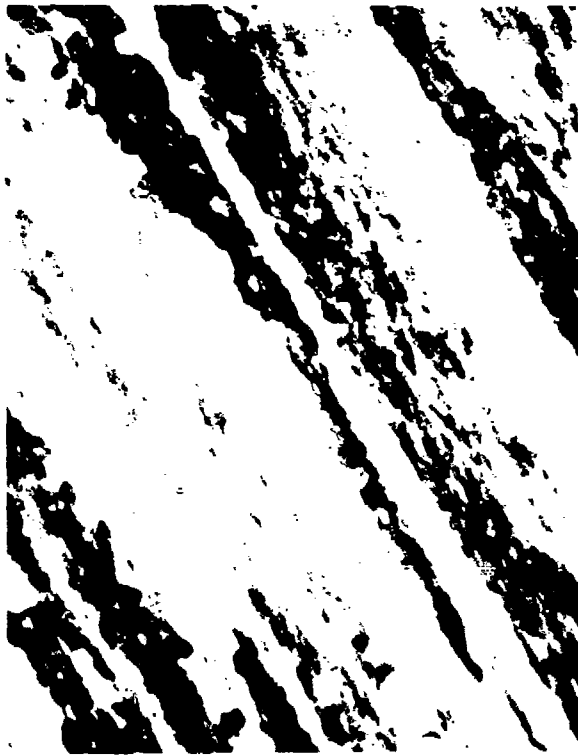in the low and high R extrusions of 7050.

LOW R

a

HIGH R

b

20 µm

Figure 42. Distribution of insoluble phases at the T/2 location in 7050 extruded at (a) low R, and (b) high R.

Figure 43. Optical micrographs taken at three orientations of polarization of 7050 (high Z, high R). Substructure is absent in the recrystallized grain regardless of orientation.

20 μm

Figure 44. Optical micrographs of 7475 (high Z, low R) illustrating preferred orientation of substructure with an unrecrystallized grain. Three different orientations of polarization are present.

20 µm

10 μm

Figure 45. Optical micrographs of 7050 (high Z, high R) illustrating preferred orientation of substructure within an unrecrystallized grain.
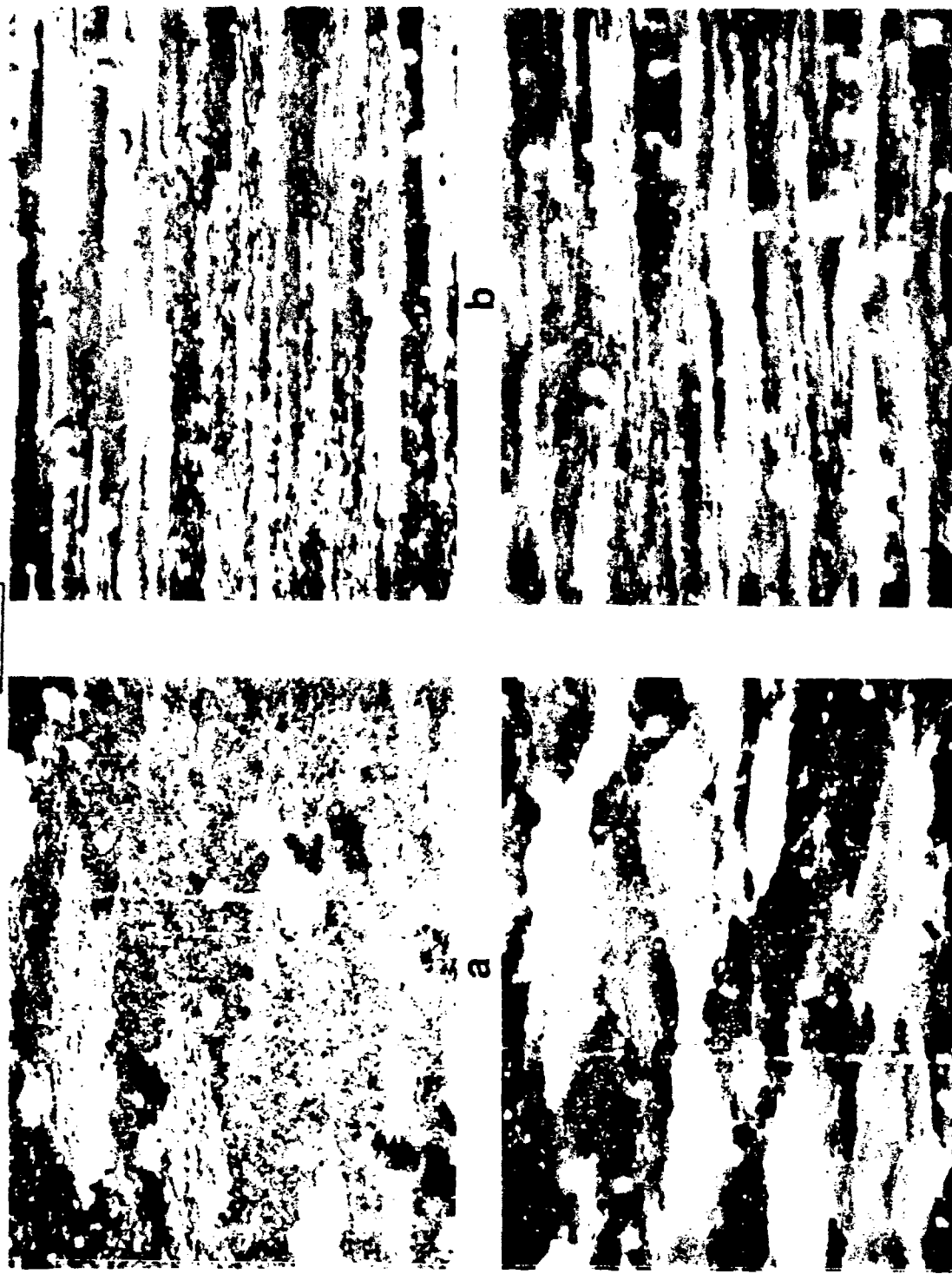
Figure 46. Polarized light micrographs taken at mid-plane of (a) high Z, low R, (b) high Z, high R, (c) low Z, low R, and (d) low Z, high R W-temper 7050 extrusions. (Longitudinal section).
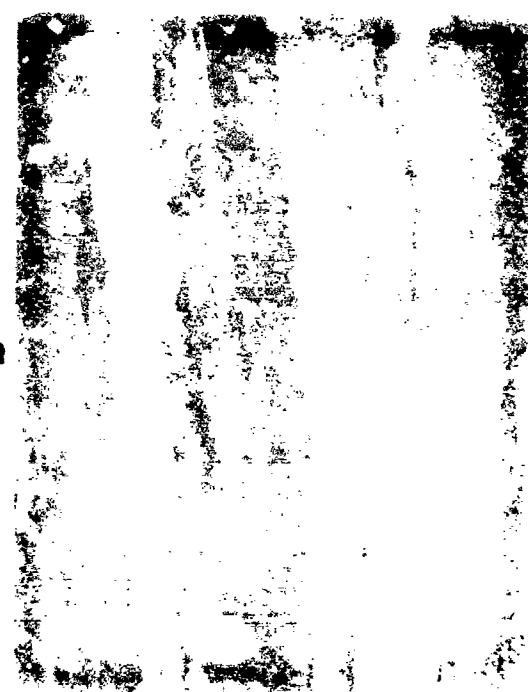
Figure 47. Polarized light micrographs at sightly higher magnifications than Figure 46; (a) high Z, low R, (b) high Z, high R, (c) low Z, low R, and (d) low Z, high R. (Longitudinal section).

20 μm

RECRYSTALLIZED

RECOVERED

RECOVERED

RECOVERED

RECRYSTALLIZED

2μm

Figure 48.   Regions in W temper 7050 which contained recovered
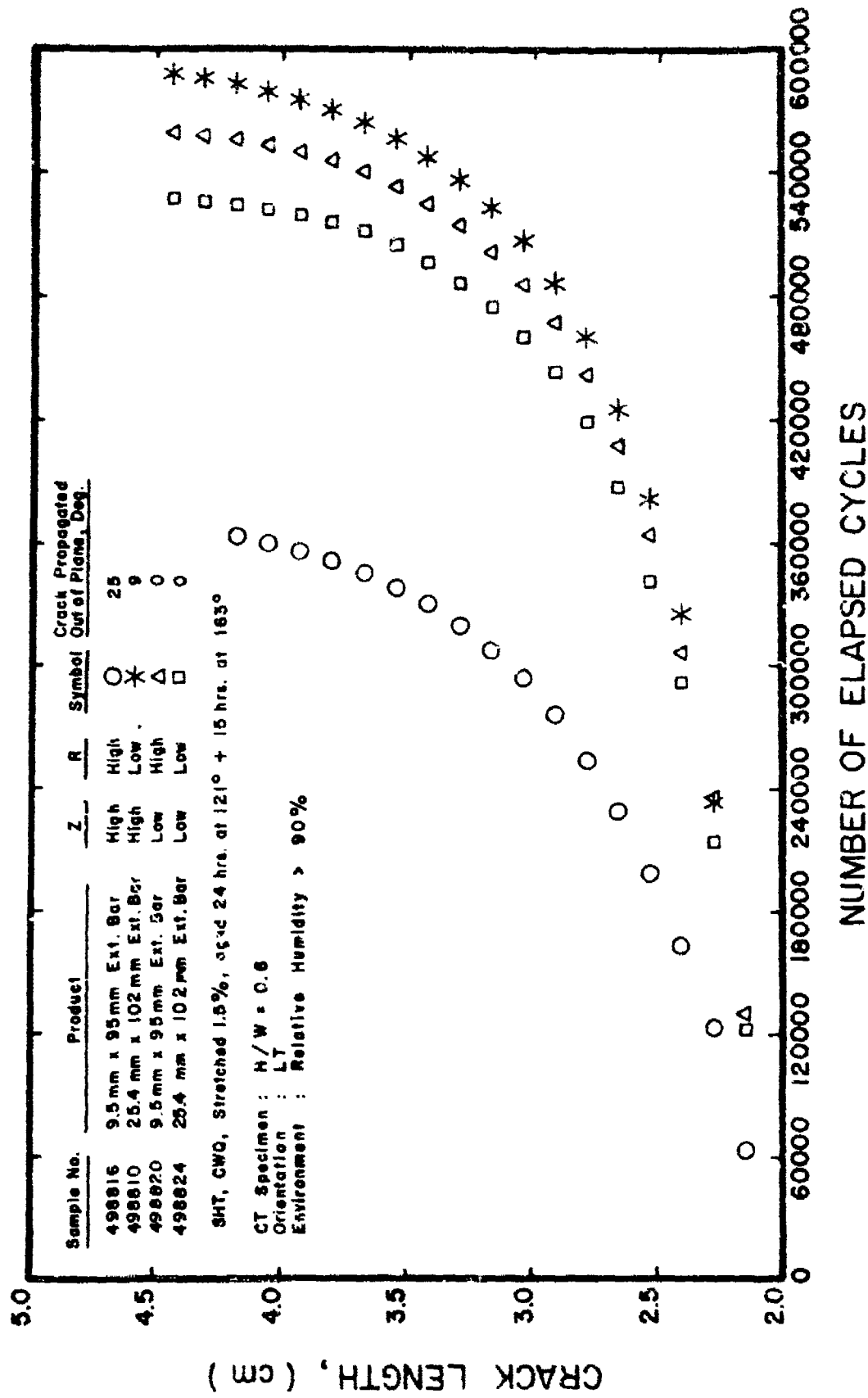   subgrains and recrystallized grains.

Sample No.	Product	Z	R	Symbol	Crack Propagated Out of Plane, Deg.
498816	9.5 mm x 95 mm Ext. Bar	High	High	O	25
498810	25.4 mm x 102 mm Ext. Bar	High	Low	*	9
498820	9.5 mm x 95 mm Ext. Bar	Low	High	△	0
498824	25.4 mm x 102 mm Ext. Bar	Low	Low	□	0

SHT, CWQ, Stretched 1.5%, aged 24 hrs. at 121° + 15 hrs. at 163°

CT Specimen : H/W = 0.6
Orientation : LT
Environment : Relative Humidity > 90%

CRACK LENGTH, (cm)

NUMBER OF ELAPSED CYCLES

Figure 49. Crack length versus number of elapsed cycles, 7050-T7651.

Sample No.	Product	Z	R	Symbol	Crack Propagated Out of Plane, Deg.
498813	9.5mm x 95mm Ext. Bar	High	High	○	24
498814	9.5mm x 95mm Ext. Bar	High	High	*	12
498811	25.4 mm x 102mm Ext. Bar	High	Low	xx	19
498812	25.4 mm x 102mm Ext. Bar	High	Low	△	0
498821	9.5 mm x 95mm Ext. Bar	Low	High	◻	8
498822	9.5 mm x 95mm Ext. Bar	Low	High	●	0
498825	25.4 mm x 102 mm Ext. Bar	Low	Low	✿	0
498826	25.4 mm x 102 mm Ext. Bar	Low	Low	▷	0

SHT, CWQ, Stretched 1.5%, aged 24 hrs. at 121° + 15 hrs. at 163°

CT Specimen : H/W = 0.6
Orientation : LT
Environment : Relative Humidity < 90%

CRACK LENGTH, (cm)

NUMBER OF ELAPSED CYCLES

Figure 50. Crack length versus number of elapsed cycles, 7475-T7651.
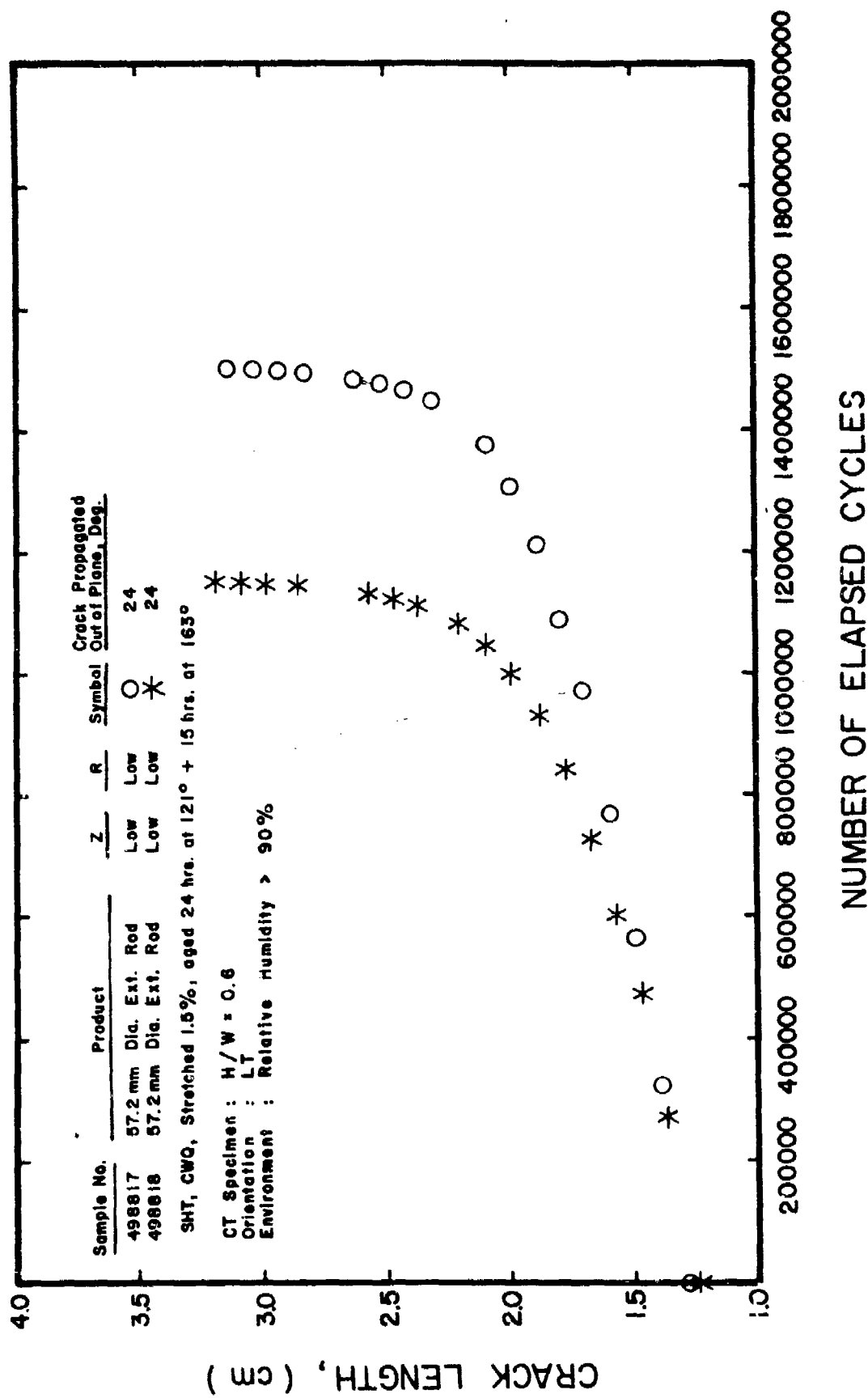
Figure 51. Crack length versus number of elapsed cycles, 7475-T7651 round rod extrusions.
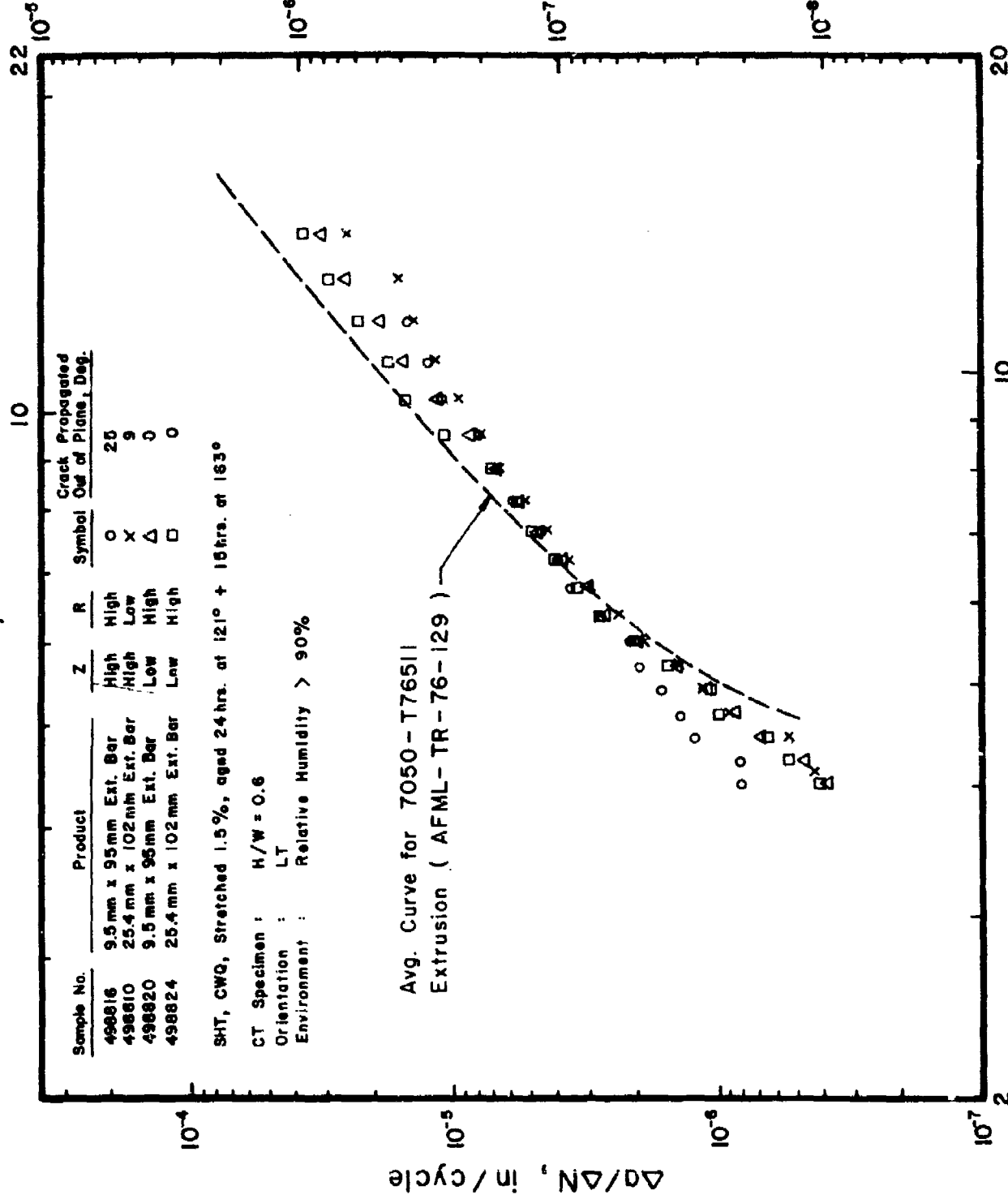
Figure 52. Cyclic stress intensity factor range, ΔK, versus cyclic fatigue crack growth, da/dn, 7050-T7651.
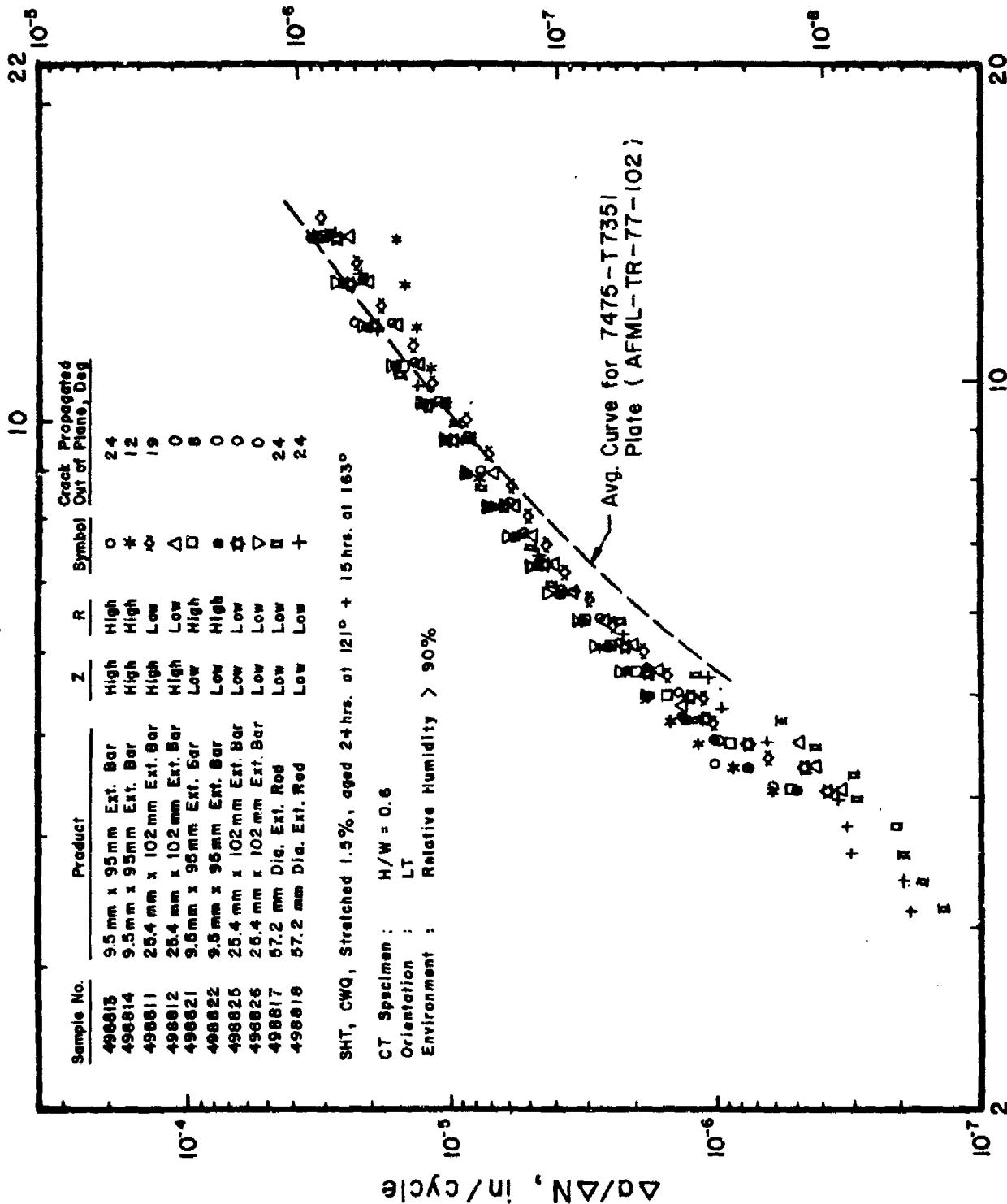
Figure 53. Cyclic stress intensity factor range, ΔK, versus cyclic fatigue crack growth, da/dn, 7475-T7651.
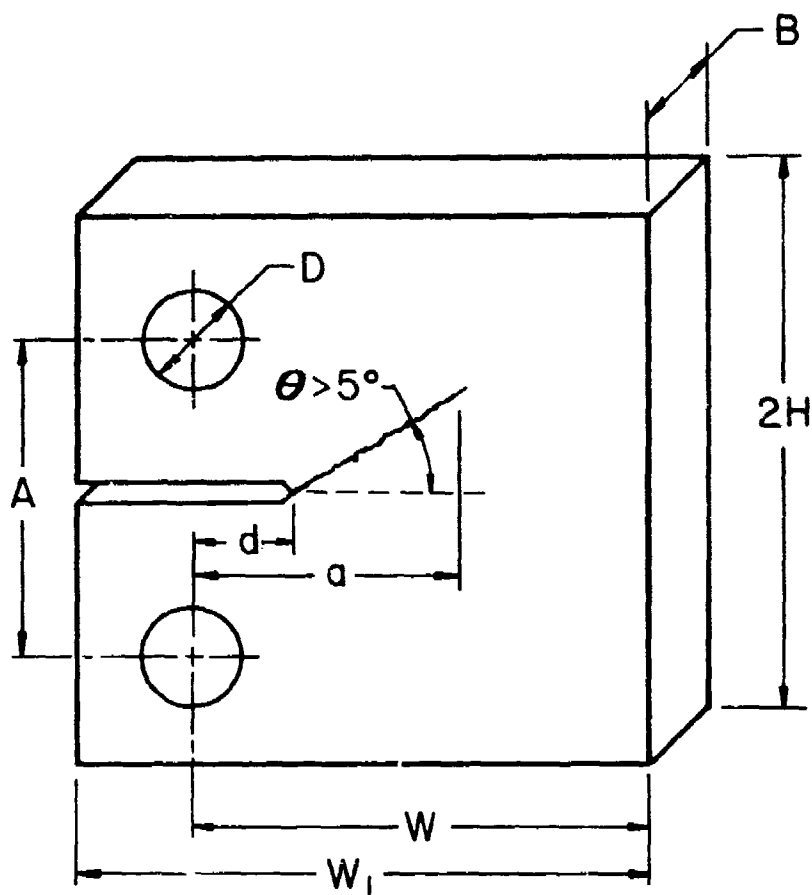
a = crack length

Violates E647-78T

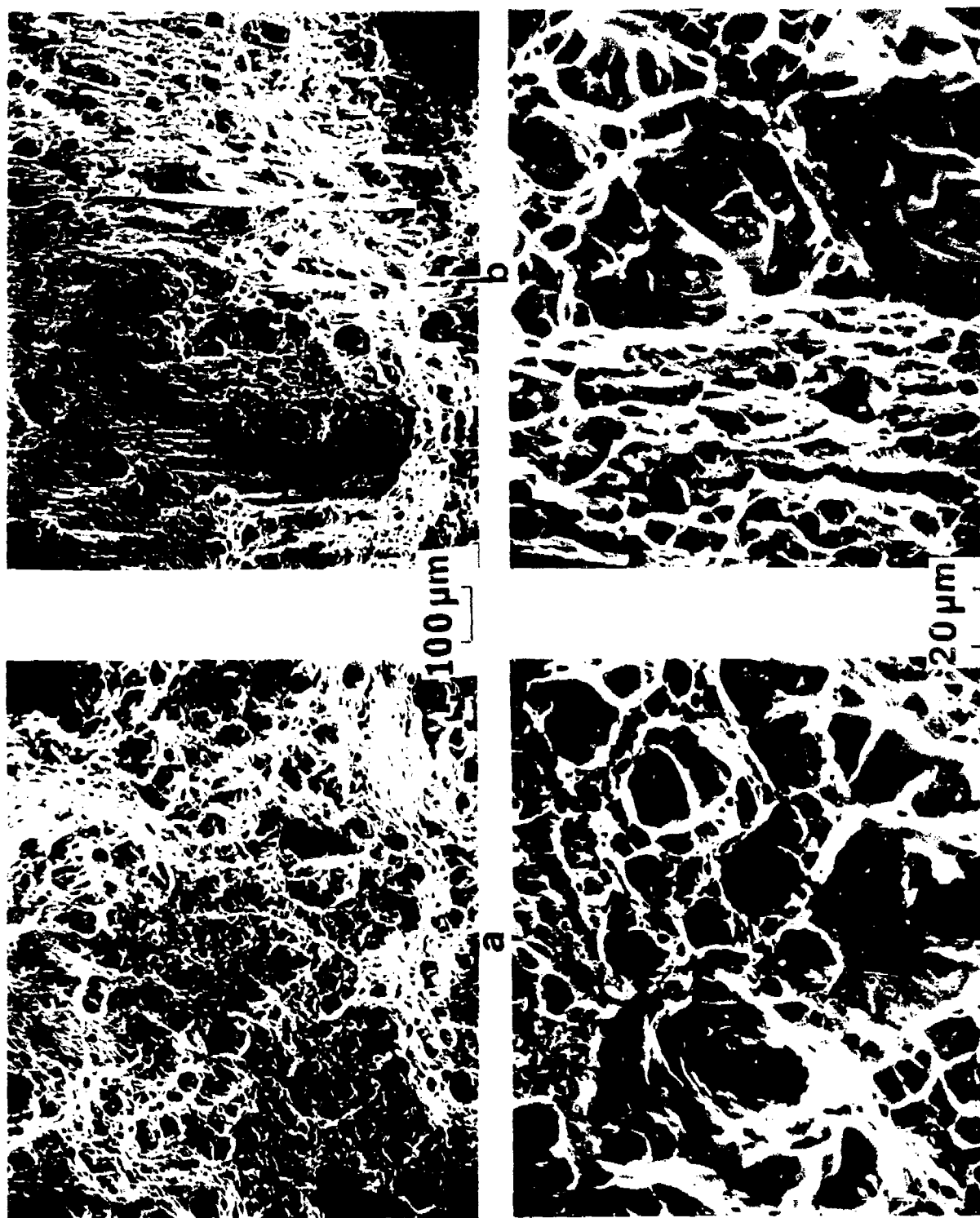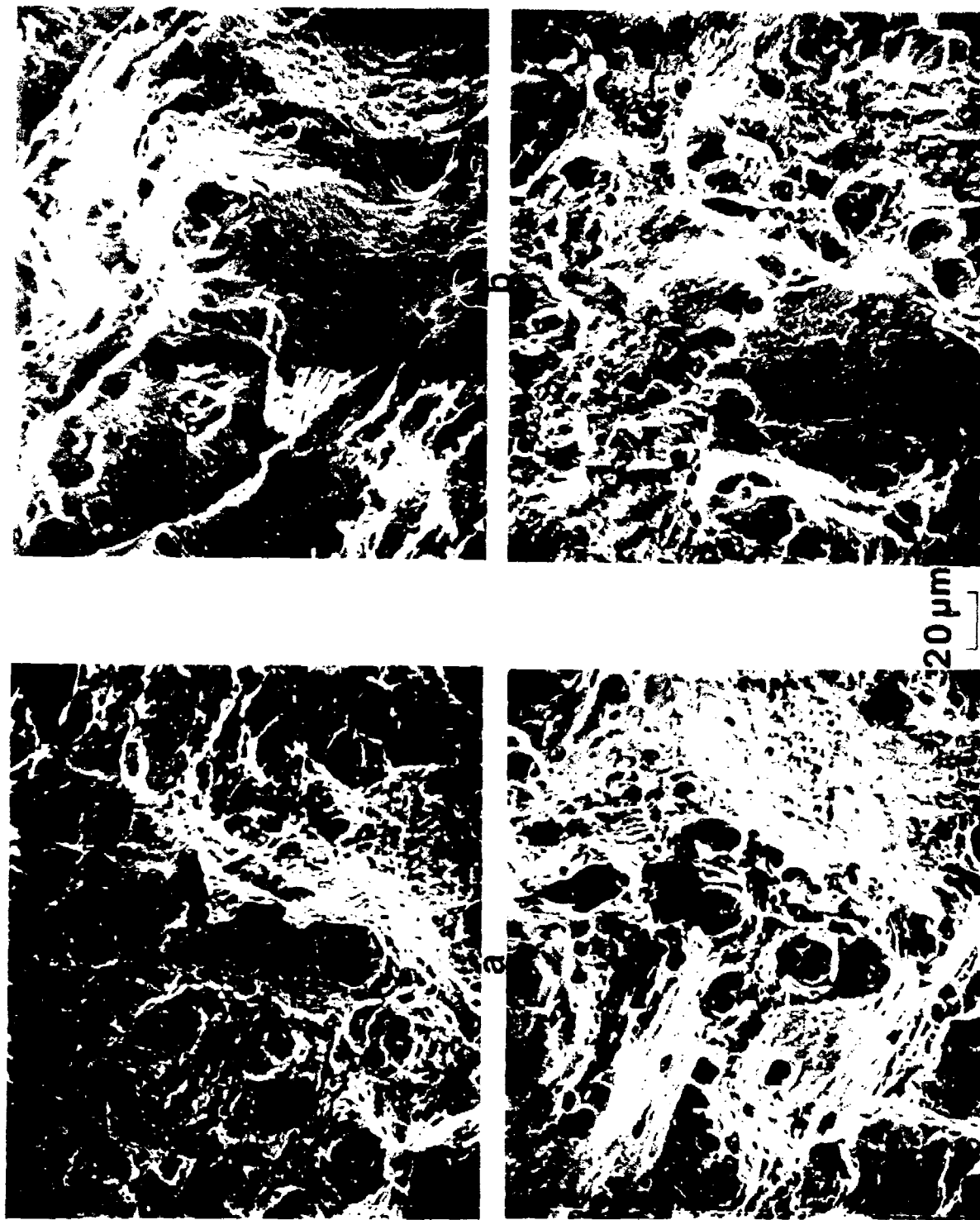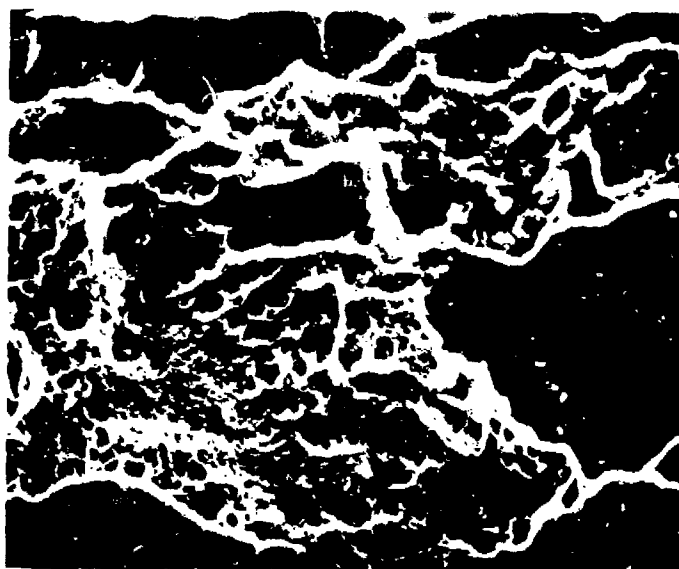Figure 54.   Definition of crack deviation according to ASTM
E647-78T.

Figure 55. Longitudinal tensile failures of 7050; (a) high Z, high R and (b) low Z, high R.

Figure 56. Longitudinal tensile failures of 7475; (a) high Z, high R, (b) high Z, low R, (c) low Z, high R, and (d) low Z, low R.
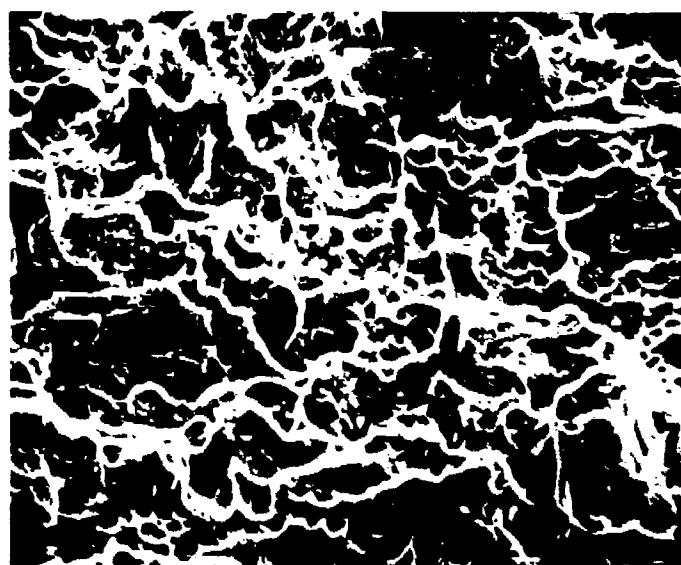
a

b

20 μm

Figure 57. (a) TL and, (b) LT Kahn tear fractures from 7050
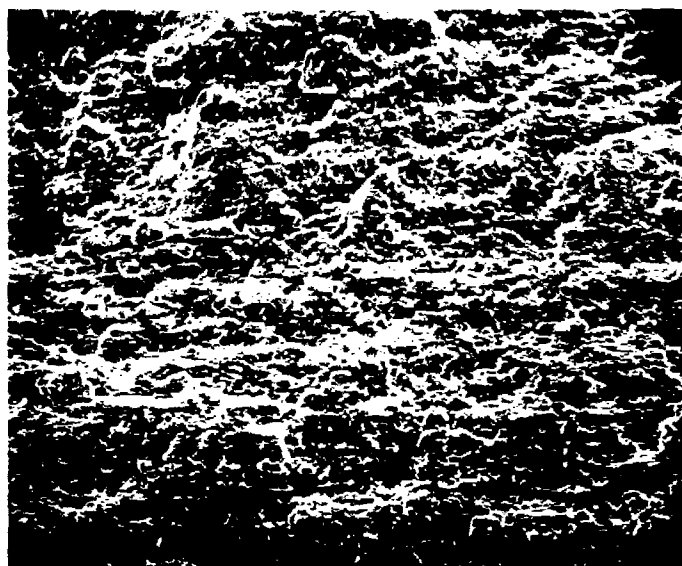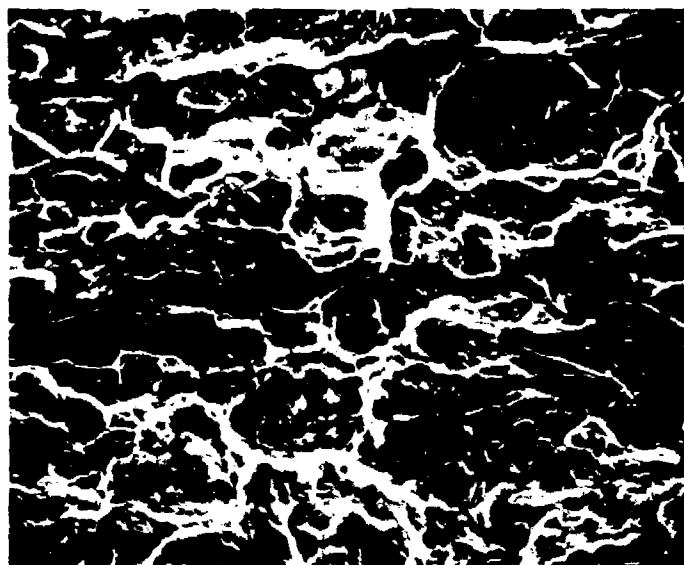extruded at low Z, low R.
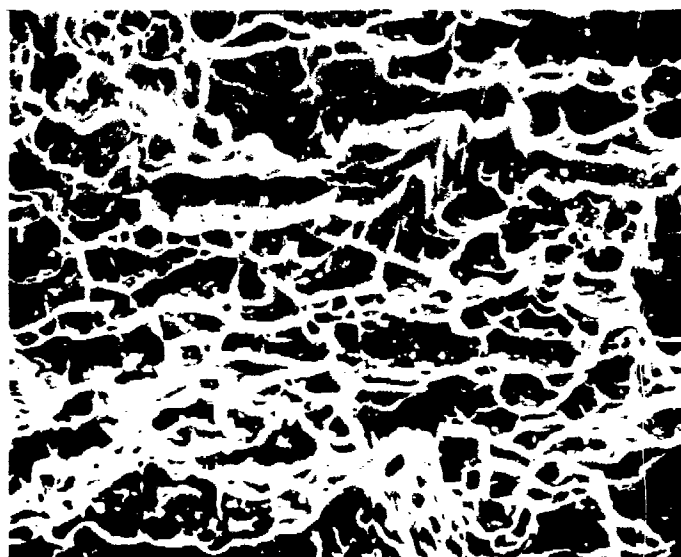
20 μm

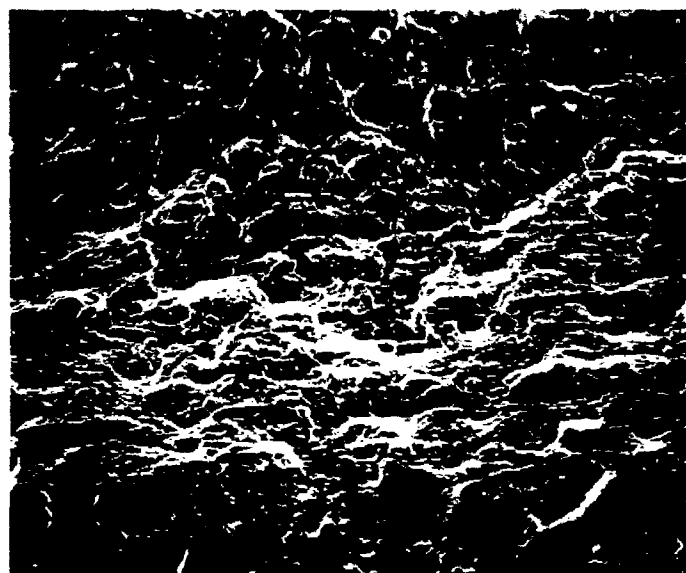Figure 58. (a) TL and (b) LT Kahn tear fractures of 7050 extruded at low Z, high R.

100 μm

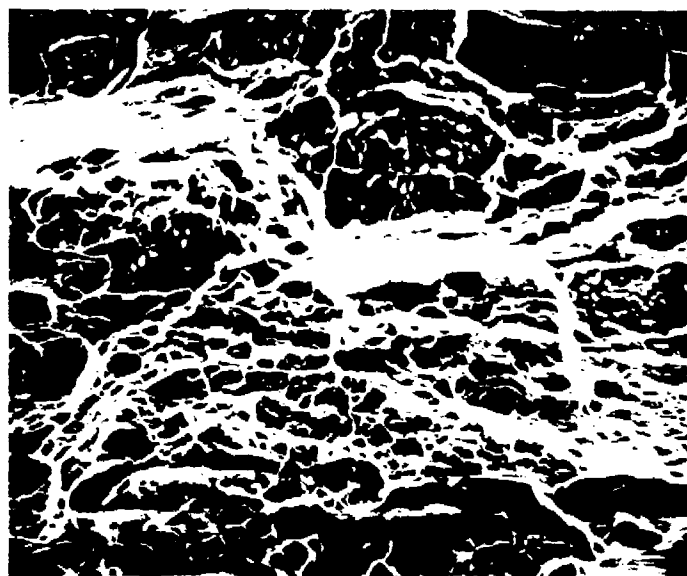**20 μm**

Figure 59. TL Kahn tear fracture of 7050 extruded at high Z, high R.

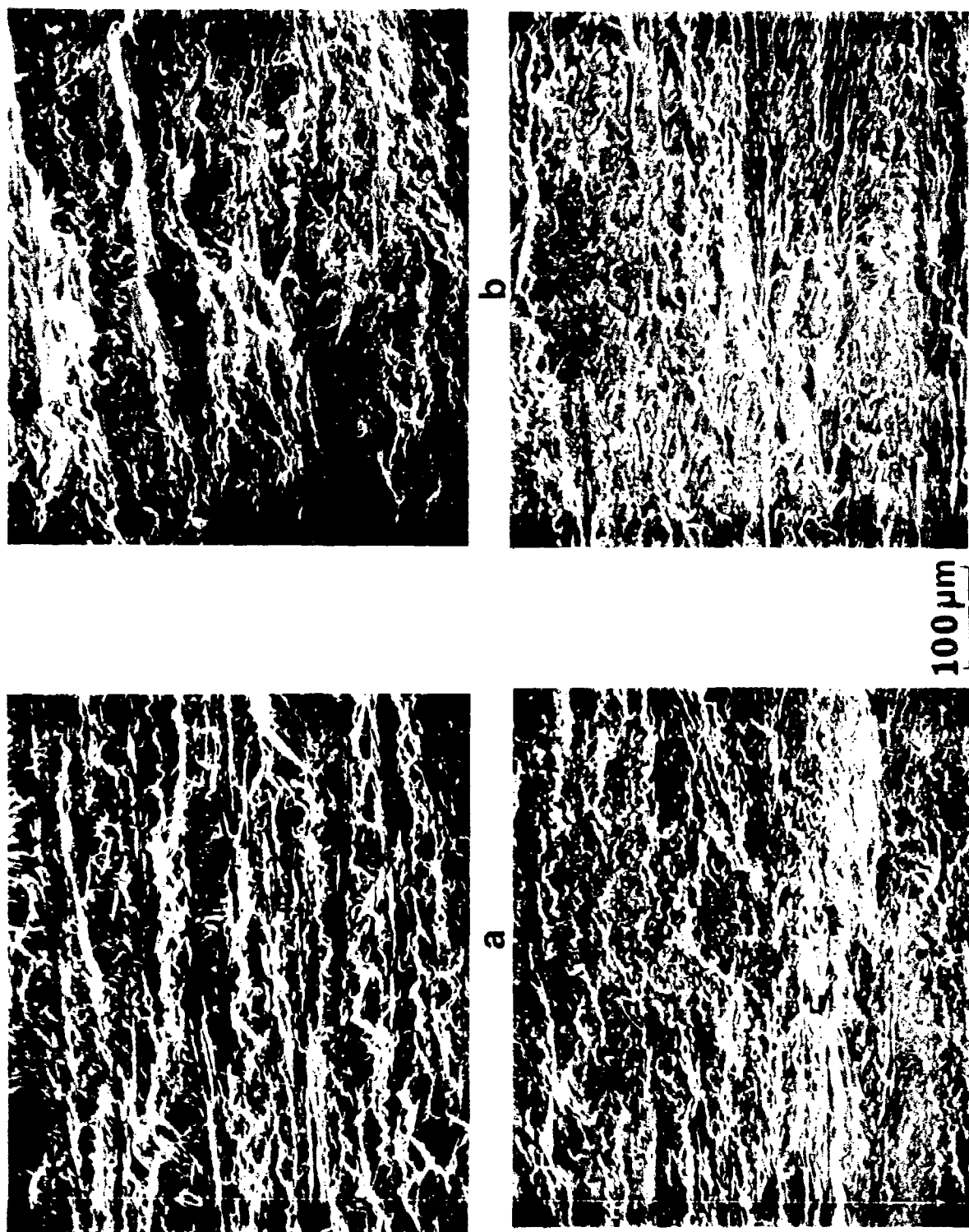Figure 60. TL Kahn tear fracture of 7050 extruded at high Z, low R.

Figure 61. Fracture surfaces at a ΔK of approximately (a) 5, (b) 6.5, (c) 8, and (d) 10 MPa√m of 7050 extruded at high Z, high R.
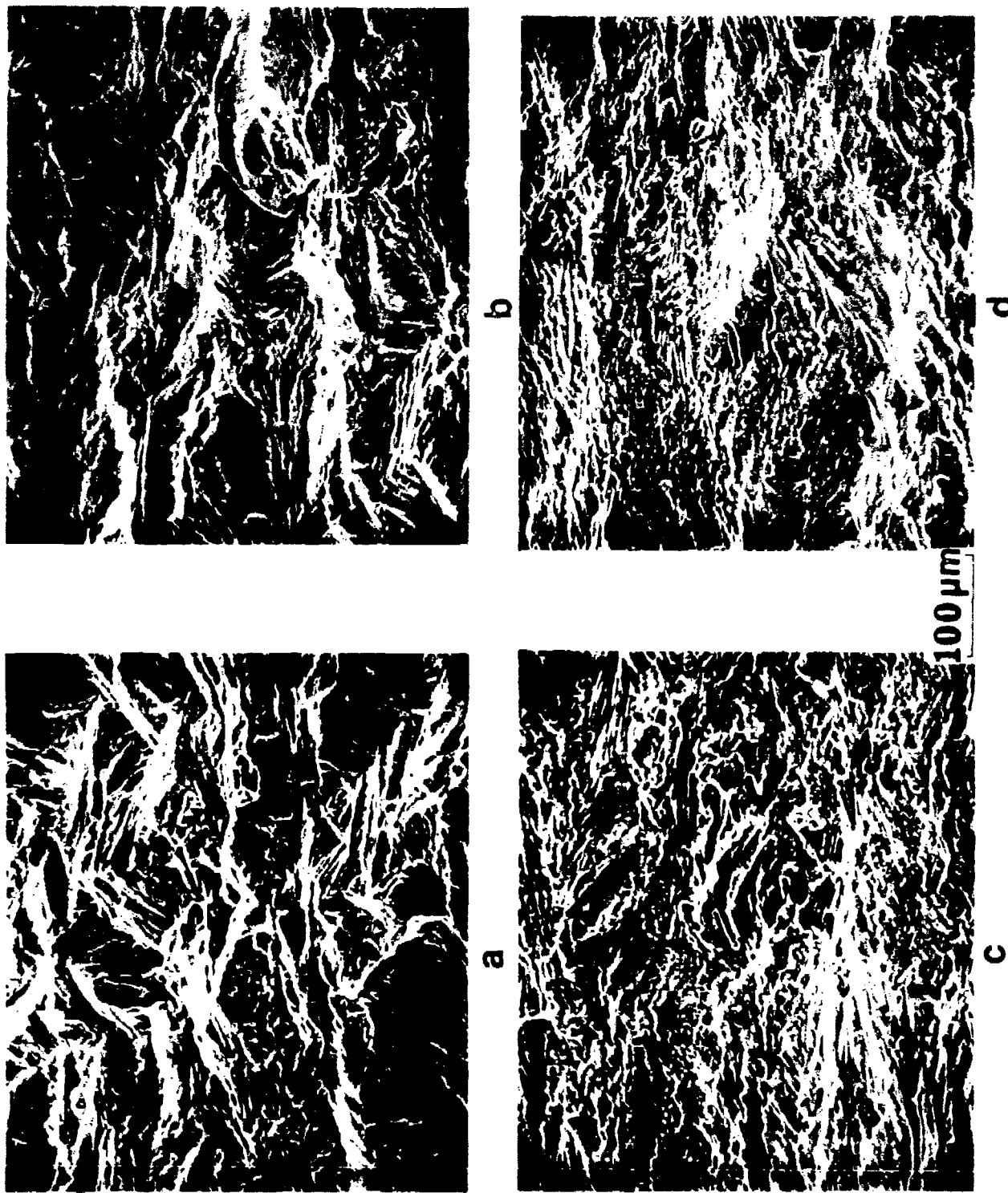
Figure 62. Fracture surfaces at a ΔK of approximately (a) 5, (b) 6.5, (c) 8, and (d) 10 MPa$\sqrt{m}$ of 7050 extruded at high Z, low R.

Figure 63. Fracture surfaces at a ΔK of approximately (a) 5, (b) 6.5, (c) 8, and (d) 10 MPa√m of 7050 extruded at low Z, high R.

Figure 64. Fracture surfaces at a ΔK of approximately (a) 5, (b) 6.5, (c) 8, and (d) 10 MPa$\sqrt{m}$ of 7050 extruded at low Z, low R.
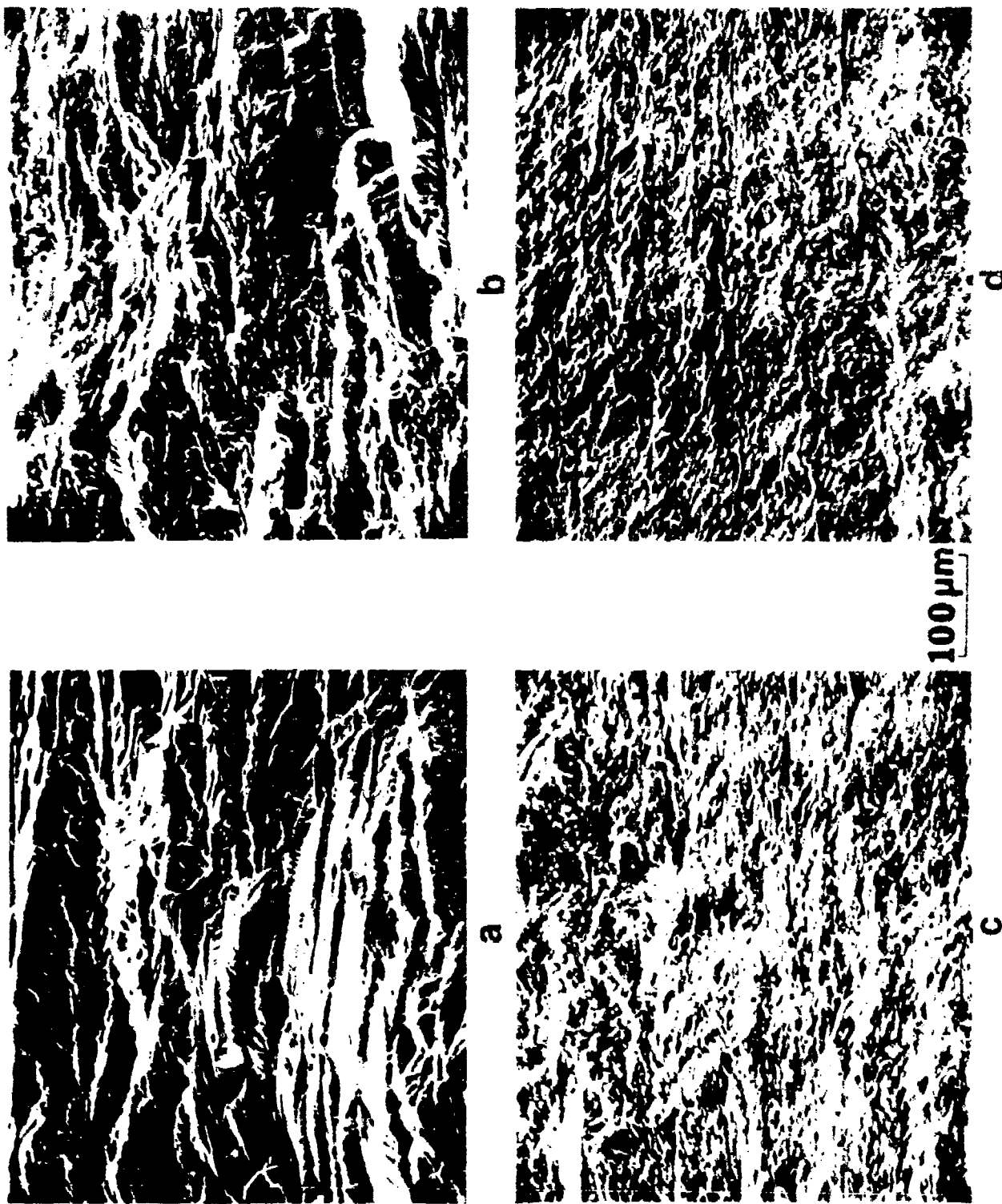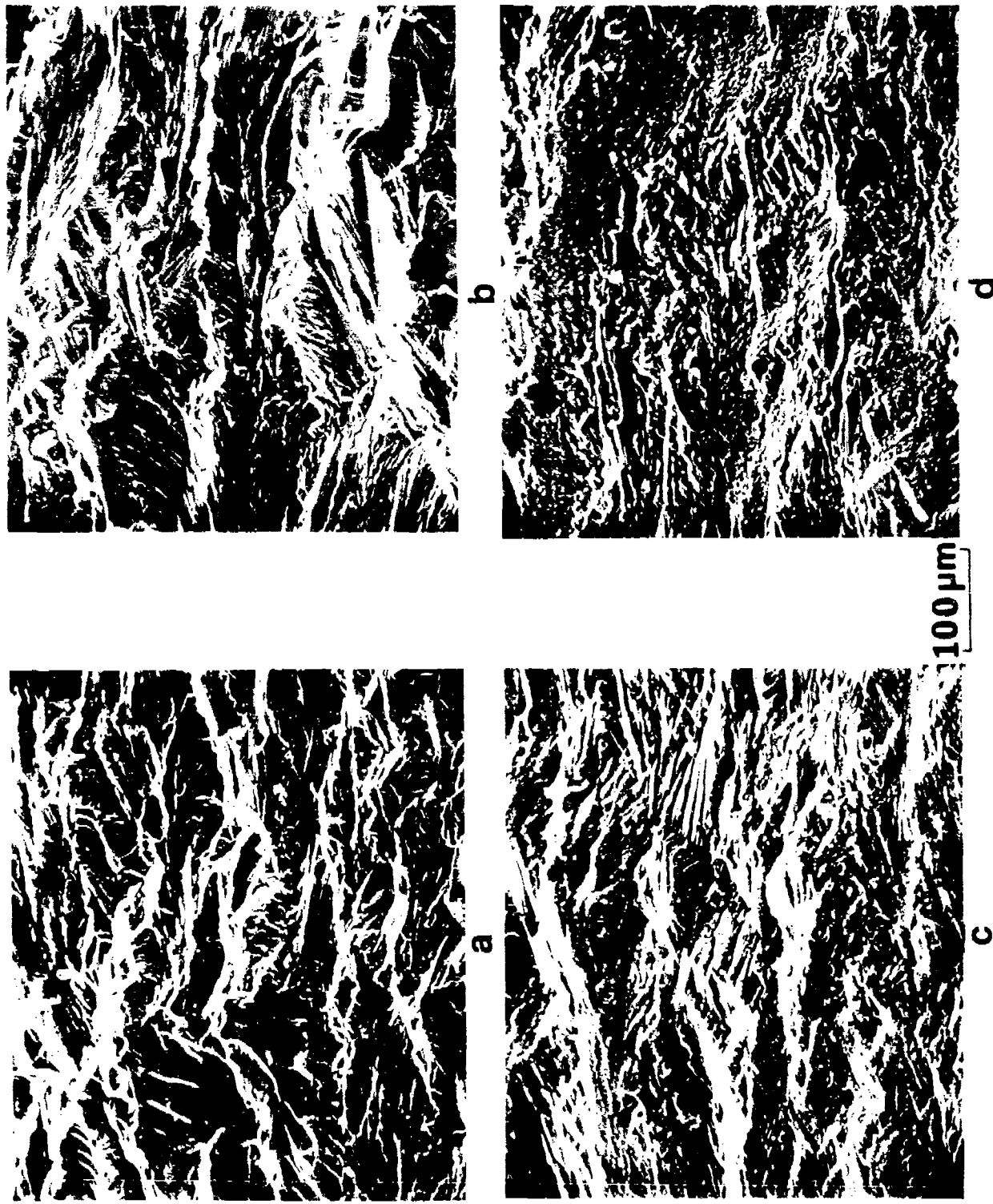
Figure 65.   Fractographs from the high Z, high R 7050 extrusion in the transition region from crack growth to overload.   The direction of crack growth is given on the figure.

100 μm

CG →

20 μm

Figure 66. Fractographs from the high Z, low R 7050 extrusion in the transition region from crack growth to overload. The direction of crack growth is given on the figure.

100 μm

CG →

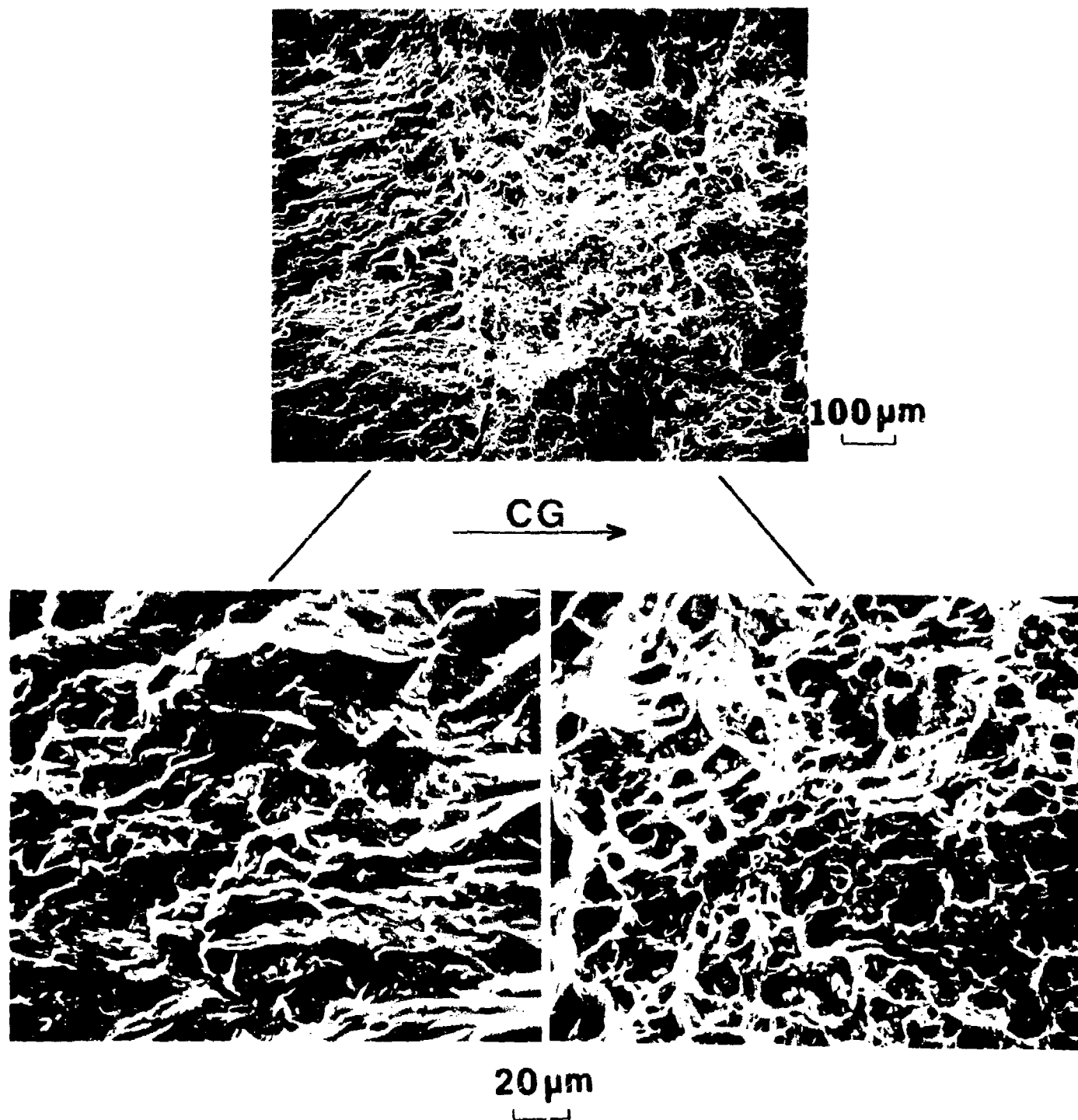**20 μm**

Figure 67.   Fractographs from the low Z, high R 7050 extrusion
in the transition region from crack growth to over-
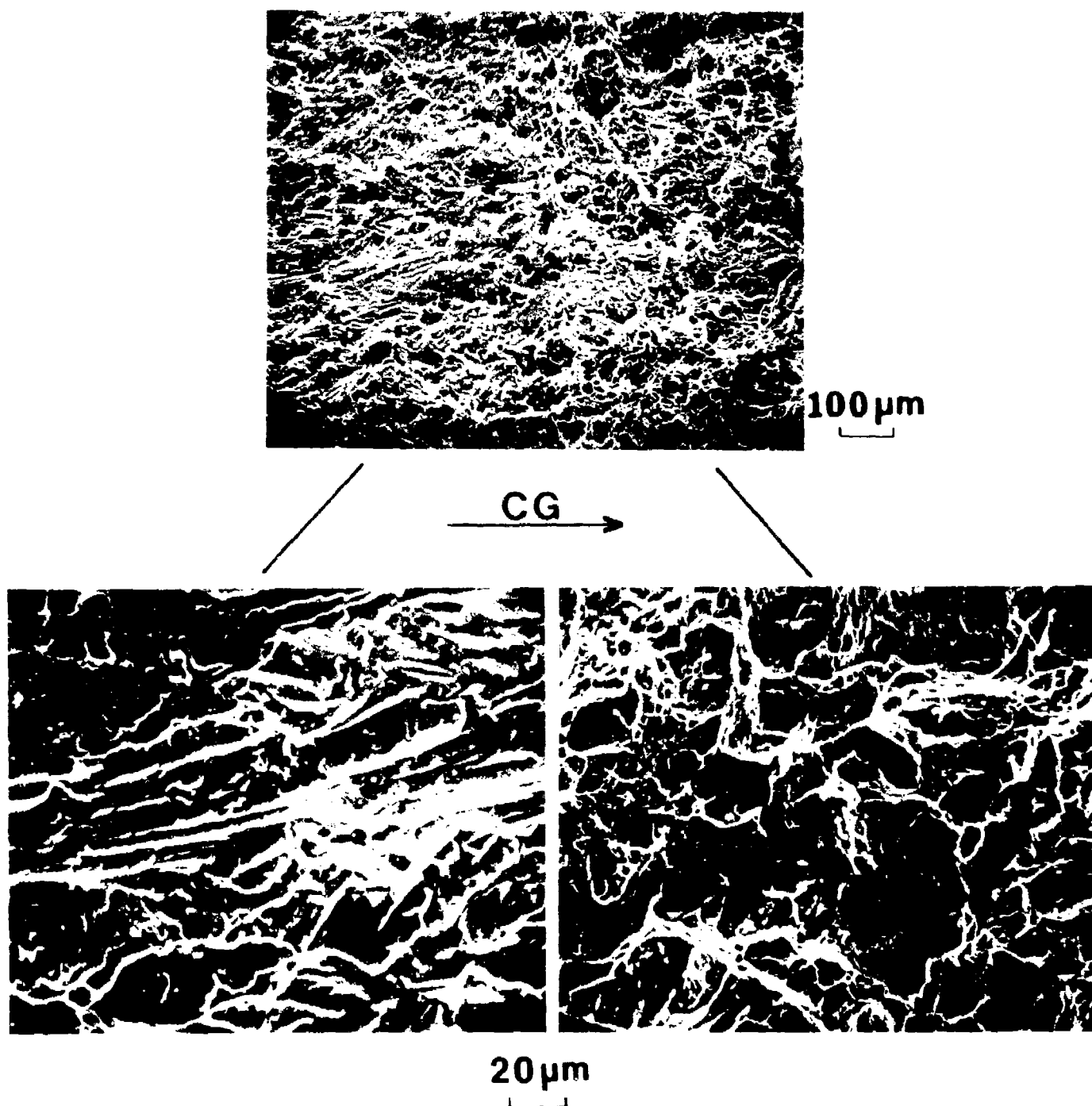load.   The direction of crack growth is given on the
figure.
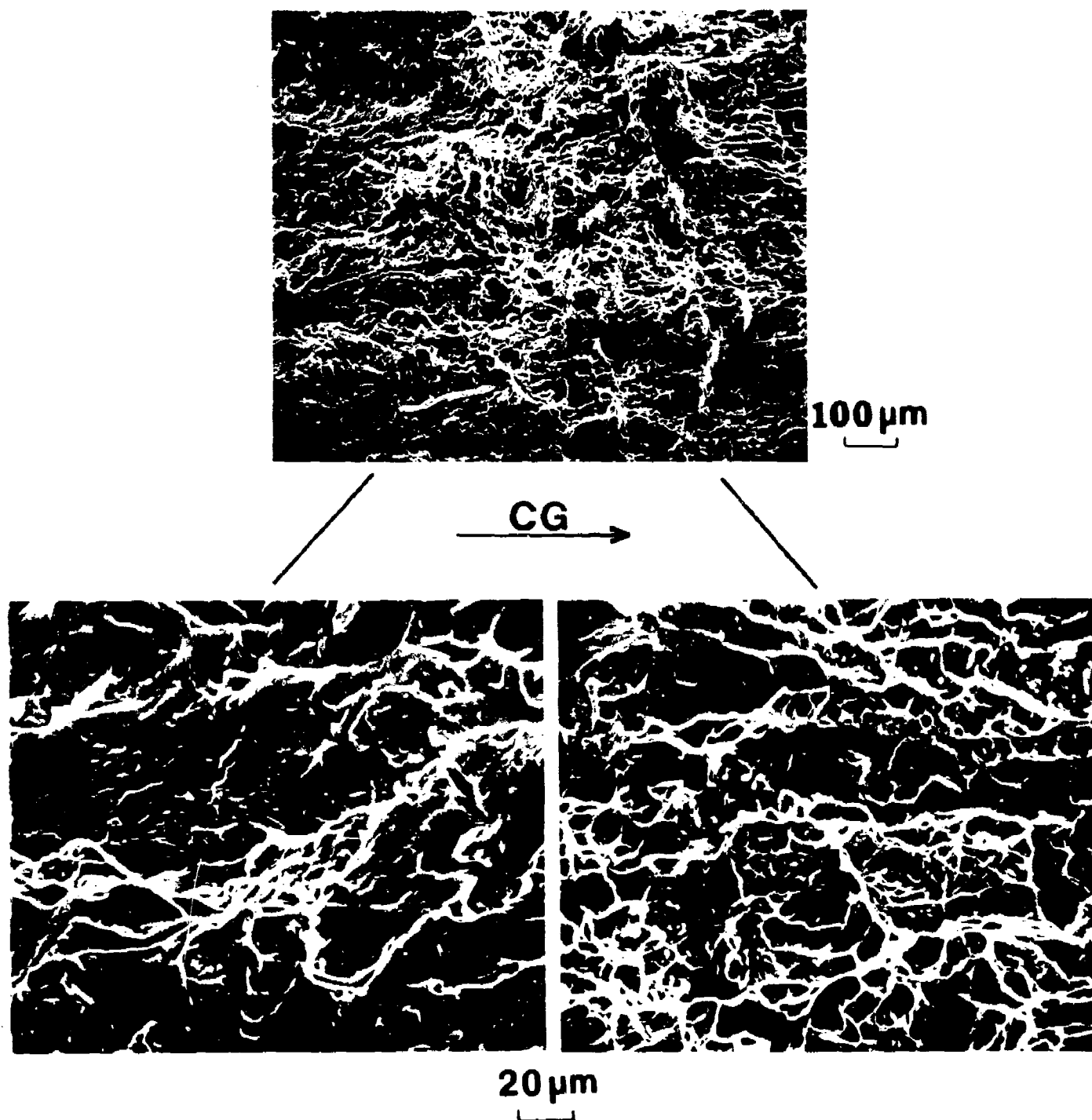
Figure 68. Fractographs from the low Z, low R 7050 extrusion in the transition region from crack growth to over-load. The direction of crack growth is given on the figure.
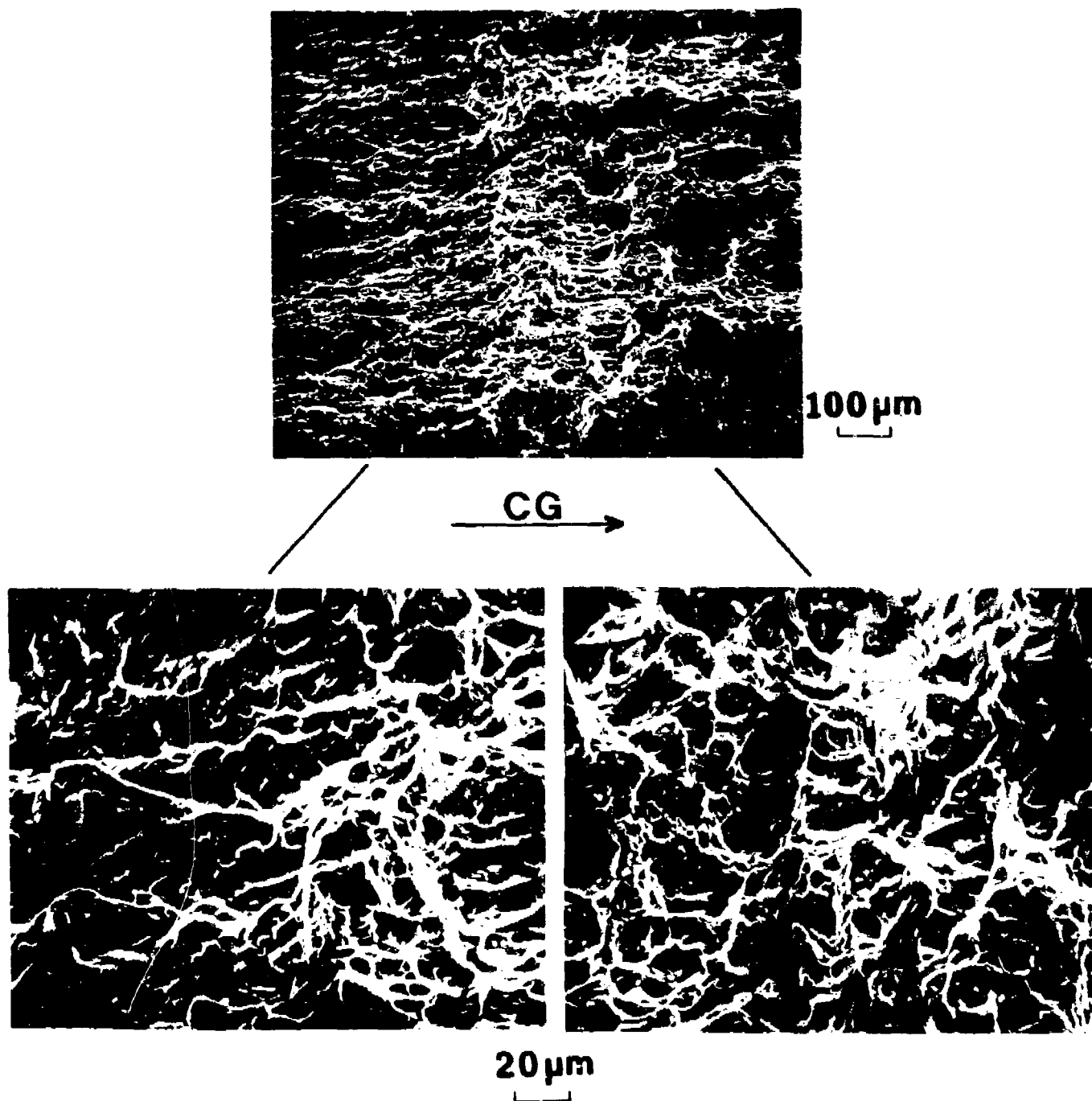
Figure 69. Effect of Extrusion Aspect Ratio on Yield Strength of
Alloy 1.2 (Al-3Li-2Cu-0.2Zr), Peak Aged Condition.[15]

Figure 70.   Effect of Extrusion Aspect Ratio on Tensile
             Properties of Alloy 1.2 (Al-3Li-2Cu-0.2Zr), Peak
             Aged Condition.(13)

Figure 71. Schematic Illustrating the Effect of Composition on Solvus Temperature.

APPENDIX A

SELECTION OF EXPERIMENTAL EXTRUSION CONDITIONS

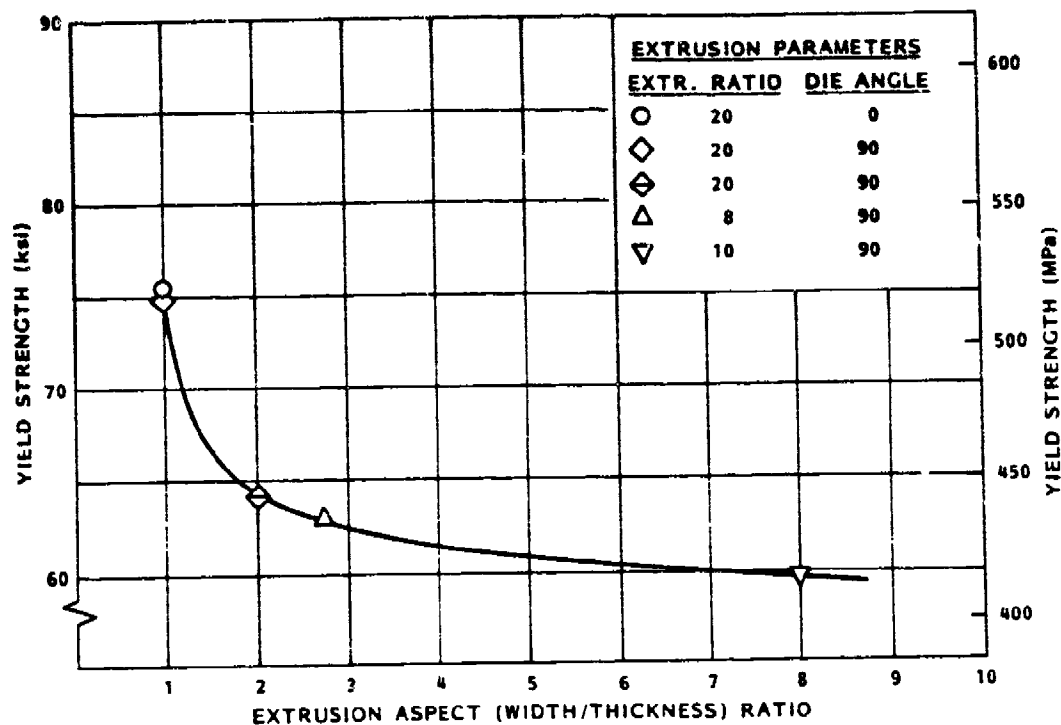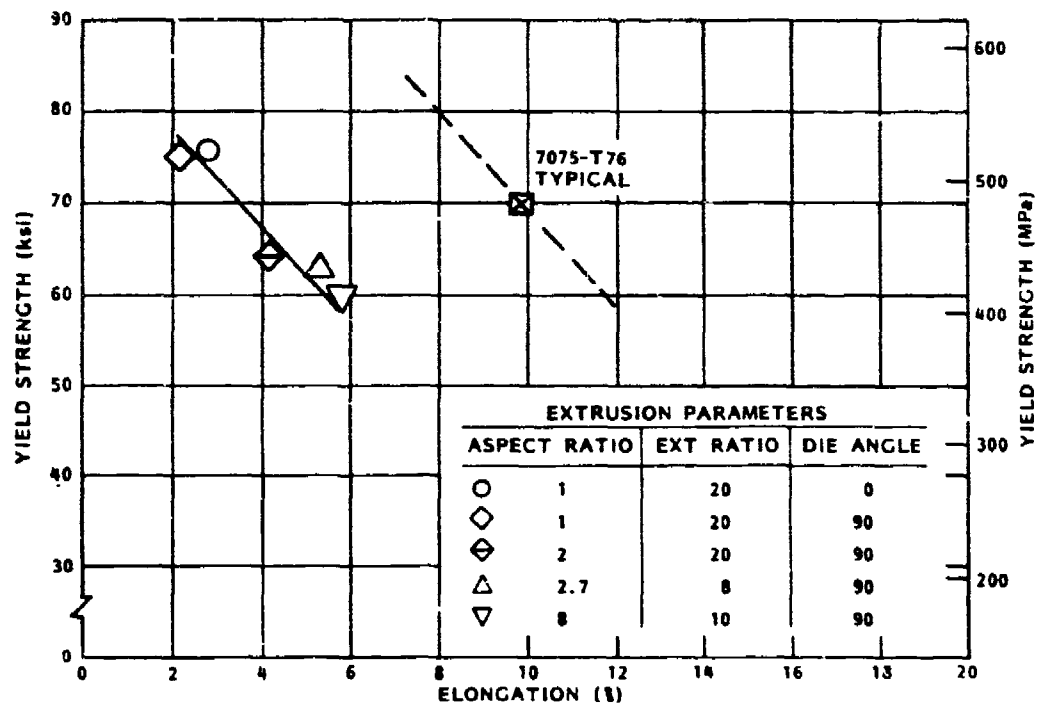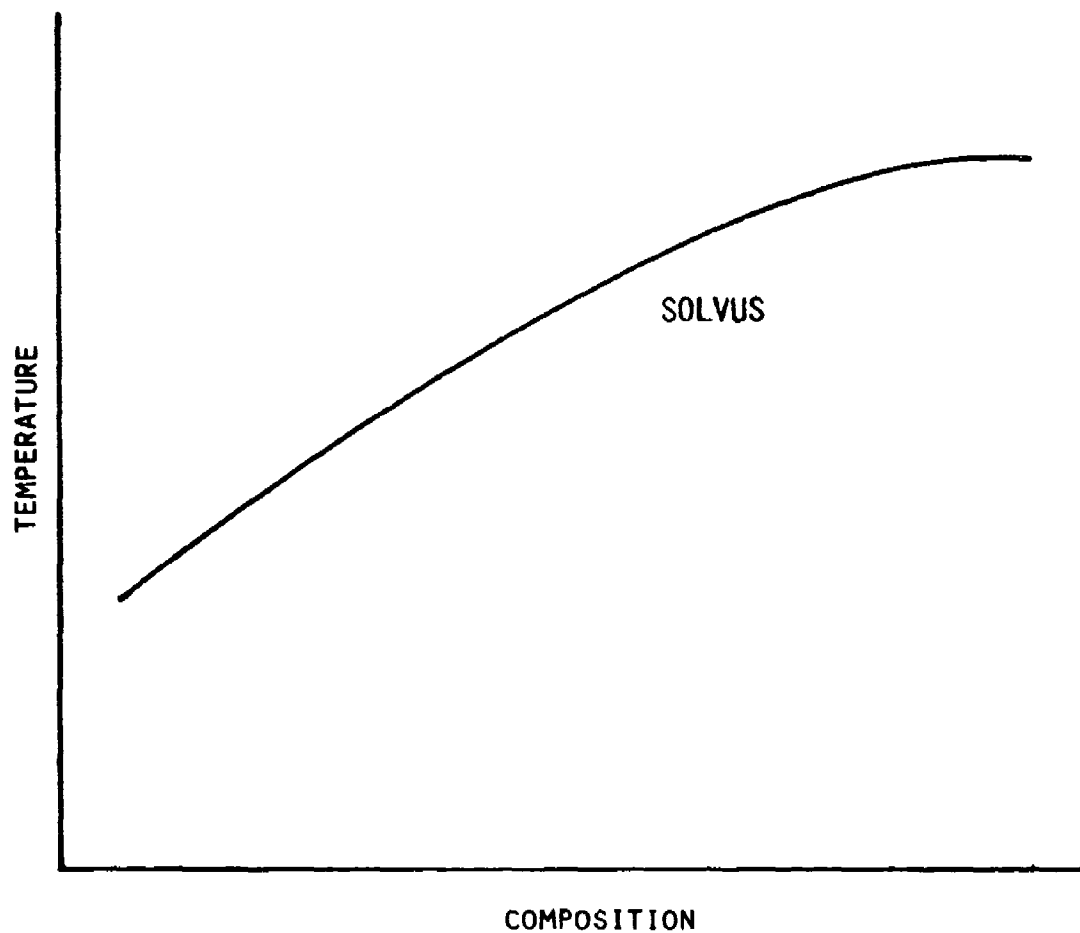Although the primary aim of the investigation was to explore the control of mcirostructure through variations in the temperature compensated strain rate, Z, it seemed advisable to organize the tests so that the final results could be evaluated by more traditional means, i.e., in terms of the extrusion and aspect ratios. Accordingly, an experimental design of the following form was chosen:

HIGH Z, HIGH R	HIGH Z, LOW R
LOW Z, HIGH R	LOW Z, LOW R

The first step in designing the experiment was to select extrusion and aspect ratios which would be reasonably representative of those used for commercial production of 7XXX extrusions on a 22.5-MN press. The choices were:

Section Type	Section Size (mm) Width (W)	Thickness (T)	Diameter (D_E)	Extrusion Ratio (R)	Aspect Ratio (W/T)
Rectangular Bar	96.2	8.0	--	26.75	12
Rectangular Bar	102.6	25.6	--	7.82	4
Round Rod	--	--	57.2	8.01	--

The round rod was included because many past investigations of microstructure development have employed axisymmetric conditions.

The next step was to select strain rates and temperatures to produce as broad a variation as possible in the Z parameter and, therefore, in the microstructure. The strain rate ($\dot{\epsilon}$) and temperature (T) which determine Z through the relation

$$Z = \dot{\epsilon} \, \exp(\Delta H / RT)$$

must, of course, be within the speed and force capabilities of the extrusion press. Based on prior experience, achievable extremes of $\dot{\epsilon}$ and T (where T is taken as the initial billet temperature) are:

$\dot{\epsilon}$ (1/sec)	T (°C)	Z (1/sec)	
.40 max	288 min	3.4E13	(High Z)
.05 min	427 max	7.4E09	(Low Z)

The Z variation based on the chosen $\dot{\epsilon}$'s and T's is seen to be about four orders of magnitude. The literature would suggest that such variation is ample to effect changes in microstructure. An activation energy close to that of self diffusion in aluminum, 150,000 Joules/Gram mole, was used to estimate the Z parameter.

The last step in the design was to determine press ram velocities consistent with the chosen strain rates. For this, Feltham's definition of mean strain rate for axisymmetric extrusion was used:

$$\bar{\dot{\epsilon}} = V \cdot \frac{6D_C \, (\ln R) \tan\alpha}{(D_C^3 - D_E^3)},$$

where: $\bar{\dot{\epsilon}}$ = mean strain rate, 1/sec,

   V = press ram velocity, mm/sec,

   D_C = billet container diameter, mm,

   D_E = extruded rod diameter, mm,

   α = angle between centerline and dead zone boundary.

For rectangular bars, D_E was taken as the equivalent diameter of the bar cross sectional area, i.e., $D_E = 2\sqrt{area/\pi}$. This same value of D_E was used to determine the direct extrusion dead zone angle (α), following the procedure of Avitzur.

The final experimental design, with the appropriate ram velocities, was:

HIGH Z, HIGH R	HIGH Z, LOW R
V = 2.2 mm/s	V = 6.0 mm/s
LOW Z, HIGH R	LOW Z, LOW R
V = 0.2 mm/s	V = 0.6 mm/s

APPENDIX B

Specimen Type and Location

The front half of each extrusion was solution heat treated*
(SHT), cold water quenched, stretched 1.5%, naturally aged for one
week, and artificially aged for 24 hours at 121°C followed by 15
hours at 163°C (T7651-type temper). The various specimens for
mechanical testing were prepared from sections taken at midplane
along the centerline of the rectangular extrusions and along a
diametral plane for the round extrusions. A complete description
showing specimen location and type of specimen is given in
Tables B1-B3. The drawing number and corresponding specimen type
are summarized in Table B4.

SHT: 7050 - 1.5 hours at 477°C (890°F)
       7475 - 1.5 hours at 516°C (960°F)

LIST OF TABLES

Table B-1. Specimen Locations from 57.2 mm (2¼") Diam. Extruded Rod

S Number

498817
498818

Specimen Drawing #

2 Tensile-L L-7735
2 Tensile-LT L-8751
3 Tear-L-T   L-7201 Type 2
3 Tear-T-L   L-7201 Type 2
2 CT-L-T   D-015365 Size 8
2 CT-T-L   D-015365 Size 7
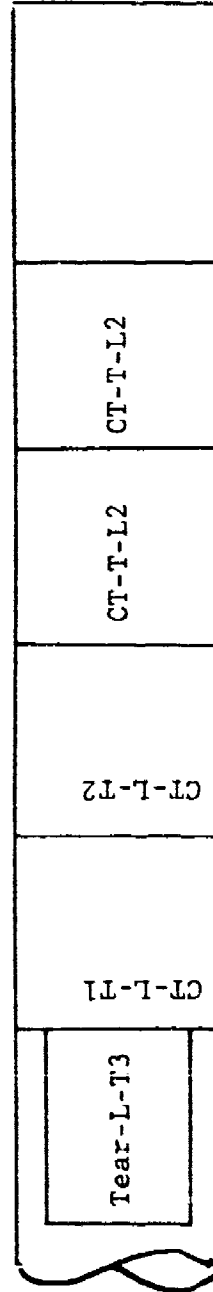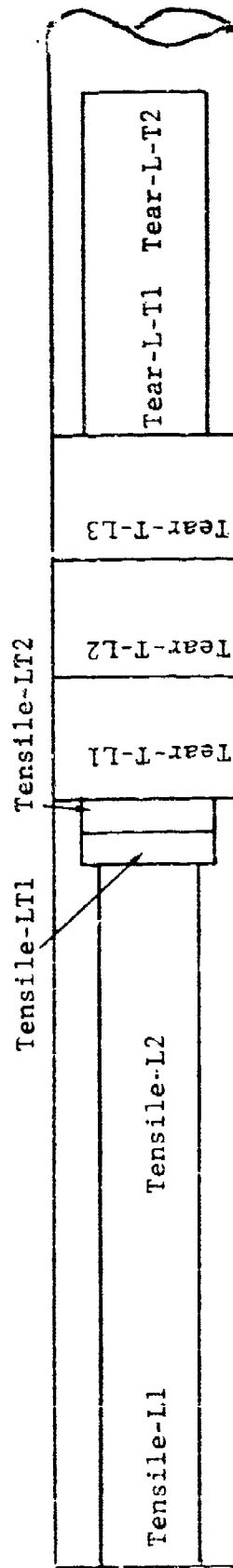
Tensile-L1   Tensile-L2   Tensile-LT1   Tensile-LT2   Tear-T-L1   Tear-T-L2   Tear-T-L3   Tear-L-T1   Tear-L-T2

Tear-L-T3   CT-L-T1   CT-L-T2   CT-T-L2   CT-T-L2

Table B-2. Specimen Locations from 25.4 mm (1") X 102 mm (4") Extruded Bar

S-Number

498809
498810
498811
498812
498823
498824
498825
498826

Specimen Drawing #

2 Tensile-L	L-7735	
2 Tensile-LT	L-8456	
3 Tear-L-T	L-7201	Type 2
3 Tear-T-L	L-7201	Type 2
2 CT-L-T	D-015365	Size 6
2 CT-T-L	D-015365	Size 6

All specimens from center of the thickness

Tear-L-T1   Tear-L-T2   Tear-L-T3

Tear-T-L-1   Tear-T-L-2   Tear-T-L-3

Tensile-LT1   Tensile-LT2

Tensile-L1   Tensile-L2

CT-L-T1   CT-L-T2   CT-T-L1   CT-T-L1
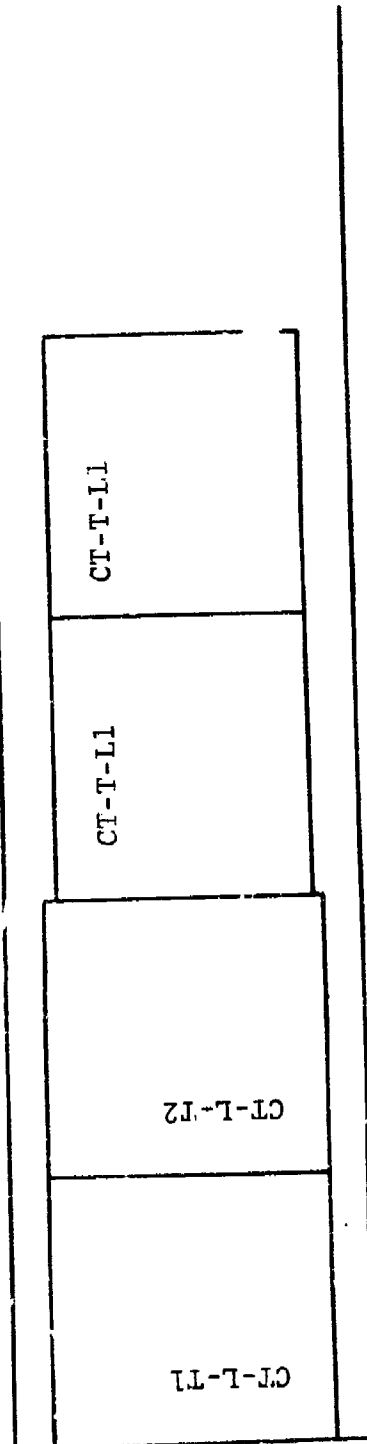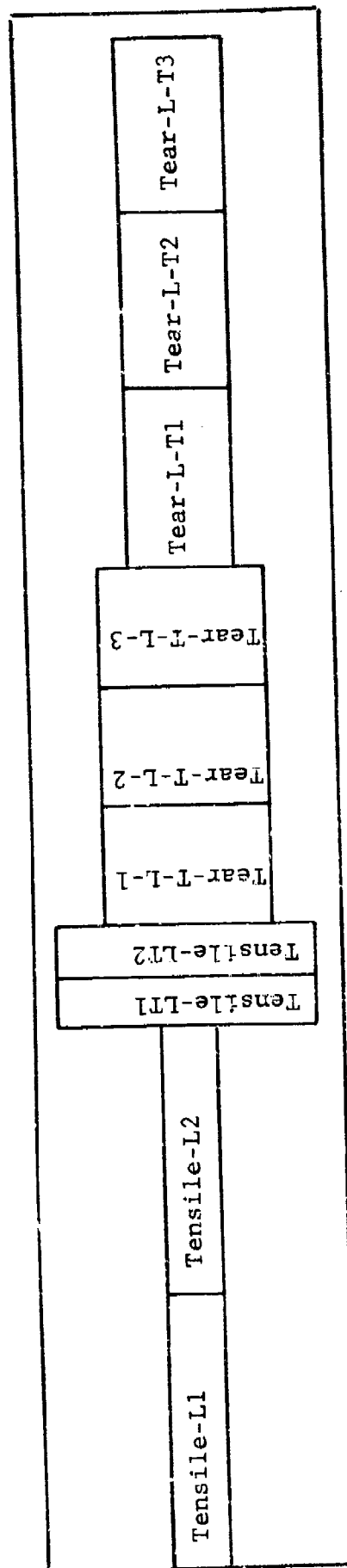
Table B-3.   Specimen Locations from 9.5 mm (3/8") X 95 mm (3 3/4") Extruded Bar

S-Number		Specimen Drawing #	
498813	2 Tensile-L	L-776	
498814	2 Tensile-LT	L-7776	
498815	3 Tear-L-T	L-7201	Type 2
498816	3 Tear-T-L	L-7201	Type 2
498819	2 CT-L-T	D-015365	Size 6
498820	2 CT-T-L	D-015365	Size 6
498821			
498822			

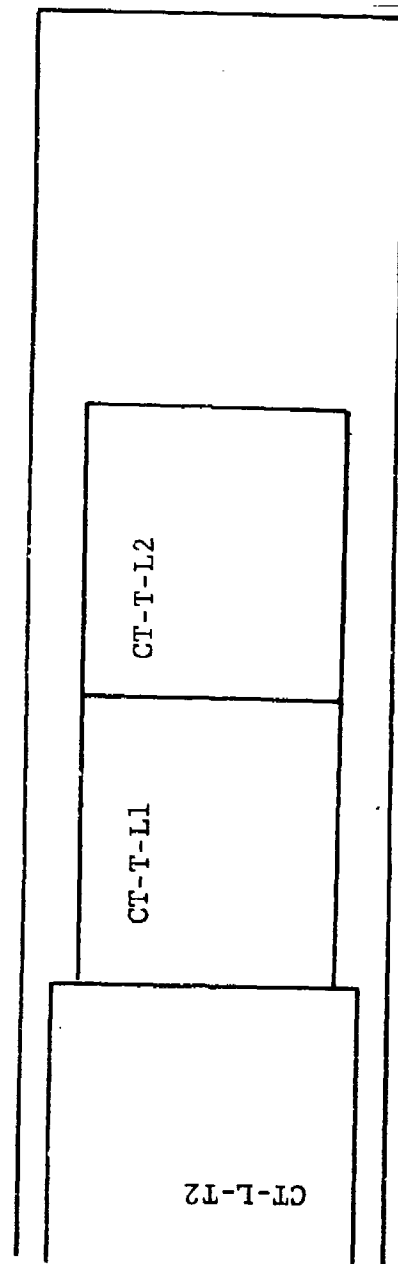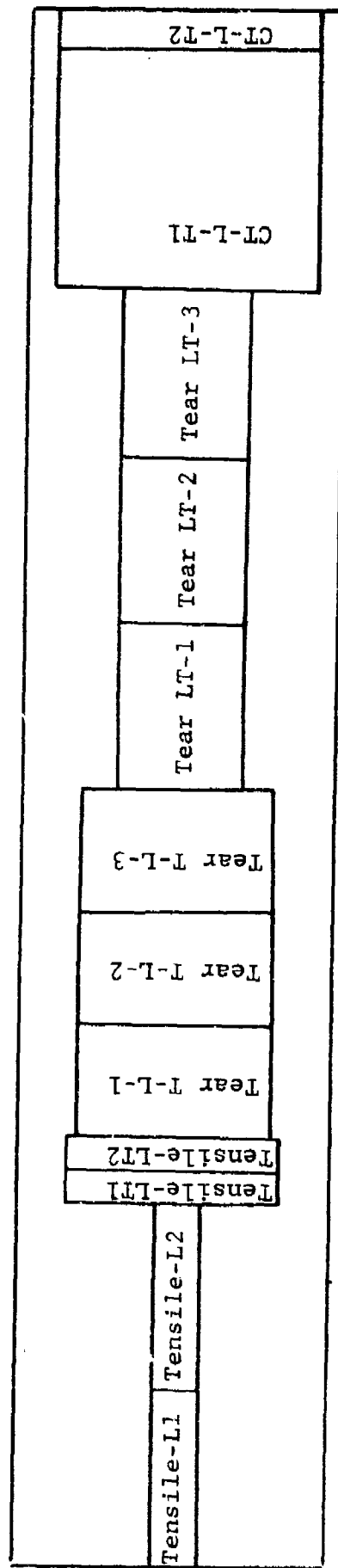All specimens from center of the thickness

Table B-4. Drawing Number and Type of Specimen

Alcoa Drawing Number	Specimen Description
L-8456-RK	.357" Daimeter Tapered Seat Tensile Specimen
L-8751-RK	1/8" Diameter Tapered Seat Tensile Specimen
L-7776-RK	1/4" Diameter Tapered Seat Tensile Specimen
L-7735-RK	1/2" Diameter Tapered Seat Tensile Specimen
D-015365-RK	Compact Tension Crack Growth Specimen
L-7201-RK	Kahn-Type Tear Test Specimen (thickness .100")

APPENDIX C

TEXTURE ANALYSIS

The results of the texture studies and analyses on the low Z extrusions are plotted in Figures C-1 - C-3. The textures could be divided into two types. A duplex <111> + <100> fiber texture with a strong <111> component was present in the round rod. The rectangular sections had a [1$\bar{1}$2] (110) texture. This texture is the type which develops in rolled plate.

Intuitively we might expect the development of a fiber texture during the axisymmetric extrusion of a round product from a round billet. A material is said to have a fiber texture when it has rotational symmetry about an axis, that is all orientations about the axis are equally probable. Since the deformation field is radial, this type of symmetry is reasonable.

Figure C-4 contains the (111) and (001) stereographic projection which can be used in the analysis of the axisymmetric textures.

For a perfect <111> fiber texture, Figure C-5a shows the radial distribution of (200) poles. In this figure, the axis E, N and R are defined. E is parallel to the extrusion direction, N is normal to the extrusion direction, and R is perpendicular to E and N. Since the pole figures were determined in a plane normal to N, we need to know the distribution of the (200) poles in that plane. The distribution normal to N can be determined by rotating the pole figure in Figure C-4b. This is illustrated by rotation of several points on half of the (200) circle.*
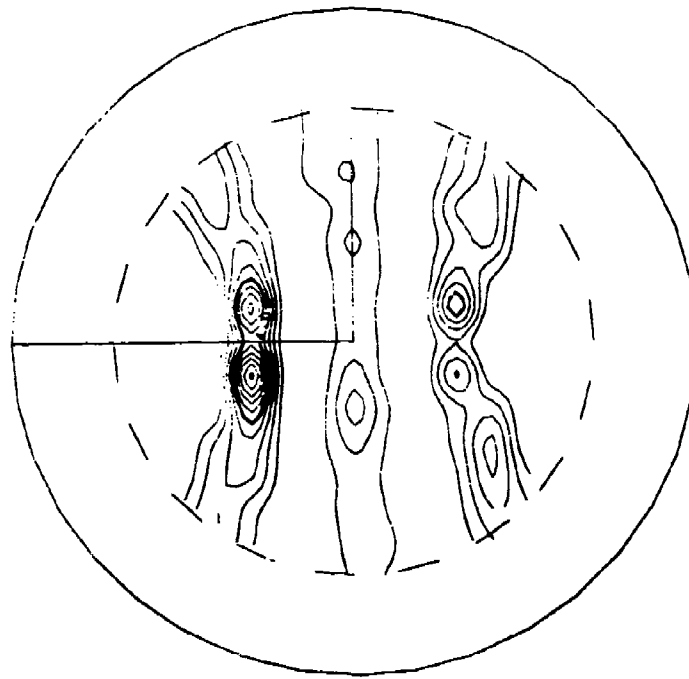
---

*The rotation is accomplished by making the axis of rotation R coincident with the N-S axis of a Wulff net.

Figure C-6a is the result of having rotated half the circle, and Figure C-6b is the complete rotation. The distribution of the (200) poles for a perfect <111> fiber texture normal to and in the plane of the extrusion direction are plotted in Figure C-7. Similarly, the distribution of poles for the (220) and (111) are given in Figures C-8 and C-9, respectively. The distributions of the (200), (220) and (111) for a perfect <100> fiber texture are plotted in Figures C-10, C-11, and C-12, respectively. Comparison of these figures with Figure C-1 facilitates the identification of texture components in the pole figures from this research. For the axisymmetric case a strong <111> and a weak <100> fiber textures were present.
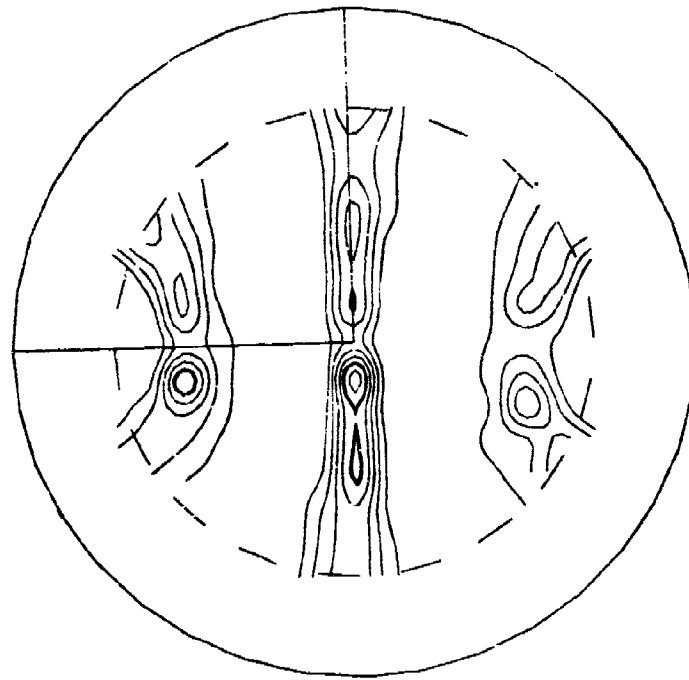
A comparison of Figure C-13 with Figures C-2 and C-3 aid in identifying the texture of the rectangular extrusions, the strong (220) intensity in the plane of the extrusion helps identify the plane, and the strong (220) poled parallel to strong to the extrusion direction orients the (110) sterographic projection with the pole figure. Thus, (110) ($\bar{1}$12) describes the texture for the rectangular sections.

LIST OF FIGURES

537.083
14.059
.090

AL 7475 AXI EX 220

776.340
11.089
.076

AL 7475 AXI EX 200

Figure C-1. (200) and (220) pole figures of SHT 7475 axisymmet-
rically extruded.

AL LOW RA LOW Z 200

689.646
14.037
.080

AL LOW RA LOW Z 220

475.599
12.370
.114

Figure C-2. (200) and (220) pole figures of low Z, low R SHT 7050 extrusion.
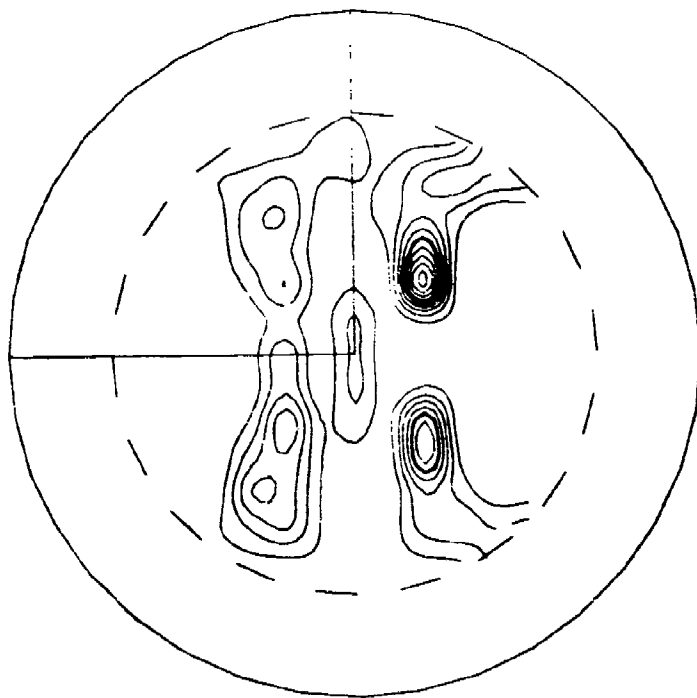
AL HIGH RA LOW Z 200   713.179
                          8.982
                           .103
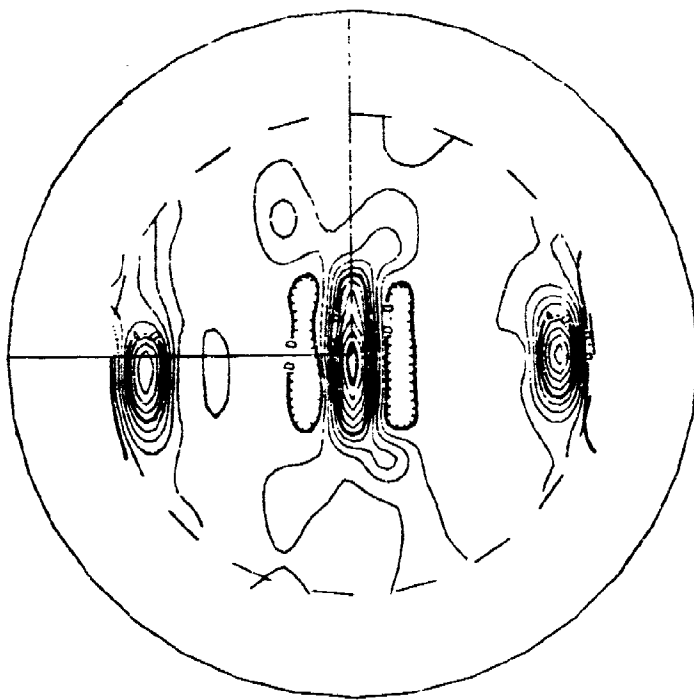
AL HIGH RA LOW Z 220.   475.334
                         10.727
                           .145

Figure C-3.   (200) and (220) pole figures of low Z, high R SHT 7050 extrusion.
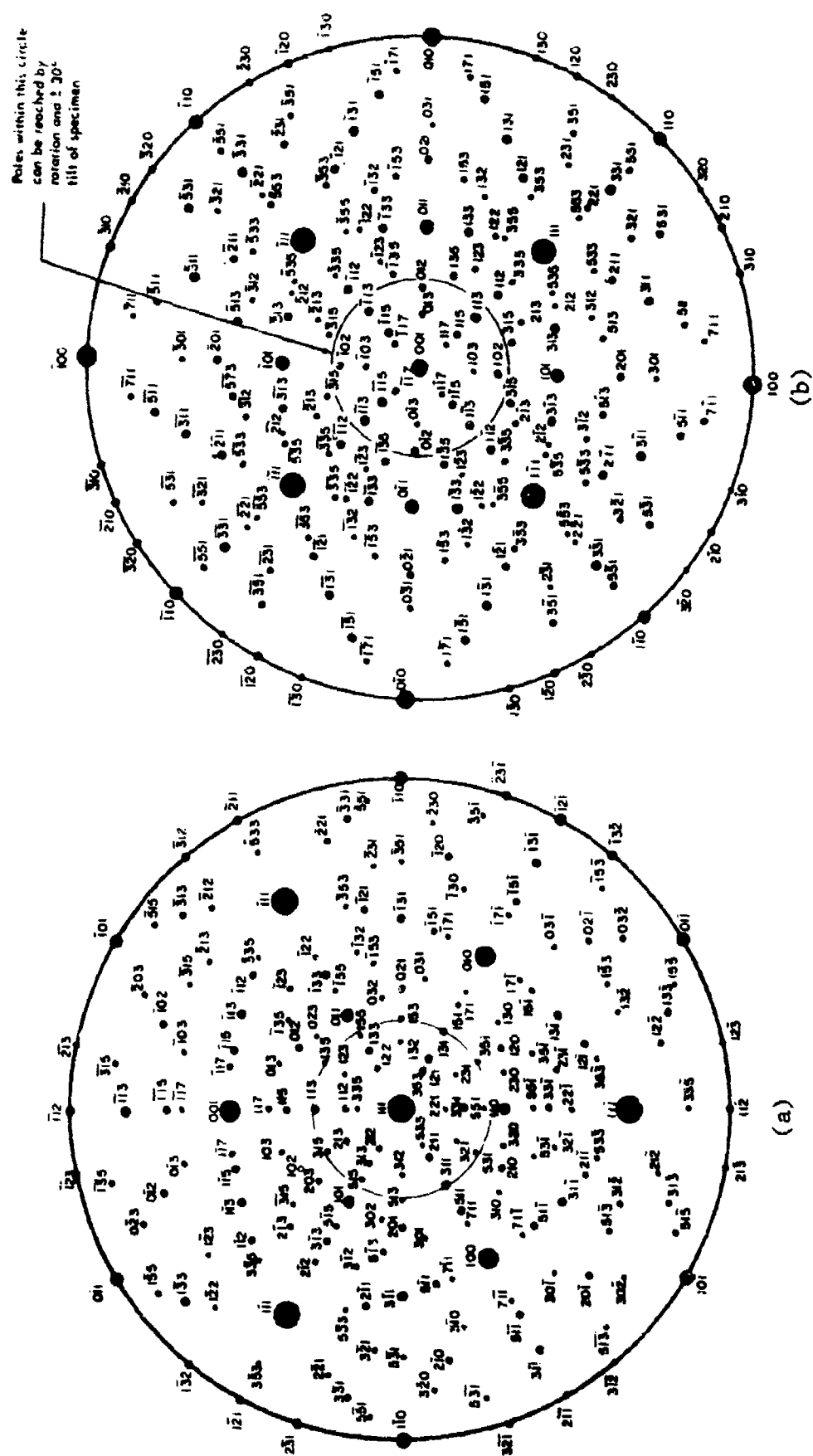
Figure C-4. Stereographic projections for a cubic material (a) (111) and (b) (001).
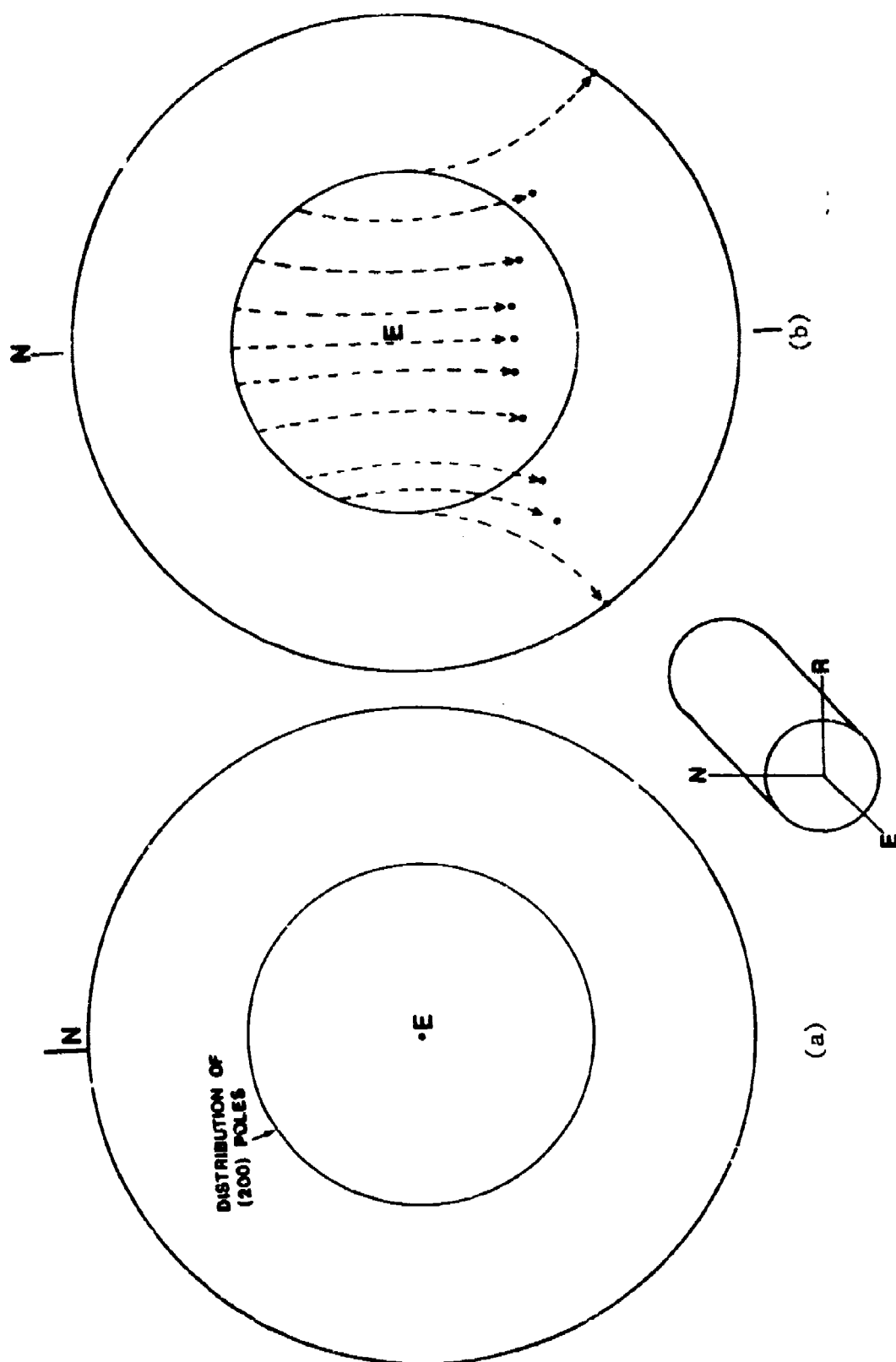
Figure C-5. Rotation of (200) poles about the R axis.
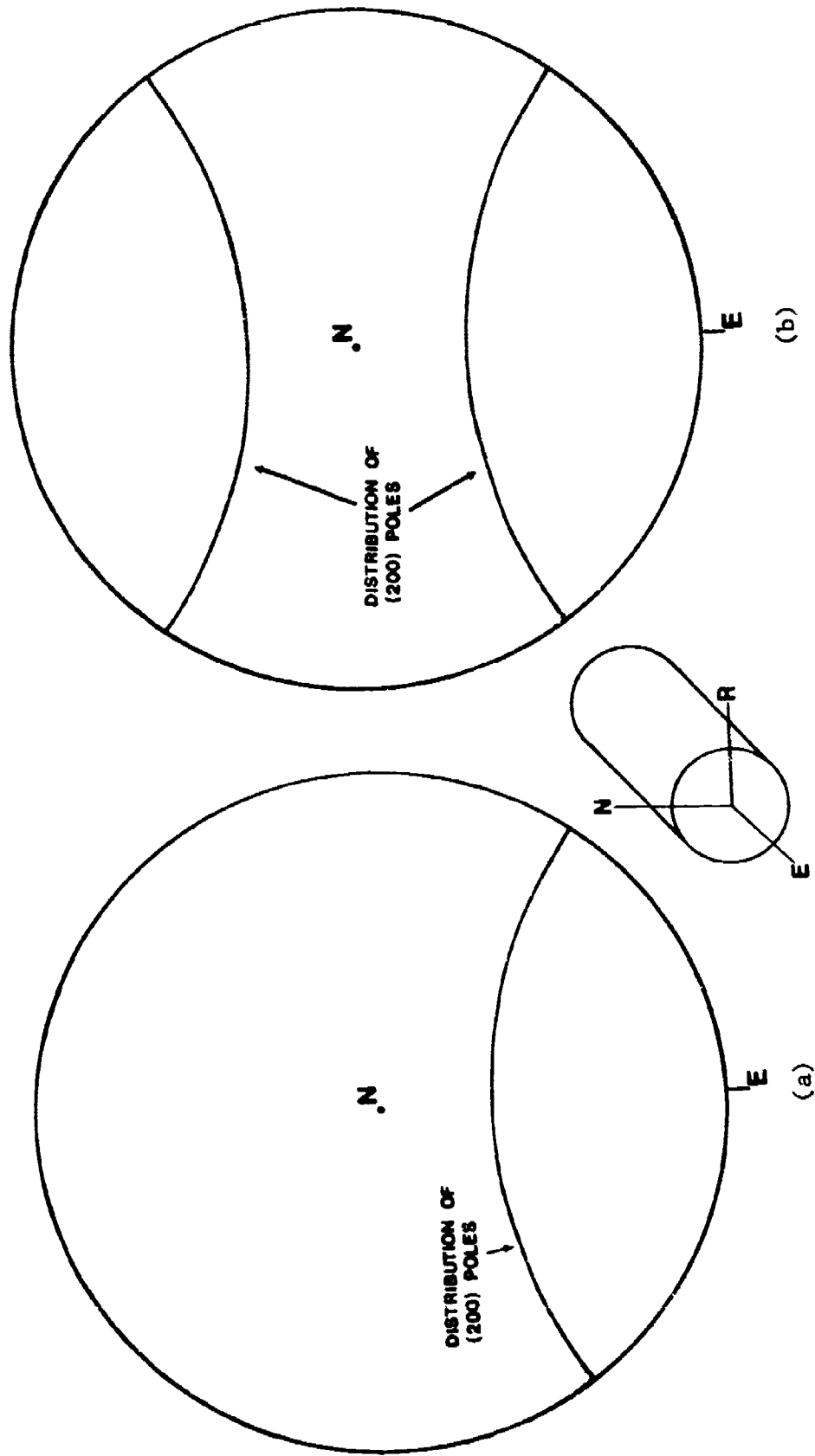
Figure C-6. Rotation of (200) poles about the R axis.

DISTRIBUTION OF
(200) POLES

•E

(a)

DISTRIBUTION OF
(200) POLES

N•

E

(b)
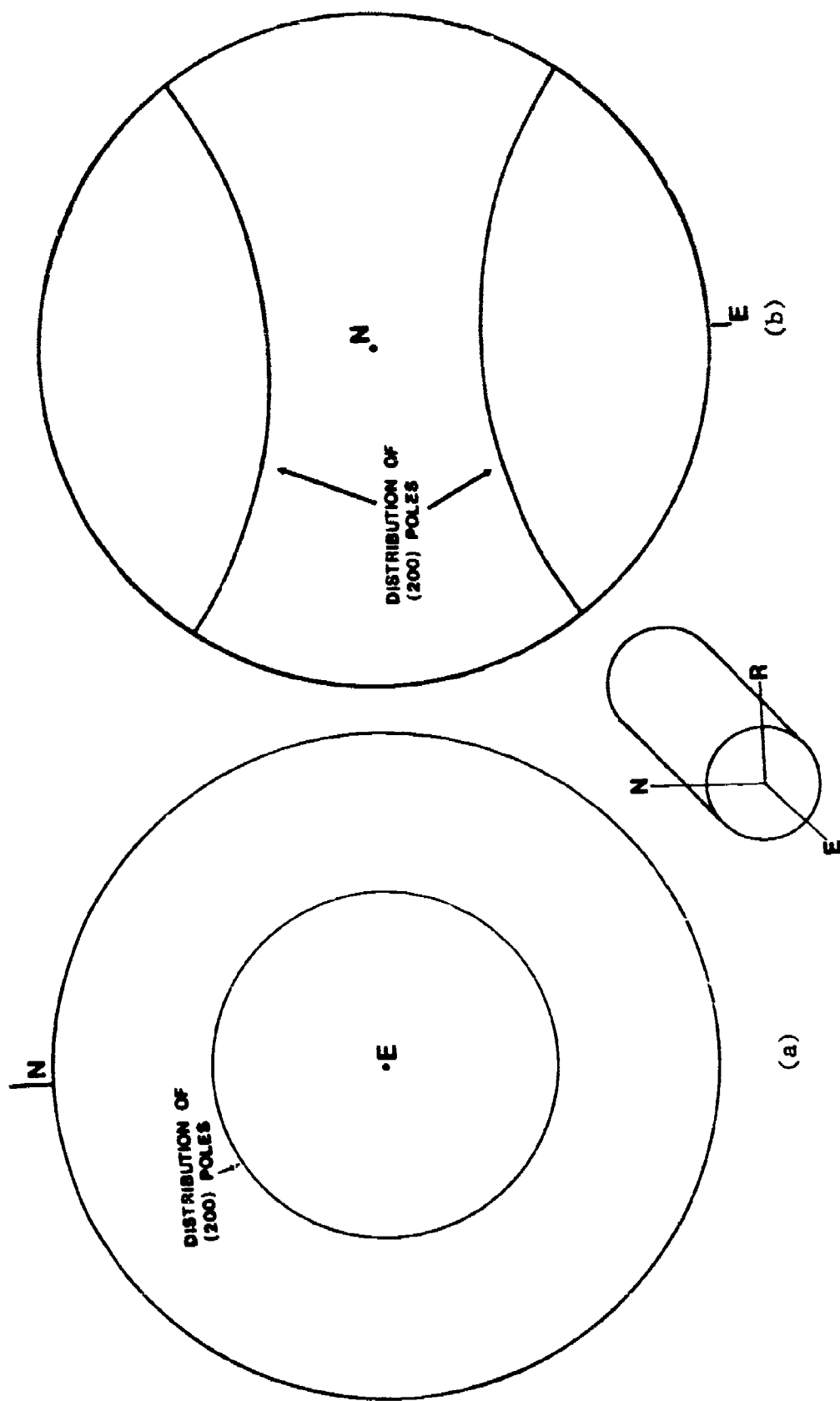
Figure C-7. Distribution of (200) poles collected from a specimen (a) perpendicular and (b) parallel to the extrusion direction for a <111> fiber texture.
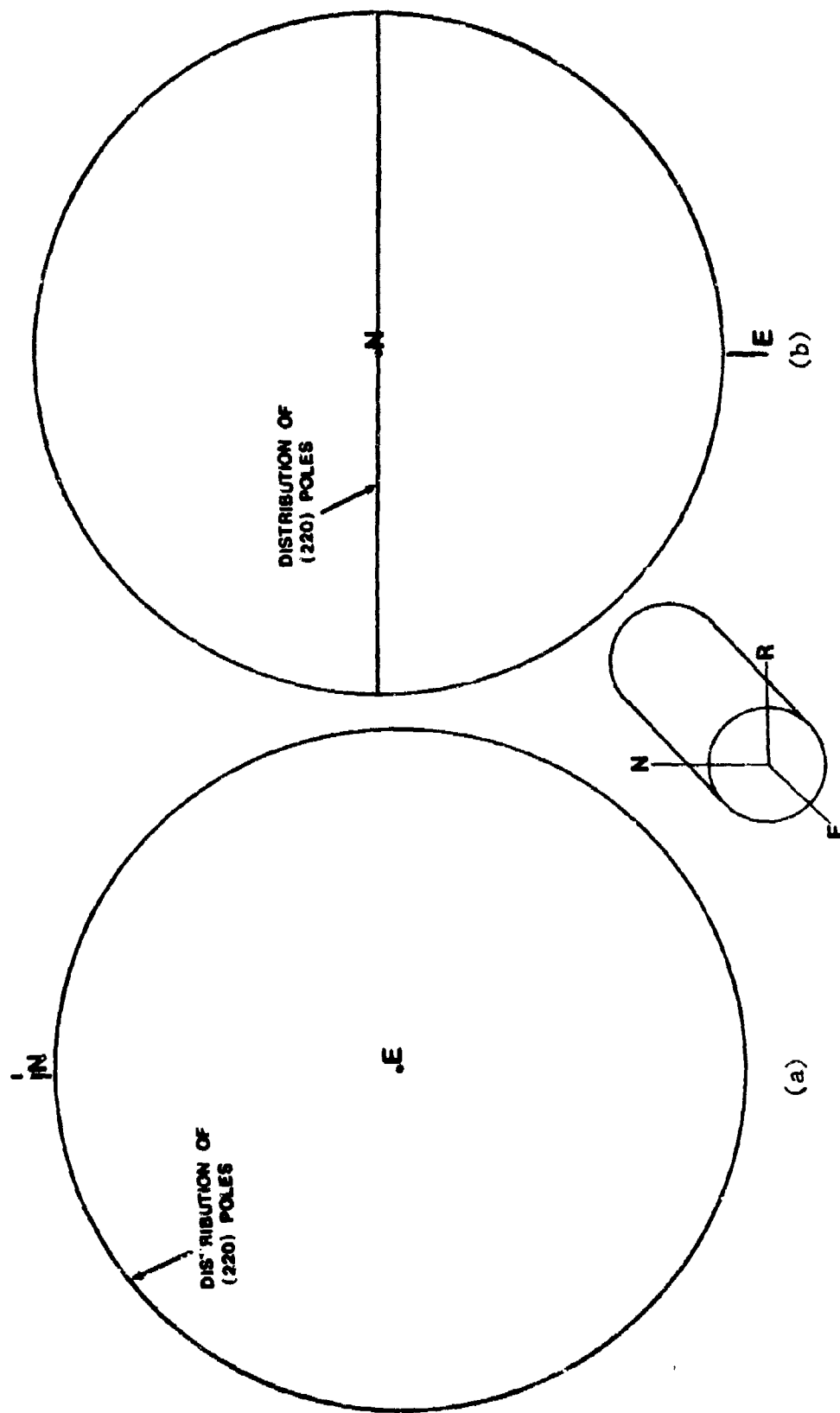
Figure C-8. Distribution of (220) poles collected from a specimen (a) perpendicular and (b) parallel to the extrusion direction for a <111> fiber texture.
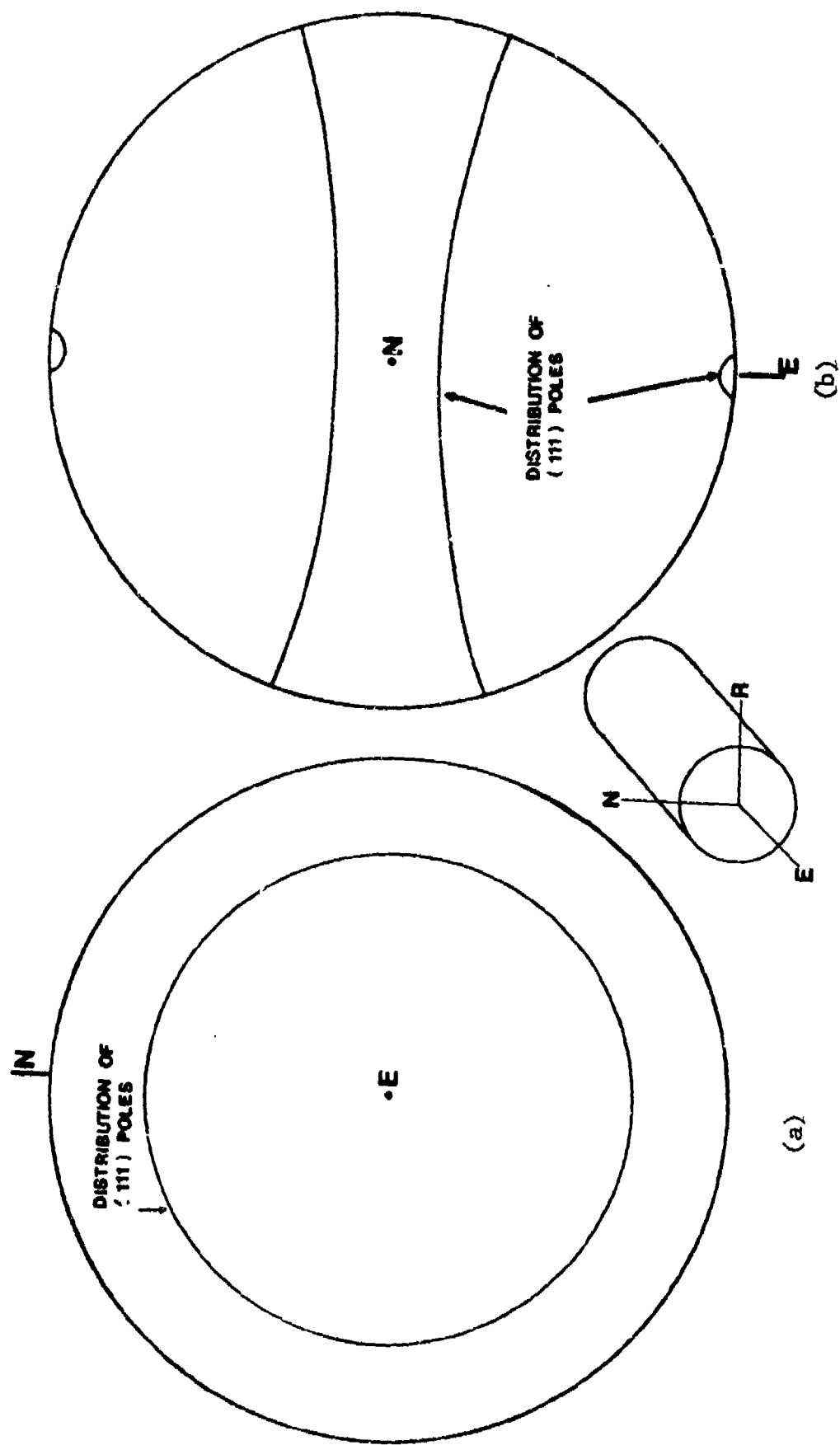
Figure C-9. Distribution of (111) poles collected from a specimen (a) perpendicular and (b) parallel to the extrusion direction for a <111> fiber texture.
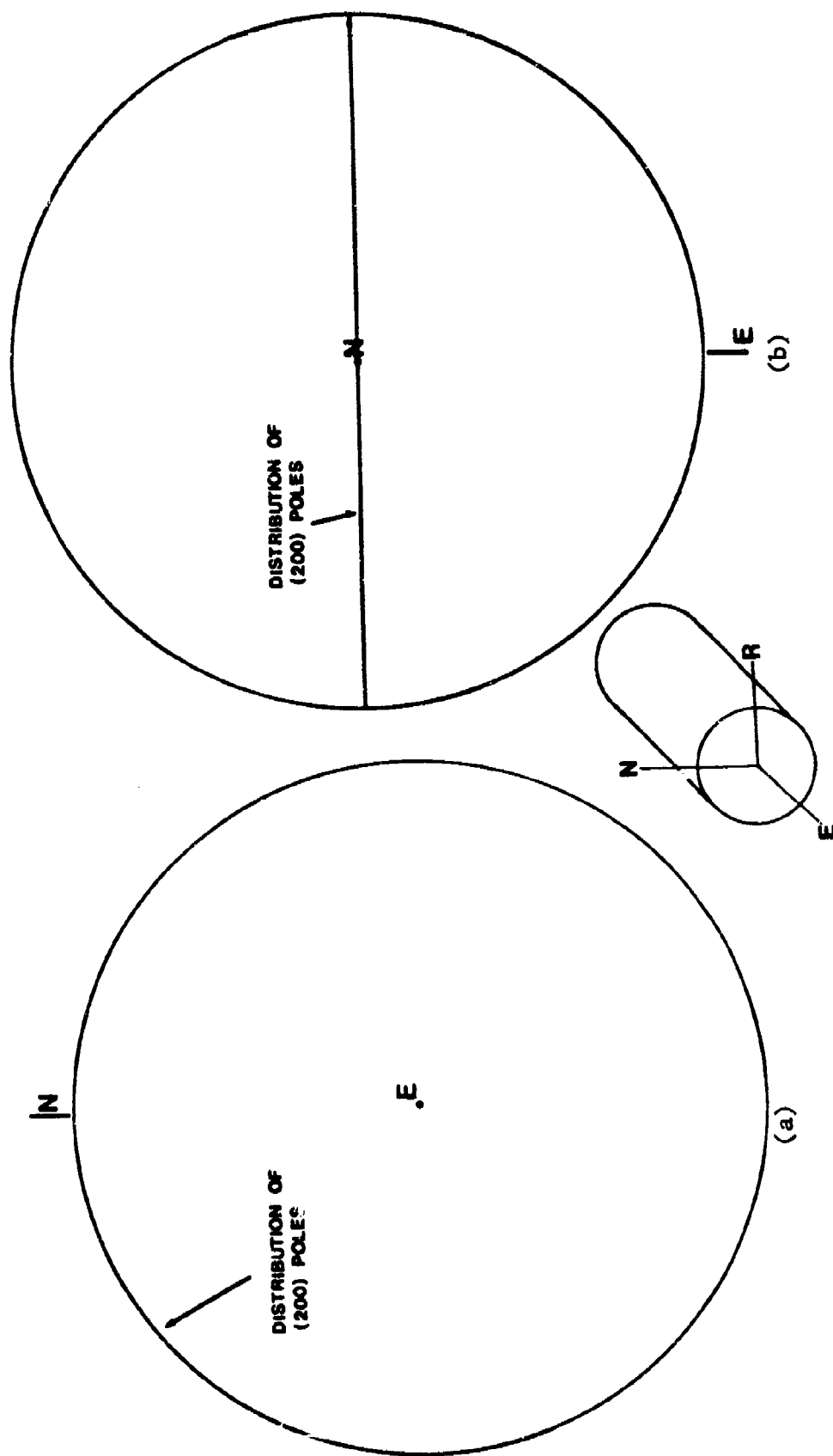
Figure C-10. Distribution of (200) poles collected from a specimen (a) perpendicular and (b) parallel to the extrusion direction for a <100> fiber texture.

DISTRIBUTION OF
(220) POLES

N

E.

(a)

DISTRIBUTION OF
(220) POLES

N

E

(b)

Figures C-11.   Distribution of the (220) poles collected from a specimen (a) perpendicular
(b) parallel to the extrusion direction for a <100> fiber texture.

DISTRIBUTION OF (111) POLES

N

E.

(a)

DISTRIBUTION OF (111) POLES

N.

E

(b)

N **R** **E**
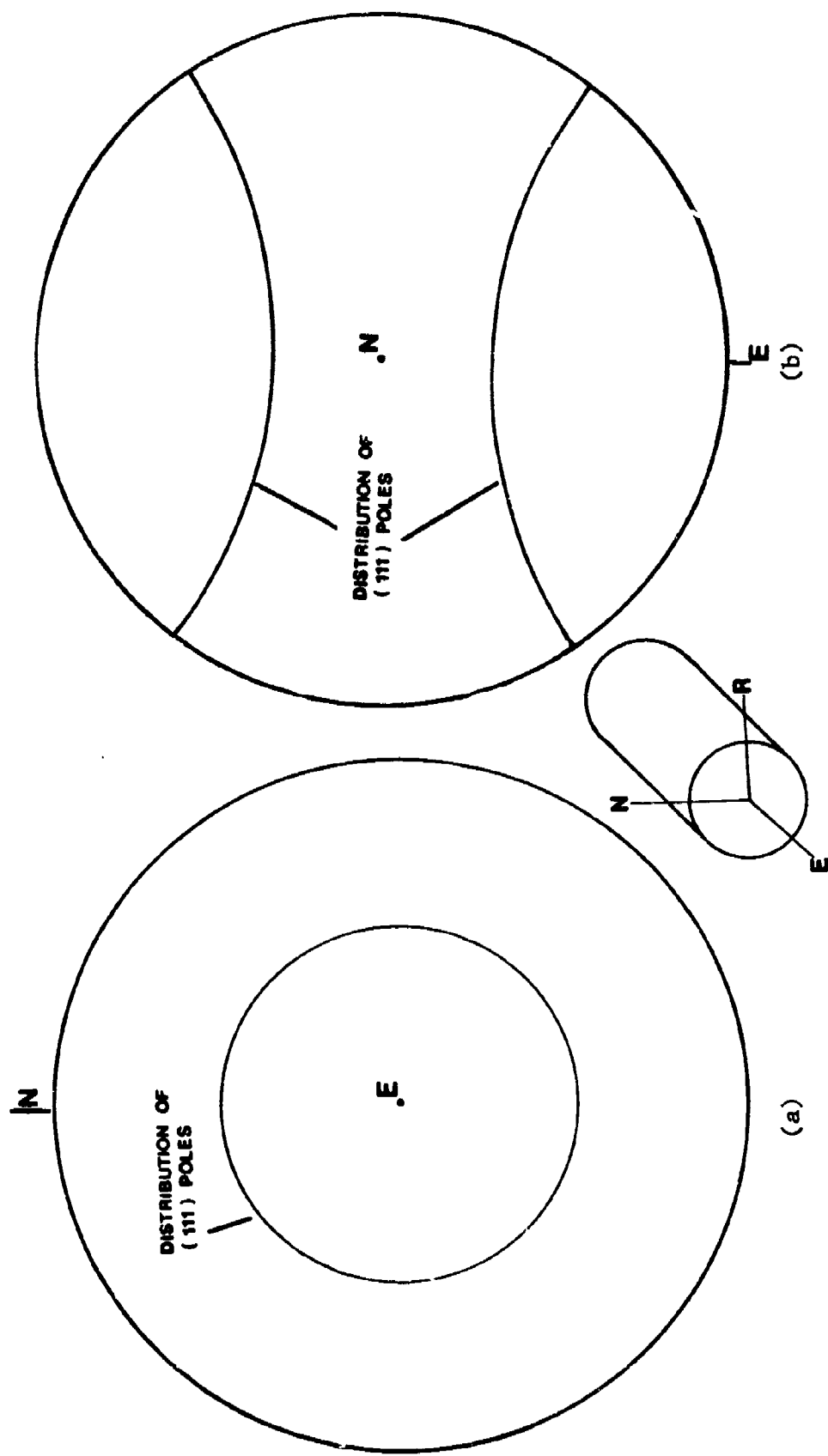
Figure C-12.   Distribution of the (111) poles collected from a specimen perpendicular and
(b) parallel to the extrusion direction for a <100> texture.
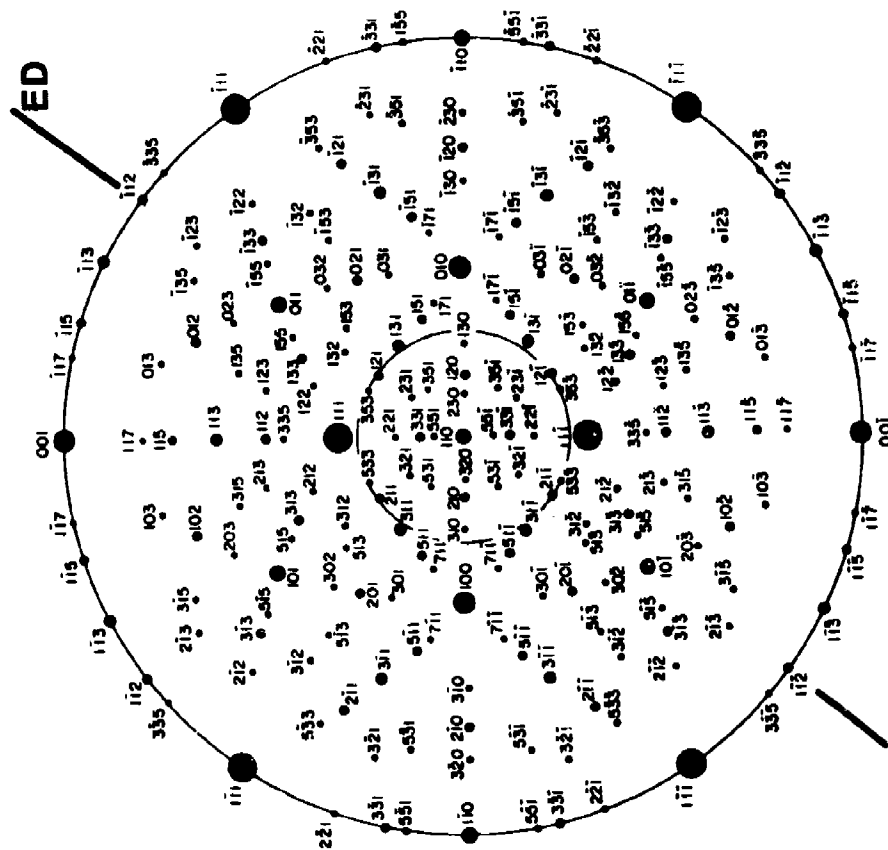
Figure C-13. (110) stereographic projection oriented with respect to the extrusion direction.

DISTRIBUTION LIST

Mr. Michael D. Valentine
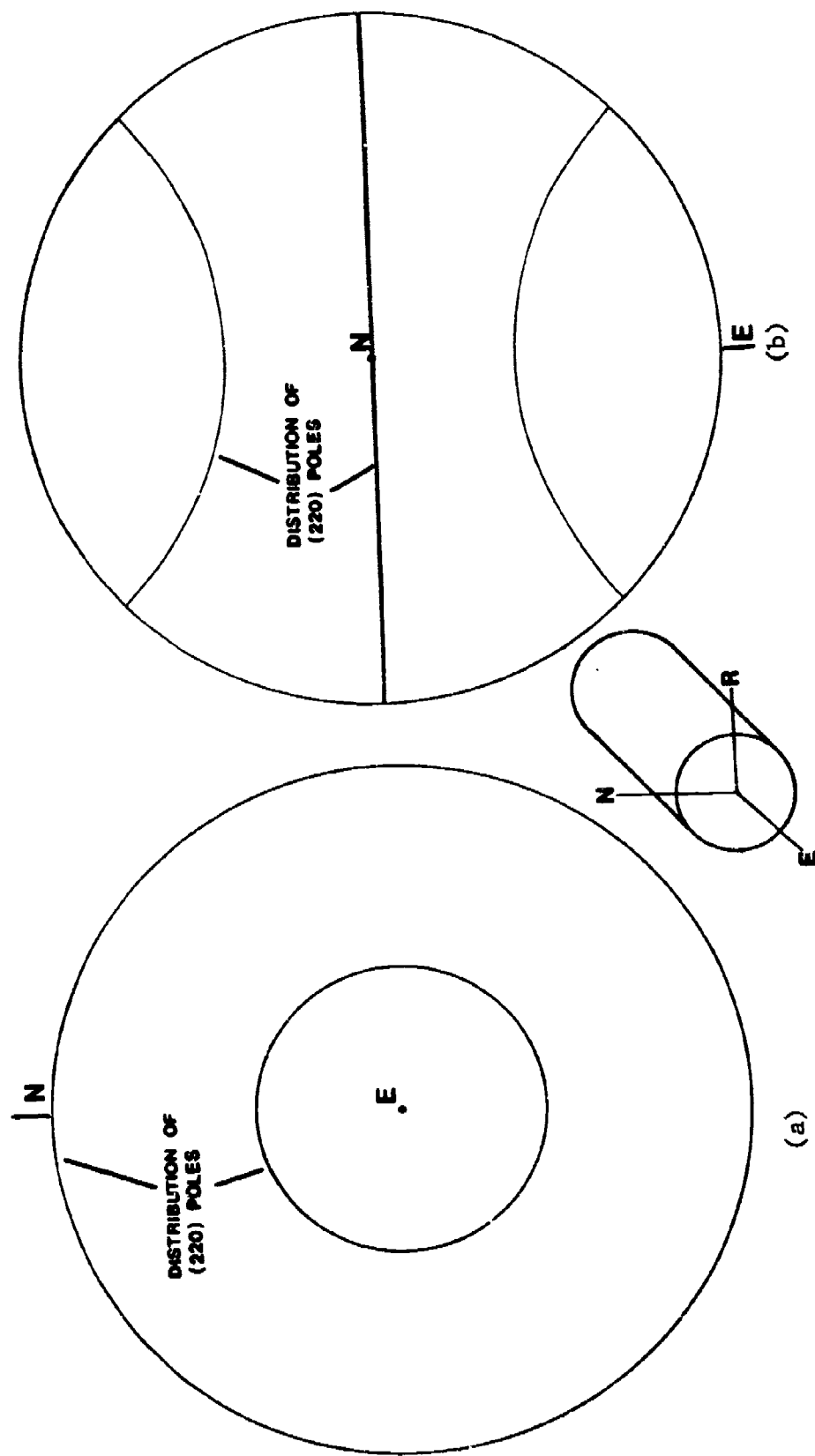AIR-5163C4
Naval Air Systems Command
Washington, DC 20361

Autonetics Division of Rockwell
    International
P. O. Box 4173
Anaheim, CA 92803
Attn: Mr. A. G. Gross, Jr.
    Dept. 522-92

United Technologies Research
    Laboratories
East Hartford, CT 06108
Attn: Mr. Roy Fanti

Dr. D. J. Duquett
Materials Engineering Dept.
RPI
Troy, NY 12181

Dr. R. Balluffi, Chairman
Dept. of Materials Science and
    Engineering
Bard Hall
Cornell University
Ithaca, NY 14853

General Electric Co.
Corporate Research and Development
Bldg. 36-441
Schenectady, NY 12345
Attn: Dr. J. H. Westbrook, Manager
    Materials Information Service

Dr. F. N. Mandigo
Olin Metals Research Laboratories
91 Shelton Avenue
New Haven, CT 06515

The Dow Metal Products Company
Hopkins Building
Midland, MI 48640

Reynolds Metals Company
Metallurgical Research Division
4th and Canal Streets
Richmond, VA 23219
Attn: Dr. J. H. Dedrick

Kaiser Aluminum & Chemical Corp.
Aluminum Division Research Center
    for Technology
P. O. Box 870
Attn: T. R. Pritchett
    Pleasanton, CA 94566

Dr. W. C. Setzer, Director
Metallurgy & Surface Technology
Consolidated Aluminum Corp.
P. O. Box 14448
St. Louis, MO 63178

ERDA Division of Reactor Development and
    Technology
Washington, DC 20545
Attn: Mr. J. M. Simmons, Chief
    Metallurgy Section

University of California
Lawrence Radiation Laboratory
P. O. Box 808
Livermore, CA 94550
Attn: Mr. L. W. Roberts

Midwest Research Institute
425 Volker Boulevard
Kansas City, MO 64110

Linde Company
Division of Union Carbide
P. O. Box 44
Tonawanda, NY 14152

Kawecki Berylco Industries
P. O. Box 1462
Reading, PA 19603

General Electric
Missile & Space Division
Materials Science Section
P. O. Box 8555
Philadephia, PA 91901
Attn: Technical Library

Brush Wellman, Inc.
17876 St. Clair Avenue
Cleveland, OH 44110
Attn: Mr. Bryce King

Avco Space Systems Division
Lowell Industrial Park
Lowell, MA 01851

Southwest Research Institute
8500 Culebra Road
P. O. Box 28510
San Antonio, TX 78284
Attn: Dr. C. Gerald Gardner

Martin Marietta Corporation
P. O. Box 5837
Orlando, FL 32805
Attn: Dr. Richard C. Hall
       Mail Point 275

Martin Marietta Corporation
1450 South Rolling Road
Baltimore, MD 21227
Attn: Dr. Joseph R. Pickens

P. R. Mallory & Co., Inc.
3029 East Washington Street
Indianapolis, IN 46206
Attn: Technical Librarian

Pratt & Whitney Aircraft
Division of United Technologies
Florida Research and Development Center
P. O. Box 2691
West Palm Beach, FL 33402

Rockwell International
P. O. Box 1082
1027 Camino Dos Rios
Thousand Oaks, CA 91320
Attn: Dr. N. Paton

Dr. John A. Schey
Department of Materials Engineering
University of Illinois at Chicago Circle
Box 4348
Chicago, IL 60680

Mr. W. Spurr
The Boeing Company
12842 72nd Avenue, NE
Kirkland, WA 98033

Dr. Howard Bomberger
Reactive Metals, Inc.
Niles, OH 44446

Martin Marietta Aluminum
Attn: Mr. Paul E. Anderson
       (M/C 5401)
19200 South Western Avenue
Torrance, CA 90509

Dr. A. I. Mlavsky
Senior Vice President for Technology &
    Director of Corporate Technology Center
Tyco Laboratories, Inc.
16 Hickory Drive
Waltham, MA 02145

General Dynamics
Fort Worth Division
MZ 5984
P. O. Box 748
Fort Worth, TX 76101
Attn: Mr. E. S. Balmuth

General Dynamics Corp.
Convair Aerospace Division
Fort Worth Operation
P. O. Box 748
Fort Worth, TX 76101
Attn: Tom Coyle

Dr. John D. Wood
Associate Professor
Lehigh University
Bethlehem, PA 18015

Westinghouse Electric Company
Materials & Processing Laboratories
Beulah Road
Pittsburgh, PA 15235
Attn: Don E. Harrison

General Electric Company
Corporate Research & Development
P. O. Box 8
Schenectady, NY 12301
Attn: Dr. D. Wood

Dr. Michael Hyatt
The Boeing Company
P. O. Box 707
Seattle, WA 98124

Dr. Charles Gilmore
Tompkins Hall
George Washington University
Washington, DC 20006

Teledyne CAE
1330 Laskey Road
Toledo, OH 43601

Solar
2200 Pacific Highway
San Diego, CA 92112
Attn: Dr. A. Metcalfe

General Electric Company
Aircraft Engine Group
Material & Processes Technology Lab.
Evendale, OH 45215

AiResearch Manufacturing Co. of America
Sky Harbor Aircraft
402 S. 36th Street
Phoenix, AR 85034
Attn: Mr. Jack D. Tree
      Dept. 93-35-5M

Detroit Diesel Allison Division
General Motors Corporation
Materials Laboratories
Indianapolis, IN 46206

Lycoming Division
AVCO Corporation
Stratford, CT 06497
Attn: Mr. Barry Goldblatt

McDonnell Aircraft Company
St. Louis, MO 63166
Attn: Mr. H. J. Siegel
      Materials & Processes Dev.
      General Engineering Division

Vought Corp.
P. O. Box 5907
Dallas, TX 75222
Attn: Mr. A. Hohman

Northrop Corporation
Aircraft Division
Dept. 3771-62
3901 West Broadway
Hawthorne, CA 90250
Attn: Mr. Allen Freedman

The Boeing Company
Commercial Airplane
ORG. 6-8733, MS77-18
P. O. Box 3707
Seattle, WA 98124
Attn: Cecil E. Parsons

Boeing-Vertol Company
Boeing Center
P. O. Box 16858
Philadelphia, PA 19142
Attn: Mr. J. M. Clark

Sikorsky Aircraft
Division of United Aircraft Corp.
Stratford, CT 06497
Attn: Materials Dept.

Douglas Aircraft Company
3855 Lakewood Blvd.
Long Beach, CA 90808
Attn: Mr. Fred Mehe, C1-250

Lockheed Missile & Space Corp.
Box 504
Sunnyvale, CA 94088
Attn: Mr. C. D. McIntyre
      Bldg. 182, Dept. 84-13

Lockheed Missile & Space Corp.
Box 504
Sunnyvale, CA 94088
Attn: Mr. G. P. Pinkerton
      Bldg. 154, Dept. 8122

Lockheed-Georgia Company
Marietta, Georgia 30061
Attn: E. Bateh

Lockheed California Company
P. O. Box 551
Burbank, CA 91503
Attn: Mr. J. M. VanOrden
      Dept. 74-71, Bldg, 221, Plt. 2

Lockheed Palo Alto Research Lab.
Materials Science Laboratory
3251 Hanover Street
Palo Alto, CA 94303
Attn: Dr. Frank A. Crossley
      52-31/204

Rockwell International
Los Angeles Division
International Airport
Los Angeles, CA 90009
Attn: Gary Keller
Materials Applications

Rockwell International
Rocketdyne Division
Canoga Park, CA 91305
Attn: Dr. Al Jacobs
      Group Scientist
      Materials Branch

Rockwell International
Columbus Division
Columbus, OH 43216
Attn: Mr. P. Maynard, Dept. 75
      Group 521

Kaman Aerospace Corporation
Old Windsor Road
Bloomfield, CT 06001
Attn: Mr. M. L. White

General Dynamics Convair Div.
P. O. Box 80847
San Diego, CA 92138
Attn. Mr. Jack Christian
      Code 643-10

IIT Research Institute
Metals Research Department
10 West 35th Street
Chicago, IL 60616
Attn: Dr. N. Parikh

Battelle Memorial Institute
505 King Avenue
Columbus, OH 43201
Attn: Mr. Stephan A. Rubin, Mgr.
      Information Operations

Director
National Bureau of Standards
Washington, DC 20234
Attn: Dr. E. Passaglia

National Academy of Sciences
Materials Advisory Board
Washington, DC 20418
Attn: Dr. J. Lane

National Aeronautics & Space
    Administration
George C. Marshall Space Flight Center
Huntsville, AL 35812
Attn: Mr. J. G. Williamson
        S&E-ASTN-MMC

National Aeronautics & Space
    Administration
Langley Research Center
Materials Division, Langley Station
Hampton, Virginia 23365
Attn: Mr. H. F. Hardrath
        Stop 188M

National Aeronautics & Space
    Administration
(Code RWM)
600 Independence Avenue, SW
Washington, DC 20546

U. S. Army Armament R&D Command
(ARRADCOM)
Dover, NJ 07801
Attn: Dr. J. Waldman
        DRDAR-SCM-P, Bldg. 3409

Metallurgy and Materials Science Div.
U. S. Army Research Office
P. O. Box 12211
Research Triangle Park, NC 27709
Attn: Dr. G. Meyer

Metallurgy and Materials Science Div.
U. S. Army Research Office
P. O. Box 12211
Research Triangle Park, NC 27709
Attn: Dr. Phillip Parrish

Commanding Officer
Office of Ordnance Research
Box CM, Duke Station
Durham, NC 27706

Army Materials & Mechanics Research Cnt.
Watertown, MA 02172
Attn: Dr. A Gorum

Wright-Patterson Air Force Base
Ohio 45422
Attn: C.L. Harmsworth, AFML/MXE

Wright-Patterson Air Force Base
Ohio 45422
Attn: W. Griffith, AFML/LLS

AFOSR/NE
Bolling Air Force Base
Washington, DC 20332
Attn: Dr. A. H. Rosenstein

Commander, Naval Air Systems Command
Air-954
Washington, DC 20361

Dr. T. R. McNelley
Dept. of Mechanical Engineering (Code 59
Naval Postgraduate School
Monterey, CA 93940

Office of Naval Research
The Metallurgy Program, Code 471
Arlington, VA 22217

Director, Naval Research Laboratory
(Code: 8430)
Washington, Dc 20390

Director, Naval Research Laboratory
(Code: 6601)
Washington, DC 20390

Director, Naval Research Laboratory
(Code: 6490)
Washington, DC 20390

Director, Naval Research Laboratory
(Code: 6380)
Washington, DC 20390

Commander
Naval Surface Weapons Center
(Metallurgy Division)
White Oak
Silver Spring, MD 20910

Naval Ships Research & Development Cnt.
(Code 2812)
Annapolis, MD 21402

Naval Sea Systems Command
(Code 03423)
Department of the Navy
Washington, DC 20360

Commander
Naval Air Development Center
(Code 302)
Warminster, PA 18974